

**ISTANBUL TECHNICAL UNIVERSITY ★ GRADUATE SCHOOL OF SCIENCE**  
**ENGINEERING AND TECHNOLOGY**

**USE OF HYDRODYNAMIC STABILITY APPROACH FOR THE  
CALCULATIONS OF INFLOW BOUNDARY CONDITIONS AND SPREAD OF  
AN AXISYMMETRIC TURBULENT SWIRLING JET**

**M.Sc. THESIS**

**Amir H. MEHRABI**

**Department of Mechanical Engineering**

**Heat-Fluid Engineering Programme**

**JULY 2020**



**ISTANBUL TECHNICAL UNIVERSITY ★ GRADUATE SCHOOL OF SCIENCE**  
**ENGINEERING AND TECHNOLOGY**

**USE OF HYDRODYNAMIC STABILITY APPROACH FOR THE  
CALCULATIONS OF INFLOW BOUNDARY CONDITIONS AND SPREAD OF  
AN AXISYMMETRIC TURBULENT SWIRLING JET**

**M.Sc. THESIS**

**Amir H. MEHRABI**  
**(503171106)**

**Department of Mechanical Engineering**

**Heat-Fluid Engineering Programme**

**Thesis Advisor: Prof. Dr. İ. Bedii ÖZDEMİR**

**JULY 2020**



**İSTANBUL TEKNİK ÜNİVERSİTESİ ★ FEN BİLİMLERİ ENSTİTÜSÜ**

**HİDRODİNAMİK KARARLILIK ANALİZİ İLE OLUŞTURULAN GİRİŞ  
KOŞULLARI KULLANILARAK ÇALKANTILI SARMAL JET AKIŞI  
BENZETİMİNİN YAPILMASI**

**YÜKSEK LİSANS TEZİ**

**Amir Hossein MEHRABI  
(503171106)**

**Makina Mühendisliği Anabilim Dalı**

**Isı-Akışkan Mühendisliği Programı**

**Tez Danışmanı: Prof. Dr. İ. Bedii ÖZDEMİR**

**TEMMUZ 2020**



Amir H. MEHRABI, a M.Sc student of ITU Graduate School of Science Engineering and Technology student ID 503171106 successfully defended the thesis/dissertation entitled “USE OF HYDRODYNAMIC STABILITY APPROACH FOR THE CALCULATIONS OF INFLOW BOUNDARY CONDITIONS AND SPREAD OF AN AXISYMMETRIC SWIRLING TURBULENT JET”, which he prepared after fulfilling the requirements specified in the associated legislations, before the jury whose signatures are below.

**Thesis Advisor:**      **Prof. Dr. İ. Bedii ÖZDEMİR**      .....

İstanbul Technical University

**Jury Members:**      **Doç. Dr. Bayram ÇELİK**      .....

İstanbul Technical University

**Dr. İlyas YILMAZ**      .....

İstanbul Bilgi University

**Date of Submission : 1 June 2020**

**Date of Defense : 15 July 2020**



*To my family,*



## **FOREWORD**

First of all, I would like to thank my supervisor Prof. Dr. İ. Bedii Özdemir for his guidance and patience for me and this thesis.

I also want to thank my office-mates Cenk, Hamed and Mert for the great moments we had throughout my Master of Science study.

I would also like to express my gratitude to my family and friends for their endless support and confidence in me. Knowing the fact that they will be always be there to stand by me, gave me the strength to accomplish this thesis.

Finally this work was supported by Research Fund (BAP) of the Istanbul Technical University (Project Number: MYL-2018-41891).

June 2020

Amir H. MEHRABI



## TABLE OF CONTENTS

	<u>Page</u>
<b>FOREWORD</b> .....	<b>ix</b>
<b>TABLE OF CONTENTS</b> .....	<b>xi</b>
<b>ABBREVIATIONS</b> .....	<b>xiii</b>
<b>SYMBOLS</b> .....	<b>xv</b>
<b>LIST OF TABLES</b> .....	<b>xix</b>
<b>LIST OF FIGURES</b> .....	<b>xxi</b>
<b>SUMMARY</b> .....	<b>xxiii</b>
<b>ÖZET</b> .....	<b>xxiv</b>
<b>1. INTRODUCTION</b> .....	<b>1</b>
1.1 Purpose and Relevance.....	1
1.2 Literature Review .....	3
1.3 Stability of Swirling Jet Flows .....	4
<b>2. HYDRODYNAMIC STABILITY ANALYSIS OF SWIRLING FLOW</b> .....	<b>7</b>
2.1 Reynolds Decomposition and Linearization of the Navier-Stokes Equations ...	7
2.2 Normal Mode Expansion and Modal Equations .....	12
2.3 Nondimensionalization.....	14
2.4 Mean Velocity Profile and the Boundary Conditions .....	18
2.5 Numerical Solution Process .....	20
2.6 Parallel Shooting Method.....	21
<b>3. RESULTS OF HYDRODYNAMIC STABILITY ANALYSIS</b> .....	<b>23</b>
<b>4. LARGE EDDY SIMULATION OF AN INCOMPRESSIBLE, AXISYMMETRIC, TURBULENT SWIRLING JET</b> .....	<b>35</b>
4.1 Turbulence Simulation: DNS .....	35
4.2 Turbulence Simulation: RANS .....	35
4.3 Turbulence Simulation: LES .....	35
4.3.1 Filtering in LES.....	37
4.3.2 Formulation of equations .....	38
4.3.3 Leonard decomposition.....	38
4.3.4 SGS models.....	39
4.4 Mean Flow and Turbulent Parameters .....	40
<b>5. COMPUTATIONAL PROCEDURES OF SWIRLING JETS</b> .....	<b>43</b>
5.1 Computational Domain .....	43
5.2 Flow Solver and Numerical Methods.....	46
5.2.1 Spatial discretization .....	46
5.2.2 Temporal discretization.....	46
5.2.3 Wall boundary condition.....	47
5.2.4 Inflow boundary conditions .....	47
5.2.5 Outflow boundary conditions.....	48
<b>6. RESULTS OF LARGE EDDY SIMULATIONS OF SWIRLING JETS</b> .....	<b>51</b>
6.1 Axial Velocity Results .....	51
6.2 Azimuthal Velocity Results .....	56
6.3 Spectrum Analysis.....	60

<b>7. CONCLUSION.....</b>	<b>63</b>
<b>REFERENCES.....</b>	<b>65</b>
<b>CURRICULUM VITAE.....</b>	<b>75</b>

## **ABBREVIATIONS**

<b>CFL</b>	: Courant-Friedrich-Lewy
<b>DNS</b>	: Direct Numerical Solution
<b>LES</b>	: Large Eddy Simulation
<b>LHS</b>	: Left Hand Side
<b>PISO</b>	: Pressure-Implicit with Splitting of Operators
<b>RHS</b>	: Right Hand Side
<b>RMS</b>	: Root-mean-square
<b>SIM</b>	: Simulation
<b>SGS</b>	: Subgrid scale
<b>UDF</b>	: User-defined function



## SYMBOLS

$A_r, A_\phi, A_z, A_p$	: Eigenfunctions of fluctuation components
$c$	: Scaling constant for turbulent intensity
$C$	: Arbitrary constant for orthonormalization condition
$C_{ij}$	: Cross-stress tensor
$C_s$	: Smogorinsky constant
$D_0$	: Diameter of the pipe
$E$	: Discrepancy vector
$G$	: Filter function
$i$	: Complex number $\sqrt{-1}$
$\text{Im}()$	: Imaginary part
$k_r, k_\phi, k_z$	: Wavenumbers in cylindrical coordinates
$l_0$	: Length scale of large eddies
$J$	: Jacobien matrix
$L$	: Length scale of mean flow
$L_s$	: Mixing length
$L_{ij}$	: Leonard stress tensor
$p'$	: Pressure fluctuation
$p'_{\text{rms}}$	: RMS of pressure fluctuation
$P$	: Instantaneous value of pressure
$P_0$	: Operating pressure
$\bar{P}$	: Time-averaged value of pressure
$\bar{p}$	: Filtered pressure
$r$	: Radial coordinate
$r_0$	: Radius of the pipe
$R_{ij}$	: Reynolds stress tensor
$\text{Re}$	: Reynolds number of mean flow
$\text{Re}_{r_0}$	: Reynolds number related to radius of the pipe
$\text{Re}_l$	: Reynolds number of large scales
$\text{Re}()$	: Real part

$S$	: Swirl number
$\tilde{S}_{ij}$	: Resolved scale strain rate tensor
$t$	: Time
$T$	: Period
$TI$	: Turbulent intensity
$u_0$	: Velocity scale of large eddies
$u_\eta$	: Velocity scale of small eddies
$u'_r, u'_\phi, u'_z$	: velocity fluctuations in cylindrical coordinates
$u'_{r, \text{rms}}, u'_{\phi, \text{rms}}, u'_{z, \text{rms}}$	: RMS of velocity fluctuations
$\tilde{u}_i$	: Resolved part of velocity component
$u''_i$	: SGS part of velocity component
$U_c$	: Convection velocity
$U_{cl}$	: Centerline velocity
$U_L$	: Local velocity
$U_{bulk}$	: Bulk axial velocity at jet exit
$U_{\text{mean}}$	: Velocity scale of mean flow
$U_r, U_\phi, U_z$	: instantaneous velocity field in cylindrical coordinates
$\overline{U_r}, \overline{U_\phi}, \overline{U_z}$	: time-averaged velocity field in cylindrical coordinates
$v_{\text{group}}$	: Group velocity
$v_{\text{phase}}$	: Phase velocity
$\mathbf{V}$	: Prediction vector
$\delta_{ij}$	: Kronecker delta
$\omega$	: Frequency
$z$	: Coordinate in axial direction
$\eta$	: Length scale for small eddies
$\mu$	: Dynamic viscosity of air
$\mu_t$	: Subgrid turbulent viscosity
$\nu$	: Kinematic viscosity of air
$\phi$	: Azimuthal coordinate
$\rho$	: Density of air
$\theta$	: Flow field variable
$\bar{\theta}$	: Resolved part of a flow field variable
$\theta''$	: SGS part of a flow field variable
$\tau_0$	: Time scale of large eddies

$\tau_{ij}$  : SGS stress tensor  
 $\tau_\eta$  : Time scale of small eddies  
 $\Delta$  : Filter width  
 $\Delta t$  : Time step size  
 $\Delta z$  : Cell size in axial direction



## LIST OF TABLES

	<u>Page</u>
<b>Table 3.1</b> : Initial guess values at boundaries. ....	<b>24</b>
<b>Table 4.1</b> : Experimental jet flow parameters. ....	<b>40</b>
<b>Table 4.2</b> : Turbulent scales. ....	<b>41</b>
<b>Table 5.1</b> : Turbulent intensity characteristics at inflow boundary and the calculated values of $c$ for all simulations. ....	<b>48</b>



## LIST OF FIGURES

	<u>Page</u>
<b>Figure 2.1</b> : Normalized jet exit velocity profiles at $z/D_0 = 0.0$ a) Axial b) Azimuthal (Örlü and Alfredsson, 2008). .....	18
<b>Figure 3.1</b> : Computational domain for mode calculation. ....	23
<b>Figure 3.2</b> : Variation of real part of normalized wavenumber $k_{zr}^*$ with normalized frequency $\omega^*$ , a) $k_\phi = 0$ , b) $k_\phi = 1$ .....	25
<b>Figure 3.3</b> : Variation of the decay rate $k_{zi}$ with normalized frequency $\omega^*$ for $k_\phi = 0$ . ....	26
<b>Figure 3.4</b> : Variation of the decay rate $k_{zi}$ with normalized frequency $\omega^*$ for $k_\phi = 1$ . ....	28
<b>Figure 3.5</b> : Mode shapes for $k_r = 0$ at different frequencies, Left, radial component, $Y_1 = u'_r$ . Center, tangential component $Y_2 = u'_\phi$ . Right, axial component $Y_3 = u'_z$ . ....	30
<b>Figure 3.6</b> : Mode shapes for $k_r = 1$ at different frequencies, Left, radial component, $Y_1 = u'_r$ . Center, tangential component $Y_2 = u'_\phi$ . Right, axial component $Y_3 = u'_z$ . ....	31
<b>Figure 3.7</b> : Zoom in features near the centerline, Left $u'_r$ , Center $u'_\phi$ , Right $u'_z$ ....	32
<b>Figure 3.8</b> : Radial distribution of RMS profiles, a) $u'_{r,rms}$ , b) $u'_{\phi,rms}$ c) $u'_{z,rms}$ ....	34
<b>Figure 4.1</b> : A schematic differentiation between RANS, LES and DNS modeling. (Sagaut et al, 2013).....	36
<b>Figure 5.1</b> : Geometry of computational jet domain with boundaries shown. ....	43
<b>Figure 5.2</b> : Computational mesh a) slice of computational grid at $x = 0$ . b) Close up section of computational grid near jet exit at $x = 0$ c) Computational grid section in the $y-z$ plane,close up of inlet plane grid. d) O-grid type used in azimuthal direction e) strong zoom of d). ....	45
<b>Figure 6.1</b> : Radial profiles of normalized mean axial velocity at $z/D_0 = 0.0$ (■): Experimental data, (—): SIM1, (---): SIM2, (---): Power-law profile. ....	52
<b>Figure 6.2</b> : Radial profiles of axial turbulent intensity at $z/D_0 = 0.0$ ■: Experimental data, (—): SIM1, (---): SIM2. ....	52
<b>Figure 6.3</b> : Radial profiles for normalized mean axial velocity at different streamwise locations. (■): Experimental data, (—): SIM1, (---): SIM2, (Each curve is moved up by 2 with respect to previous one)..	53
<b>Figure 6.4</b> : Visualization of the time-averaged axial velocity $U_z$ . The radial profiles of normalized mean axial velocity shown at selected axial positions.....	54
<b>Figure 6.5</b> : Radial profiles of axial turbulent intensity at different streamwise locations: Near-field region. (■): Experimental data, (—): SIM1,	

(--): SIM2, (Each curve is moved up by 0.2 with respect to previous one).....	55
<b>Figure 6.6</b> : Radial profiles of mean azimuthal velocity at first four streamwise location. (■): Experimental data, (—): SIM1, (---): SIM2 .....	57
<b>Figure 6.7</b> : Radial profile of azimuthal turbulent intensities at different streamwise locations. (—): SIM1, (---): SIM2. ....	59
<b>Figure 6.8</b> : Power spectrum of axial velocity at $z/D_0 = 1, r/R = 0.6$ . a) - c) SIM1 d) - f) SIM2.....	60

# **USE OF HYDRODYNAMIC STABILITY APPROACH FOR THE CALCULATIONS OF INFLOW BOUNDARY CONDITIONS AND SPREAD OF AN AXISYMMETRIC TURBULENT SWIRLING JET**

## **SUMMARY**

Turbulent swirling jets have been the subject of a significant amount of research due to their importance and wide usage in many industrial engineering applications. It is well known that such flows show strong unsteady characteristics and they are dominated by large-scale structures, which influence the stability, endurance and noise level of the applications adversely. To simulate and capture the space and time dependent characteristics of turbulent jets, it is required to create an instantaneous flow-field with a viable transient solution method.

Direct Numerical Simulation (DNS) and Large Eddy Simulation (LES) are known to be the prominent simulation models to resolve unsteady features of turbulent swirling jets. However, there are several drawbacks associated with these numerical methods. One of these is to specify proper turbulent inflow boundary conditions with appropriate time and space correlations because the flow development downstream is highly dependent on turbulent behavior upstream and at the inlet boundary. To create such inflow conditions with appropriate space-time correlations, the hydrodynamic stability approach excels as a feasible method, in which it is possible to find proper modes related to the flow field under consideration and these modes can be used to create time-dependent velocity profiles with correct cross-correlations.

The purpose of this study is to generate proper and sufficiently accurate inflow boundary conditions for turbulent swirling jet simulations using the LES method with the modes obtained from hydrodynamic stability approach. This goal is achieved in two stages: In the first stage, the hydrodynamic stability of a circular pipe flow was analyzed by deriving linearized equations of motion for fluctuation components, which were solved by the parallel shooting method to obtain Fourier modes. In the second stage, by using these modes, instantaneous velocity profiles with correct space-time correlations were generated, which were then used as an inflow boundary condition in several LES simulations of an incompressible, axisymmetric turbulent swirling air jet. Finally, results were compared with the experimental data.

The results revealed that the simulations with proper turbulent conditions at the inflow boundary, compared to the case without perturbations, provided better agreement with measurements in terms of turbulent intensity.

# HİDRODİNAMİK KARARLILIK ANALİZİ İLE OLUŞTURULAN GİRİŞ KOŞULLARI KULLANILARAK ÇALKANTILI SARMAL JET AKIŞI BENZETİMİNİN YAPILMASI

## ÖZET

Sarmal çalkantılı jetler, aksenal yöndeki jet akışlara teğetsel hız bileşenlerinin eklenmesi ile oluşur ve endüstriyel uygulamalarda sıkça kullanılır. Örneğin, yanma sistemlerinde hava ve yakıtın türbülanslı karışımlarının iyileştirilmesi, alevin kararlı hale getirilmesi ve soğutma uygulamalarında zorlanmış taşınım olarak kullanılan çalkantılı jet dinamiği, mühendislik uygulamalarındaki önemli ve geniş kullanım sahası nedeniyle sayısal ve deneysel araştırmalarda önemli bir yere sahiptir. Daimi olmayan akış özelliklerinin baskın olduğu çalkantılı jet akışlarında oluşan zamana bağlı etkileşimlerin gerçekleştirilmesi için anlık akış alanının zaman ve uzay ölçeklerinde yüksek çözünürlükte hesaplanması önemli olmaktadır.

Türbülanslı akışların hesaplamalarında kullanılan hesaplamalı akışkanlar dinamiği (HAD) yöntemleri; Doğrudan Sayısal Benzetim (Direct Numerical Simulation – DNS) ve Büyük Ölçekli Yapıların Benzetimi (Large Eddy Simulation – LES), çalkantılı jetlerdeki söz konusu daimi olmayan niteliklerin benzetimi için etkili yöntemler olarak öne çıkmaktadır. Hesaplama kabiliyetlerindeki artış ile birlikte, zamana bağlı, karmaşık, türbülanslı akışların incelenmesi konusunda LES yöntemi son yıllarda oldukça yaygın bir yöntemdir. Yurtdışında birçok kuruluş, karşılaştıkları problemlerin benzetimini en gerçekçi şekilde yapabilmek amacıyla kendi kodlarını geliştirmiştir. Imperial College’da geliştirilen FLOWSI, Sandia Ulusal Laboratuvar’ında geliştirilen RAPTOR, Stanford Üniversitesi’nden CDP ve OpenFOAM gibi birçok örnek verilebilir. Bu kodlarda ikinci merteye uzaysal ayrıklaştırma kullanılmaktadır. Zamanda ikinci veya üçüncü mertebeden integrasyon gerçekleştirilmektedir. Ağ altı ölçek modeli olarak da ağırlıklı olarak Smagorinsky/dinamik Smagorinsky modeli kullanılmaktadır. Ancak bu yöntemlerde karşılaşılan genel problem, giriş sınırında zaman ve konum bağıntılarını doğru tanımlayabilmektir. Akışın geldiği bölge yukarıdaki geçmişinin, aşağıdaki çalkantı dinamiğine doğrudan etki ettiği bilindiğine göre, bir çalkantılı jet akışı benzetimi göz önünde bulundurulduğunda, lüleden çıkış öncesi önem kazanmaktadır. Buradaki akış modlarının uygun bir yöntemle bulunması ile istenen özelliklere sahip giriş koşulları oluşturulabilir. Bu noktada, çapraz konum-zaman ilişkilerini doğru verebilmesi nedeniyle hidrodinamik kararlılık yaklaşımı ve sonucunda elde edilebilecek akışın kendisine ait modlar, giriş koşulu olarak kullanılacak zamana bağlı hız profillerinin oluşturulmasını mümkün kılmaktadır.

Söz konusu probleminin üstesinden gelebilmek için çeşitli yöntemler uygulanmıştır. Hesaplama bölgesinin sınırlarını yeterince uzağa çekmek LES ve DNS benzetimlerinde hesaplama maliyetini %50'lere varan oranlarda artırdığı görülmüştür. Girişte periyodik sınır şartı uygulamak her ne kadar çok pratik ve kullanışlı bir çözüm gibi gözükse de eğer ana akış doğrultusundaki değişimler yeterince küçük değilse bu yöntem uygulanabilirliğini kaybetmektedir.

Yapay çalkantı oluşturmak için kullanılan bir başka yöntem rasgele çalkantı eklenmesidir. Ancak elde edilen verinin enerjisi bütün dalga boylarında eşit olarak dağıldığından, düşük dalga boyu bölgesinde gerekli olan enerji yaratılamamakta ve verilen tedirginlikler kısa mesafede sönümlenmektedir. Türbülanslı akış giriş sınır koşulları üretmek için bir başka yöntem olarak, türbülanslı ortalama akış alanı çevresindeki çalkantıların çeşitli matematiksel modellere göre uygun bir yaklaşımı ile önceden tanımlanmıştır. Bu yöntem yapay türbülans üretimi olarak bilinir. Gerçekçi türbülanslı yapılar oluşturmak için Reynolds gerilmeleri, türbülans kinetik enerjisi spektrumu ve doğru faz ilişkileri mevcut veriler olarak kullanılır. Ek olarak, modelleme hatalarının önüne geçebilmek için daha uzun hesaplama ağı gereklidir.

Bu çalışmada amaç, LES yöntemi uygulanarak yapılacak çalkantılı sarmal jet akışı benzetimlerinde kullanmak amacıyla, giriş sınırında akışta olması istenen çalkantı değerlerinin, hidrodinamik kararlılık yaklaşımından yararlanılarak yeterli doğruluk ile verilebilmesidir. Bu amaç doğrultusunda, çalışmanın ilk bölümünde, tam gelişmiş, çalkantılı bir akışın modları, dairesel kesite sahip bir boru içerisinde hidrodinamik kararlılık yaklaşımı ile incelenmiştir. Bu noktada ilk adım, doğrusallaştırılmış akış denklemlerinin, akış alanı içinde geliştiği düşünülen küçük tedirginlikler için ortaya konulmasıdır. Söz konusu tedirginliklerin gelişen dalgalar şeklinde çözümleri olduğu varsayımı ve gerekli kabullerin yapılması ile bir özdeğer problemi elde edilmiştir. Daha sonra, boyutsuzlaştırılan denklemler indirgenerek, akış alanındaki tedirginlik terimlerini modelleyen ve birinci derece doğrusal kısmi diferansiyel denklemlerden oluşan bir denklem sistemi oluşturulmuştur. Söz konusu denklem sisteminin çözümü için bir ortalama akış profili uygulanmış ve gerekli sınır koşulları belirlenmiştir. Bir sonraki aşamada, özdeğer problemi ilk olarak iki sınıra sahip bir sınır değer problemine dönüştürülmüş ve denklem sistemi ortonormalizasyon koşulu ile kapalı hale getirilmiştir. Daha sonra ise söz konusu kapalı sistem, bir ilk değer problemine dönüştürülerek her iki sınırdaki bilinmeyen değerlerin kestirimi, her iki sınırdan başlayarak ortada seçilen üçüncü noktaya doğru yapılan integrasyon ve burada sağlama gerçekleşene kadar çözümün yinelenmesi esasına dayanan paralel kestirim yöntemi kullanılarak sayısal çözüm yapılmıştır. Bu çözüm sonucunda akış alanına ait Fourier modları elde edilmiş ve yapıları irdelenmiştir.

Çalışmanın ikinci bölümde, elde edilen Fourier modları kullanılarak oluşturulan zamana bağlı hız sinyalleri, eksenel simetrik ve dairesel kesitli bir sarmal hava jetinin LES benzetimlerinde radial, açısız ve eksenel hızlar için giriş koşulu olarak kullanılmıştır. Bu aşamada ilk olarak, jet için ortalama akış parametreleri ile büyük ve küçük ölçekli yapıların türbülans parametreleri hesaplanmıştır. Daha sonra, ANSYS ICEM CFD 18.0 yazılımından yararlanılarak, en küçük kafes büyüklüğü hesaplanan mikro uzunluk ölçeğine uygun olacak şekilde boyutlandırılan, altıyüzlü (hexahedral) elemanlardan oluşan, kesik koni biçiminde yapılandırılmış, 40 boru çapı uzunluğunda, alt ve üst tabanı ise sırasıyla 10 ve 30 boru çapı genişliğinde olan bir hesaplama ağı oluşturulmuştur. Söz konusu hesaplama ağında hava akışı, alt tabanın merkezinde bulunan giriş yüzeyinden başlayarak 1 boru çapı uzunluğundaki kısa bir borudan geçmekte ve boru çıkışında bir jet oluşturmaktadır. Söz konusu hesaplama ağı kullanılarak, giriş sınırında ortalama hız profili, çıkış sınır koşulu olarak ise kesik koninin her bir yüzeyinde atmosferik basınç ve taşınım sınır koşullarının uygulandığı bir LES benzetimi yapılmıştır. Bu benzetimde giriş yüzeyinde başkaca bir çalkantı yapısı uygulanmamıştır. Daha sonra, aynı hesaplama ağı ve çıkış sınır koşulları kullanılarak, bu kez girişte çalkantı yapısı olarak, elde edilen zamana bağlı çalkantı sinyallerinin deneysel veriye uygun çalkantı yoğunluğu ile uygulandığı bir LES

benzetimi yapılmıştır. Bu benzetimde, Fourier modları üstüste toplanarak radial, açısız ve aksel hızlar için zamana bağı giriş verileri oluşturulmuş, radyal yöndeki hız verisi giriş sınırında doğruca uygulanırken, açısız ve aksel yöndeki hız verileri uygulanmadan önce ortalama akış profili ile üst üste bindirilmiştir. Tüm LES benzetimlerde için ANSYS FLUENT 18.0 yazılımından yararlanılmış, mikro ölçekli yapıların modellenmesi için dinamik Smogorinsky modeli kullanılmıştır. Tüm benzetimlerin başlangıcında, giriş yüzeyindeki ortalama hız profili, boru boyunca gerçekleşen sınır tabaka gelişimi nedeniyle duvar yakınında düzenlenerek, jetin çıkışında deneysel veriye uygun ortalama akış profili elde edilmesi sağlanmıştır. Yine tüm benzetimlerde zaman adımı, akışın mikro zaman ölçeğine uygun şekilde seçilmiş ve sabit olarak alınmıştır. Benzetimler, akışın istatistiksel olarak kararlı duruma ulaşabilmesi için ilk olarak 4000 zaman adımı koşulmuş, daha sonra zaman ortalama değerleri elde edebilmek amacıyla örnekleme işlemi 5000 zaman adımı süresi boyunca yapılmıştır.

Çalışmanın son bölümünde, iki LES benzetiminin sonuçları deneysel veriler ile karşılaştırılmıştır. Aksel yöndeki ortalama akış göz önünde bulundurulduğunda, dört benzetimin de birbirine benzer ve deneysel veriye kısmen yakın sonuçlar verdiği görülmüştür. Her iki benzetim için geçerli olacak şekilde, tüm aksel yöndeki konumlarda, deneysel jetin daha yüksek yayılım gösterdiği ve giriş koşulu olarak verilen radyal yöndeki hız sinyalinin jet yayılımına gözle görülür bir etkisi olmadığı saptanmıştır. Jetin merkez çizgisi üzerinde ise, tüm benzetimler ve ölçüm değerleri arasında yeterli uygunluk gözlemlenmiştir. Sonuçlar çalkantı yoğunluğu açısından irdelendiğinde, genel olarak çalkantılı giriş koşulu uygulanan benzetimlerin, sadece ortalama akış profili uygulanan benzetime göre ölçüm değerlerine çok daha yakın veriler sağladığı saptanmıştır. Söz konusu çalkantılı giriş koşulu uygulanan benzetimler kendi aralarında karşılaştırıldığında ise, girişte verilen hız verisi nedeniyle oluşan yüksek türbülans yoğunluğunun, jet çıkışının yakınında sönmüldüğü gözlemlenmiş, giriş sınırında 15% türbülans yoğunluğu uygulanan benzetimin genel olarak diğer benzetimle oranla daha iyi sonuçlara sahip olduğu görülmüştür. Son olarak, bu çalışmada kullanılan yöntemin doğrusal olmayan terimleri göz ardı etmeden, daha gerçekçi sonuçlar verebilecek şekilde geliştirebileceği anlaşılmıştır.



# 1. INTRODUCTION

## 1.1 Purpose and Relevance

Turbulent swirling jet flows are of considerable practical importance in many industrial applications, for instance, in aeronautics, combustion, heating and cooling, mixing enhancement and noise suppression (Yang et al., 2016). During the last two decades, the advancements in computer technologies made simulations of complex turbulent flows affordable even with a moderate computing power, which also made computational Fluid Mechanics (CFD) a feasible alternative to expensive experiments. Direct Numerical Simulation (DNS) is capable of resolving the whole length scales of a given flow, which makes it the most accurate but computationally expensive method: The required for mesh resolution sharply increases with the flow Reynolds number and, therefore, the DNS computations are now feasible only at low Reynolds numbers and simple geometries. In high Reynolds number flows, Reynolds-Averaged Navier-Stokes (RANS) approach has been very common. Although the RANS is one of the cheapest and oldest approaches in turbulence modelling, it is incapable of simulating complex turbulent flows with sufficient accuracy.

An alternative approach between DNS and RANS is Large Eddy Simulation (LES), in which large-scale structures are fully resolved while the small sub-grid scales are modelled. LES also offers a good compromise between the high cost of the DNS and poor accuracy of RANS. Hence, it has become very popular in studying time-varying complex turbulent flows. These flows are, however, highly dependent on physically realistic boundary conditions, in that particularly the inflow boundary is of utmost importance. If the inflow conditions are inconsistent and are not well prescribed in time, LES computations present a significant decay of fluctuations further down in the flow. Hence, the accuracy of the entire LES simulation of turbulent flows is highly dependent on the proper definition of the inflow including instantaneous fluctuations.

It is evident that the downstream flow dynamics are directly related to the turbulent fluctuations existed at the inflow boundary, it is essential to define correct upstream

modes for the proper evolution of turbulent flow in the region where large eddies are resolved (Schlichting, 1979). Therefore, if we want to make LES of the swirling turbulent jets and resolve fluctuations, it is then vital to generate the proper turbulent inflow conditions with appropriate time and space correlations. In this regard, the nozzle flow upstream of the jet exit becomes significant. According to Rosenhead (1963), it is viable to simplify the nozzle geometry into a basic pipe structure and to scale the downstream jet flow with the turbulent structures in pipe flow. Thus, by determining the modes of the flow inside the pipe, one can generate the necessary inflow fluctuations to obtain desired turbulent flow characteristics of the swirling turbulent jets further downstream.

The hydrodynamic stability concept is usually exploited to determine the onset of instability and transition to turbulence in fluid flows. The simplest approach to describe the stability conditions in a flow is the use of linear stability analysis, in which the equations of motions and boundary conditions are linearized for sufficiently small disturbances in the flow field. The idea here is to resolve the small perturbations into separate Fourier modes and find necessary eigenvalues of the linear equation system to identify the stability conditions of corresponding disturbances (Drazin and Reid, 2004). Moreover, by solving the equations numerically with a suitable method, and finding normal modes of the system, it is mathematically possible to superpose the modes together to generate the related time-dependent disturbance with the correct space-time correlations.

The purpose of this study is to generate proper and sufficiently accurate inflow boundary conditions using hydrodynamic stability approach and to perform LES of a swirling turbulent jet. The goal is achieved in two stages: In the first stage, the stability of the flow in a circular pipe (representing the nozzle) was analyzed by linearized equations of motion, which were then solved with a method (parallel shooting) to obtain Fourier modes representing the fluctuations. In the second stage, by using these modes, the instantaneous velocity profile with correct space-time correlations were obtained, which was then applied as an inflow boundary condition in several LES simulations of an incompressible, axisymmetric turbulent swirling jet. Finally, the results were discussed in comparison with the experimental data (Örlü and Alfredsson, 2008).

## 1.2 Literature Review

To overcome the difficulties associated with defining proper inflow boundary conditions, various methods have been developed (Dhamankar et al., 2018). The use of periodic boundary conditions appears as one of these methods, where the data from flow downstream can be feedback at the inlet and so the flow pattern repeats itself periodically (Spalart, 1988). This kind of boundary condition is often used for fully developed time-evolving flows, which are homogeneous in the axial direction. In such flows, there is an equilibrium between mean flow and time-dependent fluctuations, and this satisfies the momentum equations (Lund et al, 1988). However, this approach loses its feasibility for flows where the mean variation downstream is not small enough in comparison with the variation in the transverse direction (Moin and Mahesh, 1998). Therefore, the use of the periodic boundary is not suitable for flows, which evolve spatially like turbulent boundary layers and jets. The simulation of spatially developing turbulent flows is, however, possible with a more common and direct method in which the computation is initiated with a laminar profile in an upstream region sufficiently far so that the transition to turbulence downstream occurs naturally (Dhamankar et al., 2018). Even though this approach is advantageous since using turbulent fluctuations at the inlet is unnecessary, it is not a computationally efficient procedure due the requirement of long development section (Sagaut, 2002).

Another method to produce turbulent inflow boundary conditions is known as the synthetic turbulence generation. Superimposing random fluctuations on a mean turbulent velocity profile is the simplest of these approaches to define turbulent inflow conditions, in which by adjusting the fluctuation amplitudes, it is possible to obtain desired second-order flow characteristics (Moin and Mahesh, 1998). However, randomly generated fluctuations lack proper phase relations (Keating et al, 2004) without which, it is not possible to sustain high order correlations and create a realistic turbulent flow structure (Lund et al, 1988). In addition, when the energy distribution of random signals is uniform over the entire wavenumber range, the energy of low wavenumber range mostly remains below the required level. As a result, the random fluctuations applied at inflow boundary are damped in a short distance downstream and eventually exhibit laminar inflow characteristics (Klein et al, 2003). It is also possible that fluctuations around a turbulent mean profile are predefined with an appropriate method based on various mathematical models. However, these models in

general, require Reynolds stresses, the spectrum of turbulent kinetic energy and correct phase relations as preexisting data to create realistic turbulent structures (Dhamankar, 2015). Additionally, longer computational domains are also necessary, so that the turbulent flow can recover from modelling errors (Tabor and Baba-Ahmadi, 2010).

One of the procedures to develop turbulent conditions at the inflow boundary is to run a synchronized second simulation. Hence, at each time step, one can extract a planar flow field information at a specific location downstream to be used as an inflow condition in the main simulation. Even though running two simultaneous simulations seems to be computationally expensive, it is an effective method and offers a conceivable variety of approximations and modifications, which can be made in the auxiliary simulation to obtain desired flow properties (Otero, 2009).

### **1.3 Stability of Swirling Jet Flows**

There has been a vast amount of the numerical and experimental studies devoted to the swirling jet flow configuration because it has been one of the most important complex fluid problems. Swirling jets ubiquitous in numerous natural phenomena and engineering applications. For instance, swirling flows are encountered in meteorological events such as tornadoes and dust devils (Wu et al., 2015). As well as in technical applications like wingtip vortices behind aircraft wings (Morse, 1980). In advanced combustion systems, specifically in diesel engines, the swirl in the spray jets enhances mixing characteristics, leading to flame stabilization and improvement in the combustion efficiency. They are also widely used in cyclone separators or heat exchangers due to their unique characteristics (Vaidya et al., 2011). Since the first discovery of the coherent structures in jet flows by Crow and champagne (1971) swirling flows due to their complex flow dynamics such as vortex breakdown, Precessing Vortex Core (PVC) and helical flow instabilities (Oberleithner, 2012; Mishra, 2018; Müller et al., 2020)) draw a significant attention and become a benchmark for instability researches in the past decades (Syred, 2006; Lu et al., 2005; Villalba, 2004).

The hydrodynamic stability concept is usually exploited to determine the onset of instability and transition to turbulence in fluid flows. The simplest approach to describe the stability conditions in a flow is the use of linear stability analysis, in which the equations of motions and boundary conditions are linearized for sufficiently small

disturbances in the flow field. The linear stability theory is one of the intriguing subjects of fluid mechanics which has been of growing interest for over a hundred years. The problem of jet instability was first studied theoretically by Lord Rayleigh back in 1879 where he analyzed and formulized the instability of inviscid circular jet for axisymmetric perturbation and paved the way to the extensive studies of the stability of the jets flows. (Rayleigh, 1879).

In the mid 20<sup>th</sup> century, rapid advancement in the aviation industry and the introduction of turbojet engines spurred numerous researches on the hydrodynamic stability of turbulent jet flows. (Lessen, 1975; Michalke, 1985). Batchelor and Gill (1962) for the first time conducted the mathematical linear stability analysis of steady axisymmetric parallel jet flows, they found that all axisymmetric and non-axisymmetric modes are unstable for top-hat jet profiles (Lessen 1975, Batchelor and Gill 1962). An earlier investigation of linear stability analysis was mostly based on the temporal evolution of disturbances (Wu and Farokhi, 1991; Qadri, 2013). In temporal stability analysis, the wavenumber is taken as real and dispersion relation from linear theory is solved for unknown complex frequency. (Huerre and Monkewitz, 1990). This type of stability is mostly used in bounded flows like Taylor-Couette flow (Huerre and Monkewitz, 1985; Paschereit et al., 2014). On the other hand, for the unbounded shear flows like jets and wakes, the spatially growing disturbances results in much more consistent with experimental outcomes than temporal stability theory. (Michalke, 1965; Garg and Rouleau, 1972; Huerre and Monkewitz, 1985). In spatial linear stability theory, the frequency is constrained to be a real number, and the eigenvalue problem sought for complex wavenumber (Paschereit et al., 2014; Michalke, 1965). The third methodology, in which disturbances may grow in both time and space is referred to linear Spatio-temporal stability analyses. In the context of this approach, the linear stability analysis bifurcates into the absolute and convective instability (Huerre and Monkewitz, 1990; Balestra, 2013; Loiseau, 2015). In the flow region if the linear response to a certain perturbation spreads upstream and downstream and ultimately contaminating the whole domain is considered to be locally absolute unstable. In contrast, if the perturbation is swept downstream away from the source, the flow is regarded as convectively unstable, such flows behave as noise amplifiers (Huerre and Monkewitz, 1990; Paschereit et al., 2014; Loiseau, 2015). Thus, in Spatio-temporal stability analyses both angular frequency and wavenumber is taken as complex

numbers. This type of stability analyses is mostly applicable to open shear flows such as hot jets, wakes and strong swirling jets (Monkewitz and Sohn, 1988, Paschereit et al., 2014)

.

## 2. HYDRODYNAMIC STABILITY ANALYSIS OF SWIRLING PIPE FLOW

The present investigation focuses on the solution of the equations of motion of a swirling jet flow emanating from a fully developed axially rotating pipe. This means that the history of the swirling jet perturbations is rooted in the pipe flow. In the following, the equations of motion for a cylindrical pipe flow system will be linearized and decomposed into normal modes with the corresponding eigenfunctions and the assumptions made will be elaborated. Then, in order to close the system of equations, the physical and numerical boundary conditions of this system will be defined. The numerical method used for the solution is explained in the next section.

### 2.1 Reynolds Decomposition and Linearization of the Navier-Stokes Equations

The equations of motion for a fully developed axially rotating pipe flow is based on the incompressible axisymmetric flow assumption and written for a cylindrical inertial frame of reference as,

Continuity equation:

$$\frac{\partial U_r}{\partial r} + \frac{1}{r} U_r + \frac{1}{r} \frac{\partial U_\phi}{\partial \phi} + \frac{\partial U_z}{\partial z} = 0 \quad (2.1a)$$

Momentum equations:

$r$  – momentum:

$$\begin{aligned} & \frac{\partial U_r}{\partial t} + U_r \frac{\partial U_r}{\partial r} + \frac{U_\phi}{r} \frac{\partial U_r}{\partial \phi} - \frac{U_\phi^2}{r} + U_z \frac{\partial U_r}{\partial z} \\ & = -\frac{1}{\rho} \frac{\partial P}{\partial r} + \nu \left[ \frac{\partial^2 U_r}{\partial r^2} + \frac{1}{r} \frac{\partial U_r}{\partial r} + \frac{1}{r^2} \frac{\partial^2 U_r}{\partial \phi^2} - \frac{2}{r^2} \frac{\partial U_\phi}{\partial \phi} - \frac{U_r}{r^2} + \frac{\partial^2 U_r}{\partial z^2} \right] \end{aligned} \quad (2.1b)$$

$\phi$  – momentum:

$$\begin{aligned} \frac{\partial U_\phi}{\partial t} + U_r \frac{\partial U_\phi}{\partial r} + \frac{U_\phi}{r} \frac{\partial U_\phi}{\partial \phi} + \frac{U_r U_\phi}{r} + U_z \frac{\partial U_\phi}{\partial z} \\ = -\frac{1}{\rho} \frac{\partial P}{\partial \phi} + \nu \left[ \frac{\partial^2 U_\phi}{\partial r^2} + \frac{1}{r} \frac{\partial U_\phi}{\partial r} + \frac{1}{r^2} \frac{\partial^2 U_\phi}{\partial \phi^2} + \frac{2}{r^2} \frac{\partial U_r}{\partial \phi} - \frac{U_\phi}{r^2} + \frac{\partial^2 U_\phi}{\partial z^2} \right] \end{aligned} \quad (2.1c)$$

$z$  – momentum:

$$\begin{aligned} \frac{\partial U_z}{\partial t} + U_r \frac{\partial U_z}{\partial r} + \frac{U_\phi}{r} \frac{\partial U_z}{\partial \phi} + U_z \frac{\partial U_z}{\partial z} \\ = -\frac{1}{\rho} \frac{\partial P}{\partial z} + \nu \left[ \frac{\partial^2 U_z}{\partial r^2} + \frac{1}{r} \frac{\partial U_z}{\partial r} + \frac{1}{r^2} \frac{\partial^2 U_z}{\partial \phi^2} + \frac{\partial^2 U_z}{\partial z^2} \right] \end{aligned} \quad (2.1d)$$

Using Reynolds double decomposition formalism (Tennekes & Lumley, 1972), the instantaneous flow field can be considered as the summation of time-averaged quantities and their fluctuation components. Then, it is possible to express velocity components and pressure as,

$$U_r(r, \phi, z, t) = \overline{U_r}(r, \phi, z, t) + u'_r(r, \phi, z, t) \quad (2.2a)$$

$$U_\phi(r, \phi, z, t) = \overline{U_\phi}(r, \phi, z, t) + u'_\phi(r, \phi, z, t) \quad (2.2b)$$

$$U_z(r, \phi, z, t) = \overline{U_z}(r, \phi, z, t) + u'_z(r, \phi, z, t) \quad (2.2c)$$

$$P(r, \phi, z, t) = \overline{P}(r, \phi, z, t) + p'(r, \phi, z, t) \quad (2.2d)$$

where the terms with over-bar and primes denote mean and fluctuation parts, respectively. Applying the expansions 2.2a-d into the equations 2.1a-d leads to the following equations,

Continuity:

$$\frac{\partial(\overline{U_r} + u'_r)}{\partial r} + \frac{1}{r}(\overline{U_r} + u'_r) + \frac{1}{r} \frac{\partial(\overline{U_\phi} + u'_\phi)}{\partial \phi} + \frac{\partial(\overline{U_z} + u'_z)}{\partial z} = 0 \quad (2.3a)$$

$r$  – momentum:

$$\begin{aligned}
& \frac{\partial(\overline{U}_r + u'_r)}{\partial t} + (\overline{U}_r + u'_r) \frac{\partial(\overline{U}_r + u'_r)}{\partial r} + \frac{(\overline{U}_\phi + u'_\phi)}{r} \frac{\partial(\overline{U}_r + u'_r)}{\partial \phi} \\
& \quad - \frac{(\overline{U}_\phi + u'_\phi)^2}{r} + (\overline{U}_z + u'_z) \frac{\partial(\overline{U}_r + u'_r)}{\partial z} \\
& = -\frac{1}{\rho} \frac{\partial(\overline{P} + p')}{\partial r} + v \left[ \frac{\partial^2(\overline{U}_r + u'_r)}{\partial r^2} + \frac{1}{r} \frac{\partial(\overline{U}_r + u'_r)}{\partial r} + \frac{1}{r^2} \frac{\partial^2(\overline{U}_r + u'_r)}{\partial \phi^2} \right] \\
& \quad + v \left[ -\frac{2}{r^2} \frac{\partial(\overline{U}_\phi + u'_\phi)}{\partial \phi} - \frac{(\overline{U}_r + u'_r)}{r^2} + \frac{\partial^2(\overline{U}_r + u'_r)}{\partial z^2} \right] \tag{2.3b}
\end{aligned}$$

$\phi$  – momentum:

$$\begin{aligned}
& \frac{\partial(\overline{U}_\phi + u'_\phi)}{\partial t} + (\overline{U}_r + u'_r) \frac{\partial(\overline{U}_\phi + u'_\phi)}{\partial r} + \frac{(\overline{U}_\phi + u'_\phi)}{r} \frac{\partial(\overline{U}_\phi + u'_\phi)}{\partial \phi} \\
& \quad + \frac{(\overline{U}_r + u'_r)(\overline{U}_\phi + u'_\phi)}{r} + (\overline{U}_z + u'_z) \frac{\partial(\overline{U}_\phi + u'_\phi)}{\partial z} \\
& = -\frac{1}{\rho r} \frac{\partial(\overline{P} + p')}{\partial \phi} + v \left[ \frac{\partial^2(\overline{U}_\phi + u'_\phi)}{\partial r^2} + \frac{1}{r} \frac{\partial(\overline{U}_\phi + u'_\phi)}{\partial r} + \frac{1}{r^2} \frac{\partial^2(\overline{U}_\phi + u'_\phi)}{\partial \phi^2} \right] \\
& \quad + v \left[ \frac{2}{r^2} \frac{\partial(\overline{U}_r + u'_r)}{\partial \phi} - \frac{(\overline{U}_\phi + u'_\phi)}{r^2} + \frac{\partial^2(\overline{U}_\phi + u'_\phi)}{\partial z^2} \right] \tag{2.3c}
\end{aligned}$$

$z$  – momentum:

$$\begin{aligned}
& \frac{\partial(\overline{U}_z + u'_z)}{\partial t} + (\overline{U}_r + u'_r) \frac{\partial(\overline{U}_z + u'_z)}{\partial r} + \frac{(\overline{U}_\phi + u'_\phi)}{r} \frac{\partial(\overline{U}_z + u'_z)}{\partial \phi} \\
& + (\overline{U}_z + u'_z) \frac{\partial(\overline{U}_z + u'_z)}{\partial z} = -\frac{1}{\rho} \frac{\partial(\overline{P} + p')}{\partial z} + v \left[ \frac{\partial^2(\overline{U}_z + u'_z)}{\partial r^2} + \frac{1}{r} \frac{\partial(\overline{U}_z + u'_z)}{\partial r} \right] \\
& \quad + v \left[ \frac{1}{r^2} \frac{\partial^2(\overline{U}_z + u'_z)}{\partial \phi^2} + \frac{\partial^2(\overline{U}_z + u'_z)}{\partial z^2} \right] \tag{2.3d}
\end{aligned}$$

Applying the averaging operator on the equations 2.3a-d over a sufficiently long period  $T$ , the governing equations for the flow become time-independent and following Reynolds-averaged continuity and Navier-Stokes equations (RANS) are obtained,

Continuity:

$$\frac{\partial \overline{U}_r}{\partial r} + \frac{1}{r} \overline{U}_r + \frac{1}{r} \frac{\partial \overline{U}_\phi}{\partial \phi} + \frac{\partial \overline{U}_z}{\partial z} = 0 \quad (2.4a)$$

$r$  – momentum:

$$\begin{aligned} & \frac{\partial \overline{U}_r}{\partial t} + \overline{U}_r \frac{\partial \overline{U}_r}{\partial r} + \overline{u'_r} \frac{\partial \overline{u}'_r}{\partial r} + \frac{\overline{U}_\phi}{r} \frac{\partial \overline{U}_r}{\partial \phi} + \frac{\overline{u'_\phi}}{r} \frac{\partial \overline{u}'_r}{\partial \phi} - \overline{U}_\phi \frac{\overline{U}_\phi}{r} \\ & \quad - \frac{\overline{u'_\phi u'_\phi}}{r} + \overline{U}_z \frac{\partial \overline{U}_r}{\partial z} + \overline{u'_z} \frac{\partial \overline{u}'_r}{\partial z} \\ & = -\frac{1}{\rho} \frac{\partial \overline{P}}{\partial r} + \nu \left[ \frac{\partial^2 \overline{U}_r}{\partial r^2} + \frac{1}{r} \frac{\partial \overline{U}_r}{\partial r} + \frac{1}{r^2} \frac{\partial^2 \overline{U}_r}{\partial \phi^2} - \frac{2}{r^2} \frac{\partial \overline{U}_\phi}{\partial \phi} - \frac{\overline{U}_r}{r^2} + \frac{\partial^2 \overline{U}_r}{\partial z^2} \right] \end{aligned} \quad (2.4b)$$

$\phi$  – momentum:

$$\begin{aligned} & \frac{\partial \overline{U}_\phi}{\partial t} + \overline{U}_r \frac{\partial \overline{U}_\phi}{\partial r} + \overline{u'_r} \frac{\partial \overline{u}'_\phi}{\partial r} + \frac{\overline{U}_\phi}{r} \frac{\partial \overline{U}_\phi}{\partial \phi} + \frac{\overline{u'_\phi}}{r} \frac{\partial \overline{u}'_\phi}{\partial \phi} \\ & \quad + \overline{U}_r \frac{\overline{U}_\phi}{r} + \frac{\overline{u'_r u'_\phi}}{r} + \overline{U}_z \frac{\partial \overline{U}_\phi}{\partial z} + \overline{u'_z} \frac{\partial \overline{u}'_\phi}{\partial z} \\ & = -\frac{1}{\rho} \frac{\partial \overline{P}}{\partial \phi} + \nu \left[ \frac{\partial^2 \overline{U}_\phi}{\partial r^2} + \frac{1}{r} \frac{\partial \overline{U}_\phi}{\partial r} + \frac{1}{r^2} \frac{\partial^2 \overline{U}_\phi}{\partial \phi^2} + \frac{2}{r^2} \frac{\partial \overline{U}_r}{\partial \phi} - \frac{\overline{U}_\phi}{r^2} + \frac{\partial^2 \overline{U}_\phi}{\partial z^2} \right] \end{aligned} \quad (2.4c)$$

$z$  – momentum:

$$\begin{aligned} & \frac{\partial \overline{U}_z}{\partial t} + \overline{U}_r \frac{\partial \overline{U}_z}{\partial r} + \overline{u'_r} \frac{\partial \overline{u}'_z}{\partial r} + \frac{\overline{U}_\phi}{r} \frac{\partial \overline{U}_z}{\partial \phi} + \frac{\overline{u'_\phi}}{r} \frac{\partial \overline{u}'_z}{\partial \phi} + \overline{U}_z \frac{\partial \overline{U}_z}{\partial z} + \overline{u'_z} \frac{\partial \overline{u}'_z}{\partial z} \\ & = -\frac{1}{\rho} \frac{\partial \overline{P}}{\partial z} + \nu \left[ \frac{\partial^2 \overline{U}_z}{\partial r^2} + \frac{1}{r} \frac{\partial \overline{U}_z}{\partial r} + \frac{1}{r^2} \frac{\partial^2 \overline{U}_z}{\partial \phi^2} + \frac{\partial^2 \overline{U}_z}{\partial z^2} \right] \end{aligned} \quad (2.4d)$$

Extracting RANS equations 2.4a-d from equations 2.3a-d, yields the following equations, which are representing the motion of the fluctuation components.

$$\frac{\partial \overline{u}'_r}{\partial r} + \frac{1}{r} \overline{u}'_r + \frac{1}{r} \frac{\partial \overline{u}'_\phi}{\partial \phi} + \frac{\partial \overline{u}'_z}{\partial z} = 0 \quad (2.5a)$$

$$\begin{aligned}
& \frac{\partial u'_r}{\partial t} + \overline{U_r} \frac{\partial u'_r}{\partial r} + u'_r \frac{\partial \overline{U_r}}{\partial r} + u'_r \frac{\partial u'_r}{\partial r} - \overline{u'_r \frac{\partial u'_r}{\partial r}} + \frac{\overline{U_\phi}}{r} \frac{\partial u'_r}{\partial \phi} + \frac{u'_\phi}{r} \frac{\partial \overline{U_r}}{\partial \phi} \\
& \quad + \frac{u'_\phi}{r} \frac{\partial u'_r}{\partial \phi} - \frac{\overline{u'_\phi \frac{\partial u'_r}{\partial \phi}}}{r} - 2\overline{U_\phi} \frac{u'_\phi}{r} - \frac{u'_\phi u'_\phi}{r} + \frac{\overline{u'_\phi u'_\phi}}{r} \\
& \quad + \overline{U_z} \frac{\partial u'_r}{\partial z} + u'_z \frac{\partial \overline{U_r}}{\partial z} + u'_z \frac{\partial u'_r}{\partial r} - \overline{u'_z \frac{\partial u'_r}{\partial r}} \\
& = -\frac{1}{\rho} \frac{\partial p'}{\partial r} + v \left[ \frac{\partial^2 u'_r}{\partial r^2} + \frac{1}{r} \frac{\partial u'_r}{\partial r} + \frac{1}{r^2} \frac{\partial^2 u'_r}{\partial \phi^2} - \frac{2}{r^2} \frac{\partial u'_\phi}{\partial \phi} - \frac{u'_r}{r^2} + \frac{\partial^2 u'_r}{\partial z^2} \right]
\end{aligned} \tag{2.5b}$$

$$\begin{aligned}
& \frac{\partial u'_\phi}{\partial t} + \overline{U_r} \frac{\partial u'_\phi}{\partial r} + u'_r \frac{\partial \overline{U_\phi}}{\partial r} + u'_r \frac{\partial u'_\phi}{\partial r} - \overline{u'_r \frac{\partial u'_\phi}{\partial r}} + \frac{\overline{U_\phi}}{r} \frac{\partial u'_\phi}{\partial \phi} + \frac{u'_\phi}{r} \frac{\partial \overline{U_\phi}}{\partial \phi} \\
& \quad + \frac{u'_\phi}{r} \frac{\partial u'_\phi}{\partial \phi} - \frac{\overline{u'_\phi \frac{\partial u'_\phi}{\partial \phi}}}{r} + \overline{U_r} \frac{u'_\phi}{r} + u'_r \frac{\overline{U_\phi}}{r} + \frac{u'_r u'_\phi}{r} \\
& \quad - \frac{\overline{u'_r u'_\phi}}{r} + \overline{U_z} \frac{\partial u'_\phi}{\partial z} + u'_z \frac{\partial \overline{U_\theta}}{\partial z} + u'_z \frac{\partial u'_\phi}{\partial z} - \overline{u'_z \frac{\partial u'_\phi}{\partial z}} \\
& = -\frac{1}{\rho} \frac{1}{r} \frac{\partial p'}{\partial \phi} + v \left[ \frac{\partial^2 u'_\phi}{\partial r^2} + \frac{1}{r} \frac{\partial u'_\phi}{\partial r} + \frac{1}{r^2} \frac{\partial^2 u'_\phi}{\partial \phi^2} + \frac{2}{r^2} \frac{\partial u'_r}{\partial \phi} - \frac{u'_\phi}{r^2} + \frac{\partial^2 u'_\phi}{\partial z^2} \right]
\end{aligned} \tag{2.5c}$$

$$\begin{aligned}
& \frac{\partial u'_z}{\partial t} + \overline{U_r} \frac{\partial u'_z}{\partial r} + u'_r \frac{\partial \overline{U_z}}{\partial r} + u'_r \frac{\partial u'_z}{\partial r} - \overline{u'_r \frac{\partial u'_z}{\partial r}} + \frac{\overline{U_\phi}}{r} \frac{\partial u'_z}{\partial \phi} + \frac{u'_\phi}{r} \frac{\partial \overline{U_z}}{\partial \phi} \\
& \quad + \frac{u'_\phi}{r} \frac{\partial u'_z}{\partial \phi} - \frac{\overline{u'_\phi \frac{\partial u'_z}{\partial \phi}}}{r} + \overline{U_z} \frac{\partial u'_z}{\partial z} + u'_z \frac{\partial \overline{U_z}}{\partial z} + u'_z \frac{\partial u'_z}{\partial z} - \overline{u'_z \frac{\partial u'_z}{\partial z}} \\
& = -\frac{1}{\rho} \frac{\partial p'}{\partial z} + v \left[ \frac{\partial^2 u'_z}{\partial r^2} + \frac{1}{r} \frac{\partial u'_z}{\partial r} + \frac{1}{r^2} \frac{\partial^2 u'_z}{\partial \phi^2} + \frac{\partial^2 u'_z}{\partial z^2} \right]
\end{aligned} \tag{2.5d}$$

Furthermore, by assuming:

- Quadratic and higher order perturbation terms are sufficiently small to be neglected.
- Mean radial velocity is zero.

$$\overline{U_r} = 0 \tag{2.6a}$$

- The mean flow is axisymmetric so that the partial derivatives of the mean velocities in the  $\phi$  direction are equal to zero.

$$\frac{\partial(\overline{U}_i)}{\partial\phi} = 0 \quad (2.6b)$$

- The mean flow in the pipe is fully developed in  $z$  direction, so that the partial derivatives of mean velocities in axial direction are equal to zero.

$$\frac{\partial(\overline{U}_i)}{\partial z} = 0 \quad (2.6c)$$

we obtain,

$$\frac{\partial u'_r}{\partial r} + \frac{1}{r} u'_r + \frac{1}{r} \frac{\partial u'_\phi}{\partial \phi} + \frac{\partial u'_z}{\partial z} = 0 \quad (2.7a)$$

$$\begin{aligned} \frac{\partial u'_r}{\partial t} + \frac{\overline{U}_\phi}{r} \frac{\partial u'_r}{\partial \phi} - 2\overline{U}_\phi \frac{u'_\phi}{r} + \overline{U}_z \frac{\partial u'_r}{\partial z} \\ = -\frac{1}{\rho} \frac{\partial p'}{\partial r} + v \left[ \frac{\partial^2 u'_r}{\partial r^2} + \frac{1}{r} \frac{\partial u'_r}{\partial r} + \frac{1}{r^2} \frac{\partial^2 u'_r}{\partial \phi^2} - \frac{2}{r^2} \frac{\partial u'_\phi}{\partial \phi} - \frac{u'_r}{r^2} + \frac{\partial^2 u'_r}{\partial z^2} \right] \end{aligned} \quad (2.7b)$$

$$\begin{aligned} \frac{\partial u'_\phi}{\partial t} + u'_r \frac{\partial \overline{U}_\phi}{\partial r} + u'_r \frac{\overline{U}_\phi}{r} + \frac{\overline{U}_\phi}{r} \frac{\partial u'_\phi}{\partial \phi} + \overline{U}_z \frac{\partial u'_\phi}{\partial z} \\ = -\frac{1}{\rho} \frac{\partial p'}{\partial \phi} + v \left[ \frac{\partial^2 u'_\phi}{\partial r^2} + \frac{1}{r} \frac{\partial u'_\phi}{\partial r} + \frac{1}{r^2} \frac{\partial^2 u'_\phi}{\partial \phi^2} + \frac{2}{r^2} \frac{\partial u'_r}{\partial \phi} - \frac{u'_\phi}{r^2} + \frac{\partial^2 u'_\phi}{\partial z^2} \right] \end{aligned} \quad (2.7c)$$

$$\begin{aligned} \frac{\partial u'_z}{\partial t} + u'_r \frac{\partial \overline{U}_z}{\partial r} + \frac{\overline{U}_\phi}{r} \frac{\partial u'_z}{\partial \phi} + \overline{U}_z \frac{\partial u'_z}{\partial z} \\ = -\frac{1}{\rho} \frac{\partial p'}{\partial z} + v \left[ \frac{\partial^2 u'_z}{\partial r^2} + \frac{1}{r} \frac{\partial u'_z}{\partial r} + \frac{1}{r^2} \frac{\partial^2 u'_z}{\partial \phi^2} + \frac{\partial^2 u'_z}{\partial z^2} \right] \end{aligned} \quad (2.7d)$$

## 2.2 Normal Mode Expansion and Modal Equations

In order to define the perturbations in any flow field precisely, a complete set of wave spectra is required (Boiko et al, 2002). The completeness of the problem requires self-adjointness of the equation system (Weigand, 2015). The dynamic modes developing in bounded domains, like in pipe flows, are generally continuous modes and they can represent the turbulent structures in the flow field (Özdemir, 1996). The next step is to define these fluctuations in normal modes as,

$$u'_r = A_r(r) \exp\{i(k_r r + k_\phi \phi + k_z z - \omega t)\} + (*) \quad (2.8a)$$

$$u'_\phi = A_\phi(r) \exp\{i(k_r r + k_\phi \phi + k_z z - \omega t)\} + (*) \quad (2.8b)$$

$$u'_z = A_z(r) \exp\{i(k_r r + k_\phi \phi + k_z z - \omega t)\} + (*) \quad (2.8c)$$

$$p' = A_p(r) \exp\{i(k_r r + k_\phi \phi + k_z z - \omega t)\} + (*) \quad (2.8d)$$

where (\*) denotes complex conjugate terms.  $A_r$ ,  $A_\phi$ ,  $A_z$  and  $A_p$  are the complex eigenfunctions;  $\omega$ ,  $k_r$  and  $k_\phi$  are the real eigenvalues denoting frequency and wavenumbers in the  $r$  and  $\phi$  directions, respectively. Assuming that the modes are growing or decaying spatially only in the axial direction, the relevant eigenvalue  $k_z = k_{zr} + ik_{zi}$  needs to be a complex variable ( $k_{zr}$  and  $k_{zi}$  are the real and imaginary parts of  $k_z$ , respectively) denoting the wavenumber in the  $z$  direction.

Applying the normal modes in 2.8a-d into equations 2.7a-d, yields

$$\frac{dA_r}{dr} + ik_r A_r + \frac{A_r}{r} + \frac{1}{r} ik_\phi A_\phi + ik_z A_z = 0 \quad (2.9a)$$

$$\begin{aligned} -i\omega A_r + \frac{\overline{U}_\phi}{r} ik_\phi A_r - 2\overline{U}_\phi \frac{A_\phi}{r} + ik_z \overline{U}_z A_r + \frac{1}{\rho} \left( ik_r A_p + \frac{dA_p}{dr} \right) \\ = v \left[ \frac{d^2 A_r}{dr^2} + 2ik_r \frac{dA_r}{dr} - k_r^2 A_r + \frac{1}{r} \left( \frac{dA_r}{dr} + ik_r A_r \right) \right] \\ + v \left[ -\frac{1}{r^2} k_\phi^2 A_r - \frac{2}{r^2} ik_\phi A_\phi - \frac{A_r}{r^2} - k_z^2 A_r \right] \end{aligned} \quad (2.9b)$$

$$\begin{aligned} -i\omega A_\phi + A_r \frac{\partial \overline{U}_\phi}{\partial r} + \frac{\overline{U}_\phi}{r} A_r + \frac{\overline{U}_\phi}{r} ik_\phi A_\phi + ik_z \overline{U}_z A_\phi + \frac{1}{\rho r} ik_\phi A_p \\ = v \left[ \frac{d^2 A_\phi}{dr^2} + 2ik_r \frac{dA_\phi}{dr} - k_r^2 A_\phi + \frac{1}{r} \left( \frac{dA_\phi}{dr} + ik_r A_\phi \right) \right] \\ + v \left[ -\frac{1}{r^2} k_\phi^2 A_\phi + \frac{2}{r^2} ik_\phi A_r - \frac{A_\phi}{r^2} - k_z^2 A_\phi \right] \end{aligned} \quad (2.9c)$$

$$\begin{aligned} -i\omega A_z + \frac{\overline{U}_\phi}{r} ik_\phi A_z + ik_z \overline{U}_z A_z + A_r \frac{d\overline{U}_z}{dr} + \frac{1}{\rho} ik_z A_z \\ = v \left[ \frac{d^2 A_z}{dr^2} + 2ik_r \frac{dA_z}{dr} - k_r^2 A_z + \frac{1}{r} \left( \frac{dA_z}{dr} + ik_r A_z \right) - \frac{1}{r^2} k_\phi^2 A_z - k_z^2 A_z \right] \end{aligned} \quad (2.9d)$$

The equation system in 2.9a-d forms an eigenvalue problem, which needs to be nondimensionalized, which is done next.

### 2.3 Nondimensionalization

In order to nondimensionalize the equations 2.9a-d, the bulk velocity in axial direction,  $U_{bulk}$ , and the pipe radius,  $r_0 = D_0/2$ , are used as characteristic flow parameters.

The dimensionless new variables can be defined as follows,

$$Y_1 = A_r^* = \frac{A_r}{U_b} \quad (2.10a)$$

$$Y_2 = A_\phi^* = \frac{A_\phi}{U_b} \quad (2.10b)$$

$$Y_3 = A_z^* = \frac{A_z}{U_b} \quad (2.10c)$$

$$Y_4 = A_p^* = \frac{2A_p}{\rho U_b^2} \quad (2.10d)$$

$$r^* = \frac{r}{r_0} \quad (2.10e)$$

$$z^* = \frac{z}{r_0} \quad (2.10f)$$

$$\phi^* = \phi \quad (2.10g)$$

$$k_r^* = k_r r_0 \quad (2.10h)$$

$$k_z^* = k_z r_0 \quad (2.10i)$$

$$k_\phi^* = k_\phi \quad (2.10j)$$

$$\omega^* = \frac{\omega r_0}{U_b} \quad (2.10k)$$

$$\overline{U_z^*} = \frac{\overline{U_z}}{U_b} \quad (2.10l)$$

$$\text{Re} = \frac{r_0 U_b}{\nu} \quad (2.10m)$$

Where  $\nu$ ,  $\rho$  and  $\text{Re}$  denote kinematic viscosity, density and Reynolds number in terms of radius, respectively. The dimensionless derivative operators can be defined accordingly.

$$\frac{d}{dr} = \frac{d}{dr^*} \frac{dr^*}{dr} = \frac{1}{r_0} \frac{d}{dr^*} \quad (2.11a)$$

$$\frac{d^2}{dr^2} = \frac{d}{dr} \left( \frac{d}{dr} \right) = \frac{d}{dr} \left( \frac{1}{r_0} \frac{d}{dr^*} \right) = \frac{1}{r_0} \frac{d}{dr^*} \left( \frac{d}{dr^*} \right) = \frac{1}{r_0} \left[ \frac{d}{dr^*} \left( \frac{d}{dr^*} \right) \frac{dr^*}{dr} \right] = \frac{1}{r_0^2} \frac{d^2}{dr^{*2}} \quad (2.11b)$$

Then, the nondimensionalized equation system becomes

$$\frac{dY_1}{dr^*} + ik_r^* Y_1 + \frac{Y_1}{r^*} + \frac{1}{r^*} ik_\phi^* Y_2 + ik_z^* Y_3 = 0 \quad (2.12a)$$

$$\begin{aligned} -i\omega^* Y_1 + \frac{\overline{U_\phi^*}}{r^*} ik_\phi^* Y_1 - 2 \frac{\overline{U_\phi^*}}{r^*} Y_2 + ik_z^* \overline{U_z^*} Y_1 + \frac{1}{2} \left( ik_r^* Y_4 + \frac{dY_4}{dr^*} \right) = \\ \frac{1}{\text{Re}} \left[ \frac{d^2 Y_1}{dr^{*2}} + 2ik_r^* \frac{dY_1}{dr^*} - k_r^{*2} Y_1 + \frac{1}{r^*} \left( \frac{dY_1}{dr^*} + ik_r^* Y_1 \right) - \frac{Y_1}{r^{*2}} k_\phi^{*2} - 2i \frac{Y_2}{r^{*2}} k_\phi^{*2} \right. \\ \left. - \frac{Y_1}{r^{*2}} - k_z^{*2} Y_1 \right] \end{aligned} \quad (2.12b)$$

$$\begin{aligned} -i\omega^* Y_2 + Y_1 \frac{d\overline{U_\phi^*}}{dr^*} + \frac{\overline{U_\phi^*}}{r^*} Y_1 + \frac{\overline{U_\phi^*}}{r^*} ik_\phi^* Y_2 + ik_z^* \overline{U_z^*} Y_2 + \frac{1}{2r^*} ik_\phi^* Y_4 = \\ \frac{1}{\text{Re}} \left[ \frac{d^2 Y_2}{dr^{*2}} + 2ik_r^* \frac{dY_2}{dr^*} - k_r^{*2} Y_2 + \frac{1}{r^*} \left( \frac{dY_2}{dr^*} + ik_r^* Y_2 \right) - \frac{Y_2}{r^{*2}} k_\phi^{*2} + 2i \frac{Y_1}{r^{*2}} k_\phi^{*2} \right. \\ \left. - \frac{Y_2}{r^{*2}} - k_z^{*2} Y_2 \right] \end{aligned} \quad (2.12c)$$

$$\begin{aligned} -i\omega^* Y_3 + ik_z^* \overline{U_z^*} Y_3 + Y_1 \frac{d\overline{U_z^*}}{dr^*} + \frac{\overline{U_\phi^*}}{r^*} ik_\phi^* Y_3 + \frac{1}{2} ik_z^* Y_4 = \\ \frac{1}{\text{Re}} \left[ \frac{d^2 Y_3}{dr^{*2}} + 2ik_r^* \frac{dY_3}{dr^*} - k_r^{*2} Y_3 + \frac{1}{r^*} \left( \frac{dY_3}{dr^*} + ik_r^* Y_3 \right) - \frac{Y_3}{r^{*2}} k_\phi^{*2} - k_z^{*2} Y_3 \right] \end{aligned} \quad (2.12d)$$

In order to build a linear first-order partial differential equation system that can be solved numerically, the second order partial derivatives in equations 2.12a-d need to be replaced with a mathematical manipulation as,

$$\frac{dY_1}{dr^*} = -ik_r^* Y_1 - \frac{Y_1}{r^*} - \frac{1}{r^*} ik_\phi^* Y_2 - ik_z^* Y_3 \quad (2.13)$$

And then taking the derivative with respect to  $r^*$ , yields

$$\frac{d^2 Y_1}{dr^{*2}} = -ik_r^* \frac{dY_1}{dr^*} + \frac{Y_1}{r^{*2}} - \frac{1}{r^*} \frac{dY_1}{dr^*} + \frac{1}{r^{*2}} ik_\phi^* Y_2 - \frac{1}{r^*} ik_\phi^* \frac{dY_2}{dr^*} - ik_z^* \frac{dY_3}{dr^*} \quad (2.14a)$$

By defining a new variable  $Y_6$ ,

$$\frac{dY_2}{dr^*} = Y_6 \quad (2.15)$$

One can have

$$\frac{d^2 Y_2}{dr^{*2}} = \frac{dY_6}{dr^*} \quad (2.16)$$

In the same way,

$$\frac{dY_3}{dr^*} = Y_7 \quad (2.17)$$

and the resulting second-order derivative becomes

$$\frac{d^2 Y_3}{dr^{*2}} = \frac{dY_7}{dr^*} \quad (2.18)$$

Substituting 2.15 and 2.17 into equation 2.14a reads,

$$\frac{d^2 Y_1}{dr^{*2}} = -ik_r^* \frac{dY_1}{dr^*} + \frac{Y_1}{r^{*2}} - \frac{1}{r^*} \frac{dY_1}{dr^*} + \frac{1}{r^{*2}} ik_\phi^* Y_2 - \frac{1}{r^*} ik_\phi^* Y_6 - ik_z^* Y_7 \quad (2.14b)$$

Rearranging the equation 2.12b and substituting 2.14b into it, yields

$$\begin{aligned} \frac{dY_4}{dr^*} = \frac{2}{\text{Re}_{r_0}} & \left[ Y_1 \left( -\frac{k_\phi^{*2}}{r^{*2}} - k_z^{*2} \right) + Y_2 \left( \frac{k_r^* k_\phi^*}{r^{*2}} - \frac{1}{r^{*2}} ik_\phi^* \right) + k_r^* k_z^* Y_3 - \frac{1}{r^*} ik_\phi^* Y_6 \right. \\ & \left. - ik_z^* Y_7 \right] \\ & + 2 \left[ Y_1 \left( iw^* - \frac{\overline{U}_\phi^*}{r} ik_\phi^* - ik_z^* \overline{U}_z^* \right) + 2 \frac{\overline{U}_\phi^*}{r^*} Y_2 - \frac{1}{2} ik_r^* Y_4 \right] \end{aligned} \quad (2.19)$$

By rearranging the equation 2.12c for the  $dY_6/dr^*$  term,

$$\frac{dY_6}{dr^*} = \text{Re}_{r_0} \left[ -iw^* Y_2 + \frac{\overline{U}_\phi^*}{r} ik_\phi^* Y_2 + ik_z^* \overline{U}_z^* Y_2 + Y_1 \frac{d\overline{U}_z^*}{dr^*} + \frac{\overline{U}_\phi^*}{r^*} Y_1 + \frac{1}{2r^*} ik_\phi^* Y_4 \right] \quad (2.20)$$

$$- \left[ 2ik_r^* \frac{dY_2}{dr^*} - k_r^{*2} Y_2 + \frac{1}{r^*} (Y_6 + ik_r^* Y_2) - \frac{k_\phi^{*2}}{r^{*2}} Y_2 + \frac{2}{r^{*2}} ik_\phi^* Y_1 - \frac{Y_2}{r^{*2}} - k_z^{*2} Y_2 \right]$$

And, by rearranging the equation 2.12d and taking out the  $dY_7/dr^*$  term,

$$\begin{aligned} \frac{dY_7}{dr^*} = \text{Re}_{r_0} & \left[ -i\omega^* Y_3 + \frac{\overline{U_\phi^*}}{r} ik_\phi^* Y_3 + ik_z^* \overline{U_z^*} Y_3 + Y_1 \frac{d\overline{U_z^*}}{dr^*} + \frac{1}{2} ik_z^* Y_4 \right] \\ & - \left[ 2ik_r^* Y_7 - k_r^{*2} Y_3 + \frac{1}{r^*} (Y_7 + ik_r^* Y_3) - \frac{k_\phi^{*2}}{r^{*2}} Y_3 - k_z^{*2} Y_3 \right] \end{aligned} \quad (2.21)$$

is obtained. Finally, 2.13, 2.15, 2.17, 2.19, 2.20 and 2.21 constitute the model equations for the dynamic perturbations in the flow field as,

$$\frac{dY_1}{dr^*} = -ik_r^* Y_1 - \frac{Y_1}{r^*} - \frac{1}{r^*} ik_\phi^* Y_2 - ik_z^* Y_3 \quad (2.22a)$$

$$\frac{dY_2}{dr^*} = Y_6 \quad (2.22b)$$

$$\frac{dY_3}{dr^*} = Y_7 \quad (2.22c)$$

$$\begin{aligned} \frac{dY_4}{dr^*} = \frac{2}{\text{Re}_{r_0}} & \left[ Y_1 \left( -\frac{k_\phi^{*2}}{r^{*2}} - k_z^{*2} \right) + Y_2 \left( \frac{k_r^* k_\phi^*}{r^{*2}} - \frac{1}{r^{*2}} ik_\phi^* \right) + k_r^* k_z^* Y_3 - \frac{1}{r^*} ik_\phi^* Y_6 \right. \\ & \left. - ik_z^* Y_7 \right] \\ & + 2 \left[ Y_1 \left( i\omega^* - \frac{\overline{U_\phi^*}}{r} ik_\phi^* - ik_z^* \overline{U_z^*} \right) + 2 \frac{\overline{U_\phi^*}}{r^*} Y_2 - \frac{1}{2} ik_r^* Y_4 \right] \end{aligned} \quad (2.22d)$$

$$\begin{aligned} \frac{dY_6}{dr^*} = \text{Re}_{r_0} & \left[ -i\omega^* Y_2 + \frac{\overline{U_\phi^*}}{r} ik_\phi^* Y_2 + ik_z^* \overline{U_z^*} Y_2 + Y_1 \frac{d\overline{U_z^*}}{dr^*} + \frac{\overline{U_\phi^*}}{r^*} Y_1 + \frac{1}{2r^*} ik_\phi^* Y_4 \right] \\ & - \left[ 2ik_r^* \frac{dY_2}{dr^*} - k_r^{*2} Y_2 + \frac{1}{r^*} (Y_6 + ik_r^* Y_2) - \frac{k_\phi^{*2}}{r^{*2}} Y_2 + \frac{2}{r^{*2}} ik_\phi^* Y_1 - \frac{Y_2}{r^{*2}} - k_z^{*2} Y_2 \right] \end{aligned} \quad (2.22e)$$

$$\begin{aligned} \frac{dY_7}{dr^*} = \text{Re}_{r_0} & \left[ -i\omega^* Y_3 + \frac{\overline{U_\phi^*}}{r} ik_\phi^* Y_3 + ik_z^* \overline{U_z^*} Y_3 + Y_1 \frac{d\overline{U_z^*}}{dr^*} + \frac{1}{2} ik_z^* Y_4 \right] \\ & - \left[ 2ik_r^* Y_7 - k_r^{*2} Y_3 + \frac{1}{r^{*2}} (Y_7 + ik_r^* Y_3) - \frac{k_\phi^{*2}}{r^{*2}} Y_3 - k_z^{*2} Y_3 \right] \end{aligned} \quad (2.22e)$$

which represent the eigenvalue problem defined by the eigenvectors  $\omega^*$ ,  $k_r^*$ ,  $k_\phi^*$  and  $k_z^*$ .

## 2.4 Mean Velocity Profile and the Boundary Conditions

The dynamic perturbation equations consist of terms with the axial and azimuthal mean velocities, which need to be defined explicitly. The normalized velocity profiles (shown in Figure 2.1) at the pipe exit ( $x/D_0 = 0$ ) of the experimental study (Örlü and Alfredsson, 2008) were used as the mean axial and azimuthal velocities ( $\overline{U_z}$  and  $\overline{U_\phi^*}$ ) in the present simulations. The data correspond to a bulk dimensional axial velocity of  $U_{bulk} = 6$  m/s and to a Reynolds number of  $\text{Re} = 24000$ . When necessary, a cubic interpolation (Press et al, 1992) was used in between the measured points.

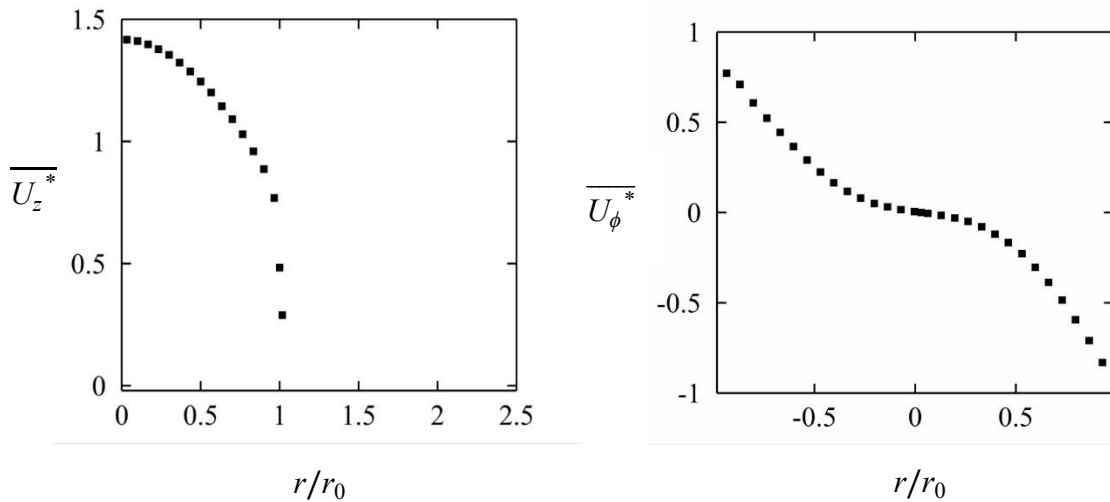


**Figure 2.1** : Normalized jet exit velocity profiles at  $z/D_0 = 0.0$  a) Axial b) Azimuthal (Örlü and Alfredsson, 2008).

The swirl number is formulized by,

$$S = \frac{\int_0^R \rho u w r^2 dr}{R \int_0^R \rho u^2 r dr} \quad (2.23)$$

Which is the ratio of axial flux of angular momentum and the axial momentum, times the equivalent pipe radius (Gupta et al., 1984). The swirling jet of mentioned experiments, therefore, has a swirling number of the  $S = 0.5$  (Örlü and Alfredsson, 2008).

The impermeable and no-slip boundary condition is imposed for velocity fluctuation components at the wall, that is,

$$Y_1(r^*, z^*, t) = 0 \quad (2.24a)$$

$$Y_2(r^*, z^*, t) = 0 \quad (2.24b)$$

$$Y_3(r^*, z^*, t) = 0 \quad (2.24c)$$

However, due to the coordinate singularity at the centerline ( $r^* = 0$ ), certain regularity and analytical constraints are required for the solution of the equation system to remain bounded (Meseguer and Trefethen, 2000). According to Batchelor and Gill (1962) and Faisst (2003), for non-helical ( $k_\phi = 0$ ) perturbations these constraints are,

$$Y_1(0, z^*, t) = 0 \quad (2.25a)$$

$$\frac{d^2 Y_1}{dr^{*2}}(0, z^*, t) = 0 \quad (2.25b)$$

$$Y_2(0, z^*, t) = 0 \quad (2.25c)$$

and for helical perturbation, i.e.,  $k_\phi = 1$ , constraints are,

$$Y_3(0, z^*, t) = 0 \quad (2.25d)$$

$$Y_1(0, z^*, t) = -iY_2(0, z^*, t) \quad (2.25e)$$

$$Y_4(0, z^*, t) = 0 \quad (2.25f)$$

Additionally, due to the radial symmetry,

$$\overline{\frac{dU_z}{dr^*}}(0, z^*, t) = 0 \quad (2.25g)$$

It is known that in fully turbulent wall-bounded shear flows, the viscous shear stresses are very small compared to the turbulent stresses particularly in the outer region of

the boundary layer and can be neglected (Toonder & Nieuwstadt 1997; Wu & Moin, 2008). Based on this, it can be said that viscous terms at the right-hand side (RHS) of the equations 2.12b-d can be neglected near centerline region, which also agrees with the fact these terms are divided by the Reynolds number and happen to be roughly 5 orders of magnitude smaller than the rest. The Polar coordinate singularity at the centerline ( $r^* = 0$ ) is treated by the strategy developed by Mohseni and Colonius (2000), where the first discretization point is staggered by  $\Delta r/2$ ; In our study we locate the grid point further close to the pole by shifting the radial coordinate by  $0.15 \times \Delta r/2$ . This method is widely used in previous studies regarding cylindrical coordinate singularities due to its simplicity and accurate results. (Bogey, Marsden, & Bailly, 2011; Skene and Schmid, 2019).

## 2.5 Numerical Solution Process

The first order ordinary differential equations 2.22a-e represent the eigenvalue problem defined by the eigenvectors  $\omega^*$ ,  $k_r^*$ ,  $k_\phi^*$  and  $k_z^*$ . In order to solve the problem, given the values of  $\omega^*$ ,  $k_r^*$  and  $k_\phi^*$  the corresponding values of  $k_z^*$  and eigenfunctions (shape functions) will be sought (Özdemir, 1991). In order to reduce the eigenvalue problem into a boundary value problem, a new variable is defined (Özdemir, 1991).

$$Y_5 = k_z^* \quad (2.26)$$

Since the eigenvalue  $k_z^*$  is constant throughout the solution space,

$$\frac{dY_5}{dr^*} = 0 \quad (2.27)$$

The new system extended by adding 2.27 to the equation set necessitates one more boundary condition to make the system closed. The orthonormalization condition of eigenfunctions is used for this purpose,

$$\int_0^{r_0^*} Y^T(r^*) Y(r^*) dr^* = C \quad (2.28)$$

where the constant  $C$  might arbitrarily have any value. Furthermore, by using 2.28, another new variable is defined as (Keller, 1976),

$$Y_8(r^*) = \int_0^{r_0^*} Y^T(r^*) Y(r^*) dr^* \quad (2.29)$$

$$\frac{dY_8}{dr^*} = Y^T(r^*) Y(r^*) \quad (2.30)$$

Or it can be explicitly expressed as

$$\frac{dY_8}{dr^*} = Y_1^2 + Y_2^2 + Y_3^2 + Y_4^2 + Y_5^2 + Y_6^2 + Y_7^2 \quad (2.31)$$

The equation 2.29 brings two new boundary conditions and transforms the system into a closed-form and can be expressed as,

$$Y_8(0) = 0 \quad (2.32a)$$

$$Y_8(1) = C \quad (2.32b)$$

In the present work,  $C$  value is defined according to the prescribed value of the turbulent intensity at the pipe exit, which will be described in section 5.3.

## 2.6 Parallel Shooting Method

The boundary value problem described by the equations 2.22a-e and the boundary conditions 2.24a-c, 2.25a-g and 2.32a-b can be solved like an initial value problem using the shooting method. In that, the missing boundary values at both inner ( $r=0$ ) and outer ( $r=r_0$ ) boundaries are specified freely so that the system can be integrated from one to the other boundary (Press et al, 1992). The freely specified values are corrected iteratively by using the multidimensional Newton-Raphson method until the integration fulfills the actual conditions at the opposite boundary. However, using the standard shooting method in wide domains leads to undesired numerical errors (Olendraru et al., 1999; Wang et al., 2016). To prevent such errors, the domain is split into two parts, in which the integration is performed from each boundary to an arbitrary fitting point near the middle, where the solutions from both sides are desired to be close as possible within a very small margin of error. This approach is called parallel shooting method and it is faster and more reliable compared to the standard shooting method.

Due to the complex eigenfunctions, the equation system requires 16 real conditions at two boundaries. Eight of these boundary conditions are prescribed by the flow

dynamics and numerical procedure, while the rest of them should be guessed initially. In this regard, a vector  $V$  with the components of initially guessed values is formed so that all the necessary boundary conditions of the system are specified. As the integration proceeds from inner and outer boundaries to the fitting point with fourth order Runge-Kutta method, the solutions are checked after each integration step with a discrepancy vector  $E$ ,

$$E_i = |Y_i(y^*; V_1, \dots, V_n) - Y_i(y^*; V_{n+1}, \dots, V_8)|, \quad 1 \leq i \leq 8 \quad (2.33)$$

At this point, the purpose is to find a vector value of  $V$  for that the vector value of  $E$  is zero (Press et al, 1992). Using the multidimensional Newton-Raphson method, the equation set is solved,

$$J_{(8 \times 8)} \cdot \delta V = -E \quad (2.34)$$

and the correction vector  $\delta V$  from 2.34 is added back to  $V$  to generate a new prediction vector,

$$V_{\text{new}} = V_{\text{old}} + \delta V \quad (2.35)$$

The Jacobien matrix in 2.34 has the components given by the evaluation

$$J_{ij} = \frac{\partial E_i}{\partial V_j} \approx \frac{E_i(V_1, \dots, V_j + \Delta V_j, \dots) - E_i(V_1, \dots, V_j, \dots)}{\Delta V_j} \quad (2.36)$$

The iterations in this study were repeated until the discrepancy vector  $E$  reaches a margin of  $10^{-14}$ , while the calculations were done on a 64-bit processor with all numerical values defined in double-precision format.

### 3. RESULTS OF HYDRODYNAMIC STABILITY ANALYSIS

The numerical solution method described in the previous chapter was used for the calculations in a circular pipe flow. The calculations were made at the exit of a pipe of length  $2r_0$ , which corresponded to a wave growth over a  $z$  distance of  $2r_0$ . The computational domain defined for the stability analysis is shown in Figure 3.1, which was discretized in the radial direction at 201 computation points.

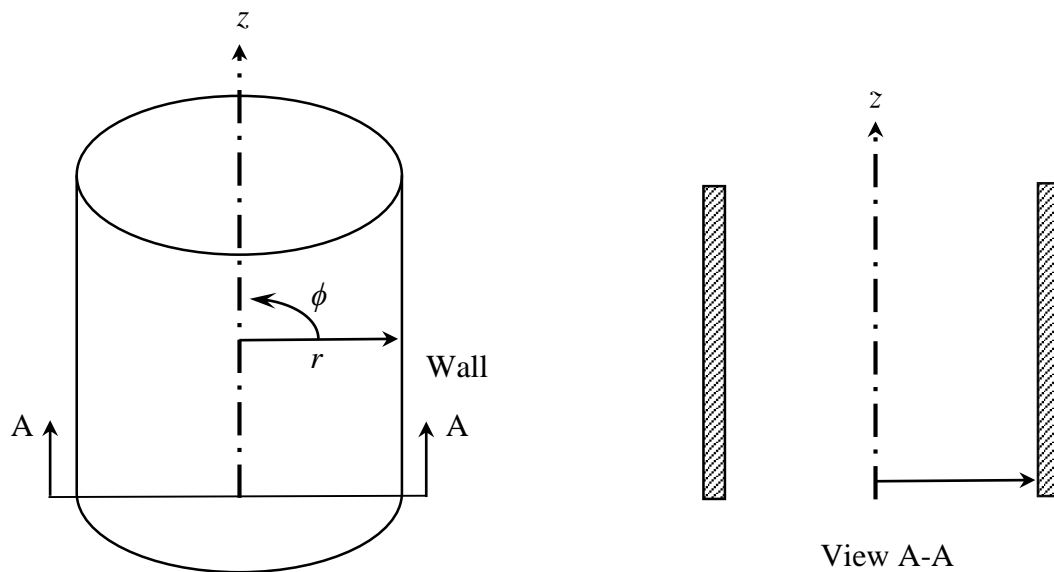


**Figure 3.1 :** Computational domain for mode calculation.

The initial guess values at the start of the computation are given in Table 3.1.

**Table 3.1** : Initial guess values at boundaries.

Boundary	Variable	$V$	$\Delta V$
Wall	Re( $Y_6$ )	$-4.606728474739236 \cdot 10^{-1}$	$4.606728543384840 \cdot 10^{-2}$
	Im( $Y_6$ )	$-1.533805845315795 \cdot 10^{-2}$	$1.533805868171283 \cdot 10^{-3}$
	Re( $Y_7$ )	$-1.944235913640080 \cdot 10^{-8}$	$1.944235942611453 \cdot 10^{-9}$
	Im( $Y_7$ )	$4.0895872302174190 \cdot 10^{-9}$	$4.089587291157017 \cdot 10^{-10}$
	Re( $Y_4$ )	$2.336262838489050 \cdot 10^{-7}$	$2.336262873302079 \cdot 10^{-8}$
	Im( $Y_4$ )	$-5.717627379947398 \cdot 10^{-9}$	$5.717627465146685 \cdot 10^{-10}$
	Re( $Y_5$ )	$2.565199944935720 \cdot 10^{-3}$	$2.565199887599033 \cdot 10^{-5}$
	Im( $Y_5$ )	$7.738414932520961 \cdot 10^{-2}$	$7.738414759553908 \cdot 10^{-4}$
Centerline	Re( $Y_1$ )	$2.971826961290401 \cdot 10^{-4}$	$2.971827005574073 \cdot 10^{-5}$
	Im( $Y_1$ )	$-4.075944535036068 \cdot 10^{-5}$	$4.075944595772375 \cdot 10^{-6}$
	Re( $Y_2$ )	$6.988301031184836 \cdot 10^{-4}$	$6.988301135318636 \cdot 10^{-5}$
	Im( $Y_2$ )	$-2.483215984593990 \cdot 10^{-6}$	$2.483216021596792 \cdot 10^{-7}$
	Re( $Y_3$ )	$-1.987592540730970 \cdot 10^{-6}$	$1.987592570348407 \cdot 10^{-7}$
	Im( $Y_3$ )	$1.845545041503233 \cdot 10^{-7}$	$1.845545069003997 \cdot 10^{-8}$
	Re( $Y_5$ )	$2.565199944935720 \cdot 10^{-3}$	$2.565199887599033 \cdot 10^{-5}$
	Im( $Y_5$ )	$7.738414932520961 \cdot 10^{-2}$	$7.738414759553908 \cdot 10^{-4}$

The variations of  $k_{zr}^*$  with normalized frequency ( $\omega^*$ ) are illustrated in Figure 3.2 for axisymmetric and non-axisymmetric perturbations. It appears that  $k_{zr}$  remains positive and exhibits a linear behavior with approximately constant slope for all values of  $k_r$ . The axial wavenumber  $k_{zr}^*$  of disturbances remains almost independent of the  $k_r$  values. Thus, for clarity, the graphs are shown for the radial wavenumber of  $k_r = 0$ . we can define a phase velocity,  $v_{phase}$ , for the modes travelling downstream as (Wu et al., 1992)

$$v_{phase} = \frac{\omega}{k_{zr}} \quad (3.1)$$

which takes a value of  $v_{phase} = 0.85$  m/s for  $k_\phi = 0$  and 1.14 m/s for  $k_\phi = 1$ . These phase velocities are in agreement with the studies for both temporally (Lessen et al., 1974) and spatially (Garg and Rouleau, 1972; Lessen and Singh, 1973; Abid et al., 1993) evolving waves.

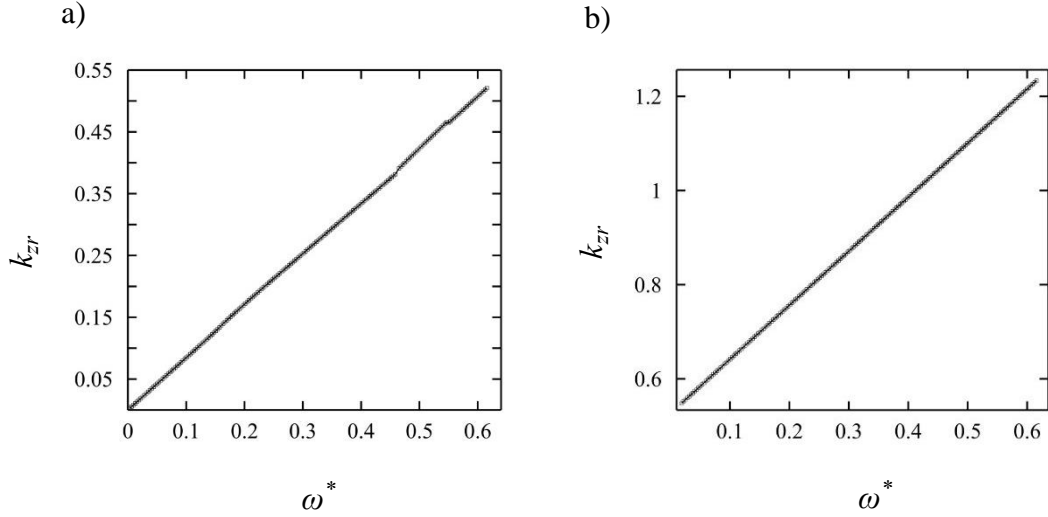
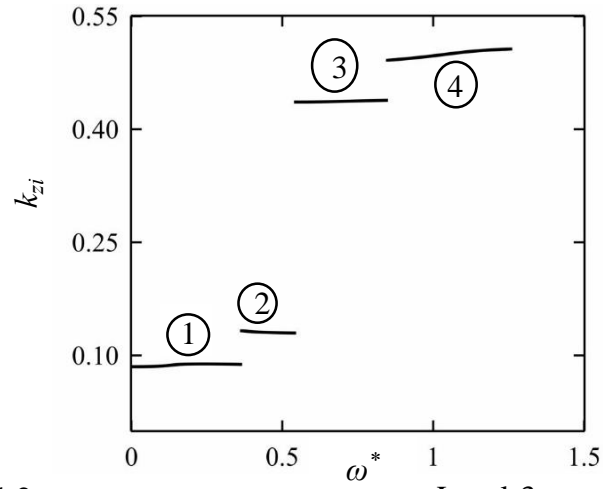
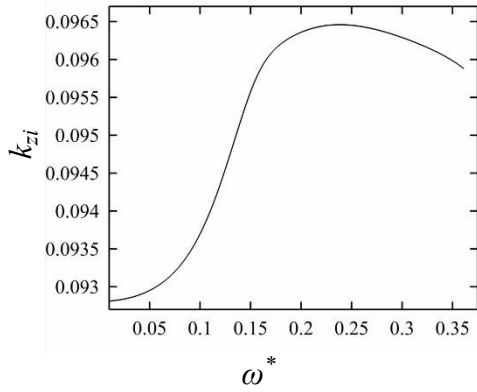


**Figure 3.2 :** Variation of real part of normalized wavenumber  $k_{zr}^*$  with normalized frequency  $\omega^*$ , a)  $k_\phi = 0$ , b)  $k_\phi = 1$

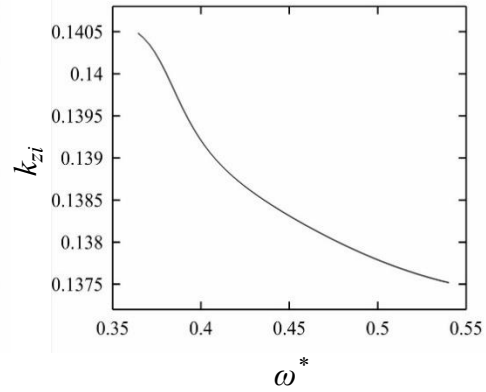
The imaginary part,  $k_{zi}$ , for  $k_\phi = 0$  is presented in Figure 3.3, where it remains always positive over the entire spectrum, which indicates a negative growth rate expressed as  $e^{-k_{zi}}$ . Since all Fourier modes decay downstream in the flow, the pipe flow can be said to be spatially stable with respect to the axisymmetric ( $k_\phi = 0$ ) disturbances. Reminding the current swirl ratio,  $S = 0.5$ , these results are actually in agreement with the findings of Howard and Gupta (Howard and Gupta, 1962) and Leibovich (Leibovich, 1984), who showed that swirling pipe flows are stable for swirl ratios higher than the critical value of 0.403. Indeed, it is known that the swirling pipe flows are generally stable to axisymmetric perturbations in a wide range of Reynolds numbers and swirl ratios. Furthermore, the temporal (Pedley, 1969; Lessen and Singh, 1973) and spatial (Garg and Rouleau, 1972; Fernandez-Feria and del Pino, 2002) stability studies both conclude that such flows are generally stable to axisymmetric ( $k_\phi = 0$ ) perturbations. In Figure 3.3, one should also point out that the  $k_{zi}$  values have different discrete levels (rising from 1 to 4), in each of which changes occur in a continuous manner. The  $k_{zi}$  values in level 1 first increases from 0.0452 to 0.0965 in the range  $0 < \omega < 0.22$  and, then, decreases to a value of 0.0958 towards  $\omega = 0.35$ . Afterwards, it jumps to 0.1405 in level 2, where the rate of wave attenuation decreases continuously to 0.1375. The second jump occurs to 0.444 in level 3, where the decay exponent continuously increases to 0.4463. Finally, the third jump takes the decay rate from 0.495 to 0.514.



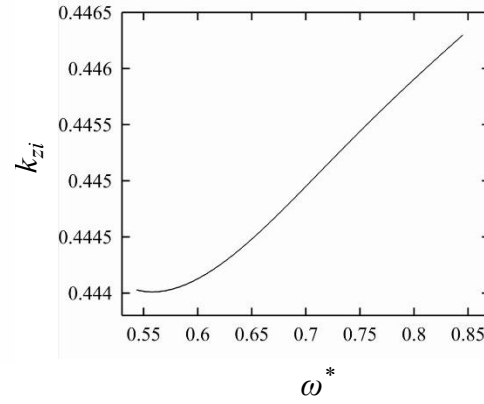
Level-1



Level-2



Level-3



Level-4

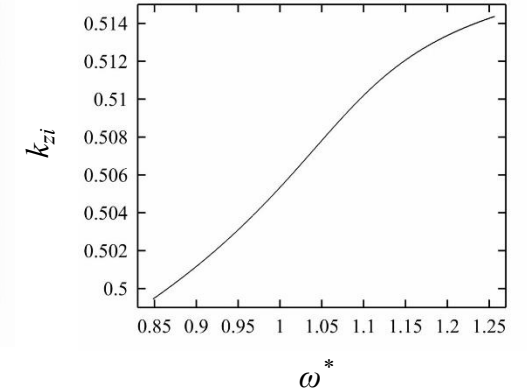


**Figure 3.3 :** Variation of the decay rate  $k_{zi}$  with normalized frequency  $\omega^*$  for  $k_\phi = 0$ .

The rates of change of modes for the case  $k_\phi = 1$  are presented in Figure 3.4. Here again, all modes decay and the pipe flow seems to be spatially stable in response to the non-axisymmetric ( $k_\phi = 1$ ) disturbances. This is in agreement with the studies on temporal modes in the range of high Reynolds numbers (Lessen et al., 1968; Vanderborck and Platten, 1978) (including the Re of the current flow) and on the spatial instability of turbulent pipe flows (Garg and Rouleau, 1972), where no instability was found in non-axisymmetric perturbation of  $k_\phi = 1$ . In addition, the investigation of the vortex instabilities and the onset of breakdown leads to a new definition of instability based on critical swirl threshold, which was first proposed by Wang and Rusak (Wang and Rusak, 1996) for solid body rotations in pipe flows. The extension of their work on non-axisymmetric perturbations (Wang et al., 2016) shows that the flow remains asymptotically stable when its swirl ratio is less than the critical value of 1.613, which perfectly concurs with the findings of the present work, where the swirl level was less than this critical value. Furthermore, the experimental results of Örlü & Alfredsson (Örlü and Alfredsson, 2008) indicate that there is no vortex breakdown phenomenon undergoing in their benchmark pipe flows, which substantiates the results of our stability analyses. Fig. 5 also shows that three different discrete levels in the form of a backward step are observed in contrary to the case  $k_\phi = 0$ . The detailed changes in each of these sections are provided in subfigures Level 1 to Level 3: In the first level, the decay rate changes in a parabolic manner. In the two subsequent levels, it first increases with a curve concaving up between  $0.7 < \omega < 1.4$  and, then, with a curve concaving down between  $1.4 < \omega < 1.9$ .

The mode shapes corresponding to the eigenspectra discussed previously are presented in Figure 3.5 for radial wavenumber  $k_r = 0$  and in Figure 3.6 for  $k_r = 1$ . It is clear in all sub-graphs in Figure 3.5 that the amplitude of the eigen (shape) function modulations increases with the frequency. The envelope function of the amplitude modulations, which gives us an idea about the spatial distributions of the relevant rms fluctuations, behaves more like a skewed Gaussian distribution with a tail extending towards the centerline. It makes a peak at around  $r/r_0 = 0.58$  and it is interesting that this point is not close to the centerline but on the wall side of the flow passage, in a region typically described as the outer region of a turbulent boundary layer. Almost exactly the same behavior is observed for  $k_r = 1$  (Figure 3.6) except for the location of the envelope peak, which is shifted towards the wall and occurs  $r/r_0 = 0.62$ .

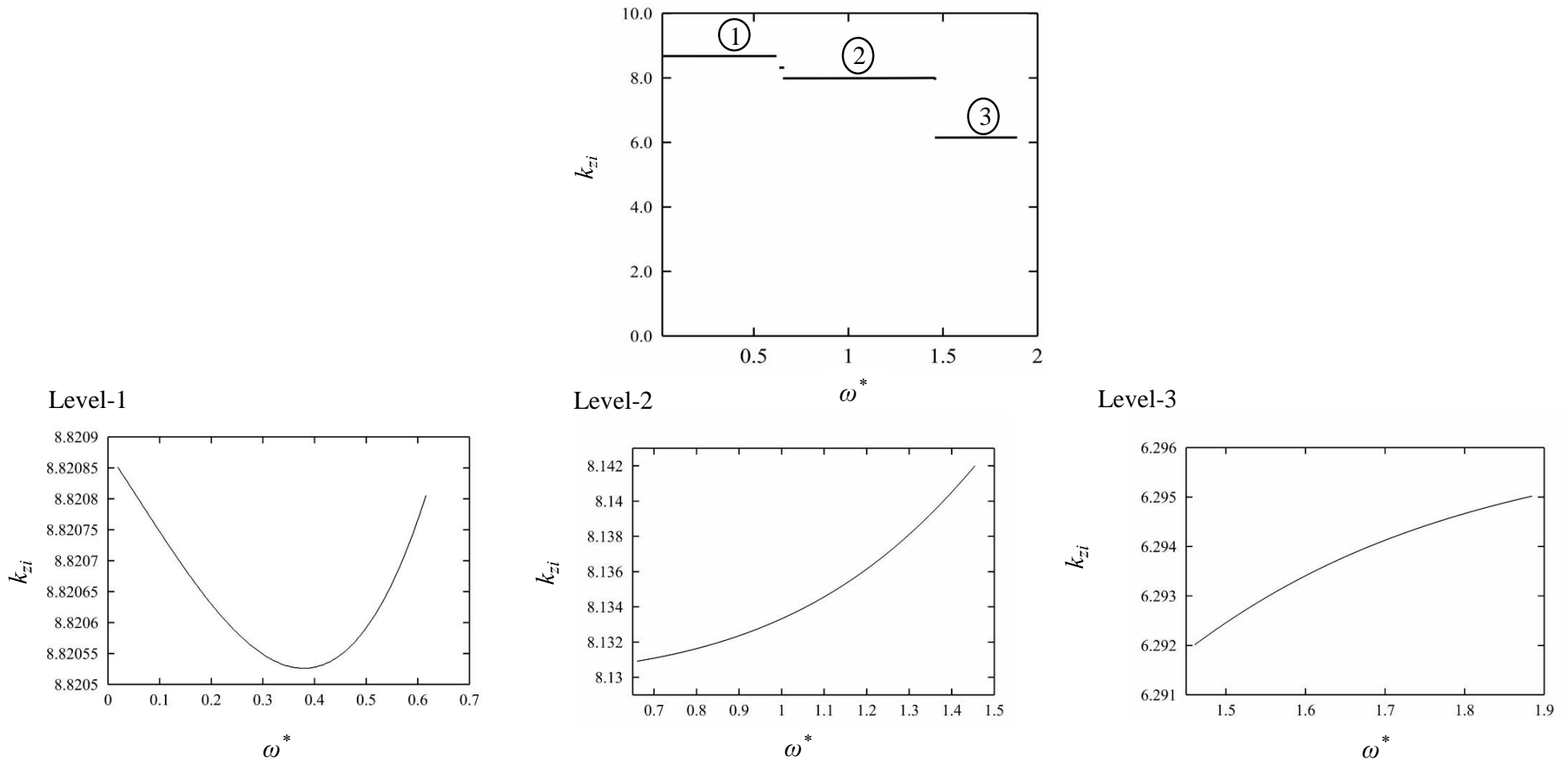


**Figure 3.4 :** Variation of the decay rate  $k_{zi}$  with normalized frequency  $\omega^*$  for  $k_\phi = 1$ .

It should also be noted that in both Figure 3.5 and Figure 3.6, the order of magnitude of amplitudes seems very different for different model shapes,  $u'_r$ ,  $u'_\phi$  and  $u'_z$ , in that  $u'_\phi$  and  $u'_z$  are at the same order of magnitude whereas  $u'_r$  is 2 orders of magnitude smaller. Figure 3.7 shows that unlike the mode shapes for  $u'_r$  and  $u'_\phi$ , the mode shapes for  $u'_z$  are not zero at the centerline  $r/r_0 = 0$ . This is a manifestation of the boundary conditions imposed  $u'_z$ , where it is bounded on the wall and is free at the centerline (Garg and Rouleau, 1972; Faisst, 2003). However, as the frequency increases, the nonzero values at  $r/r_0 = 0$  decreases substantially. From the previous studies on turbulent rotating pipe flows such as the experimental investigation of pipe flows conducted by Imao et al. (1996) and lately, DNS of pipe flows reported in Wu and Moin (2008), The Reynolds and viscous shear stresses have both peak values near the wall where Reynolds stress goes to zero in the vicinity of the wall while viscous shear stress gets the highest value. These results support the previous radial distribution of turbulent intensities graphs (Figure 3.7) from the linear instability analysis, where it is not taking into account the Reynolds stresses which results in the shifted peaks toward the centerline of the pipe.

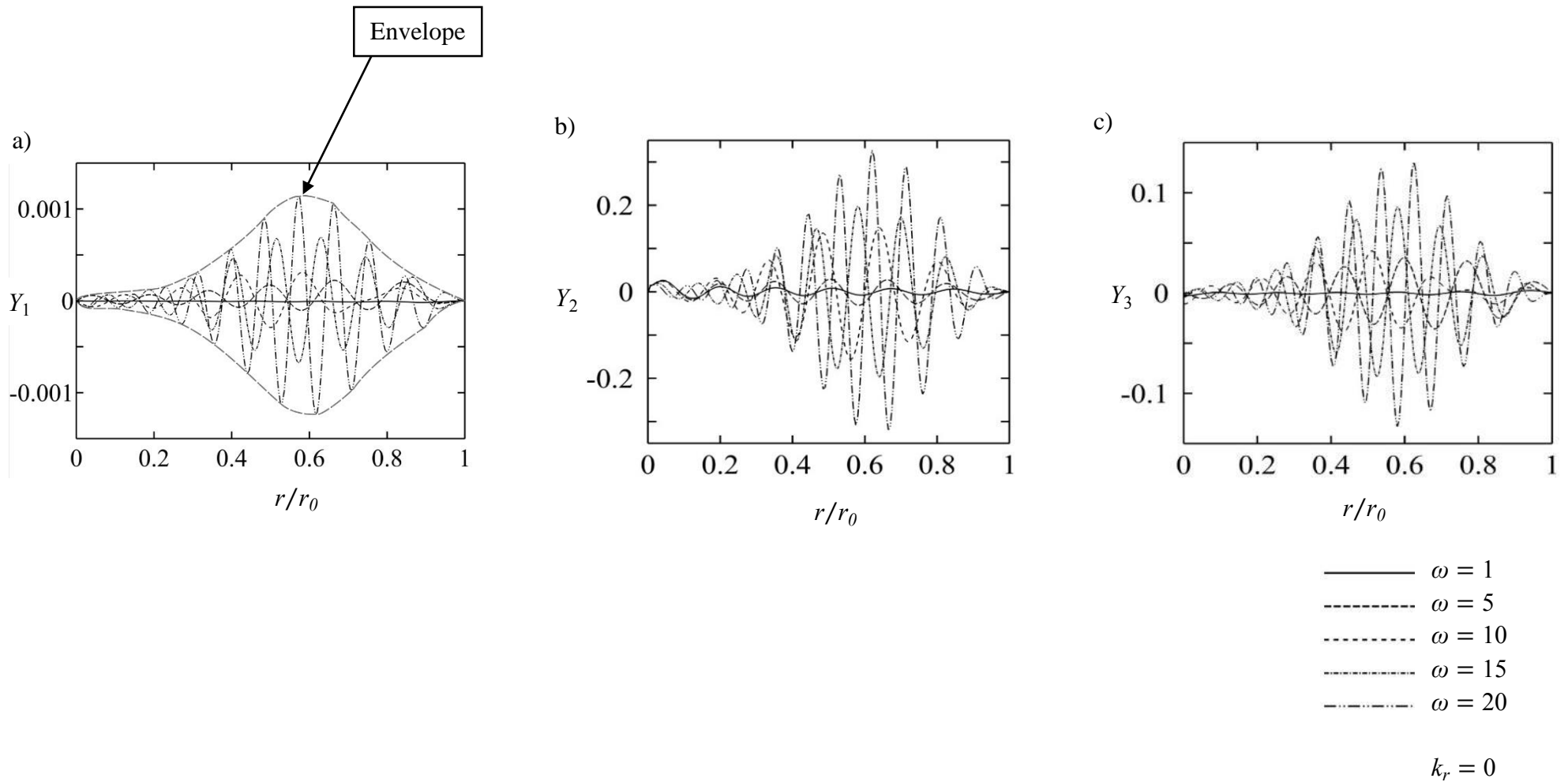


**Figure 3.5 :** Mode shapes for  $k_r = 0$  at different frequencies, Left, radial component,  $Y_1 = u'_r$ . Center, tangential component  $Y_2 = u'_\phi$ . Right, axial component  $Y_3 = u'_z$ .

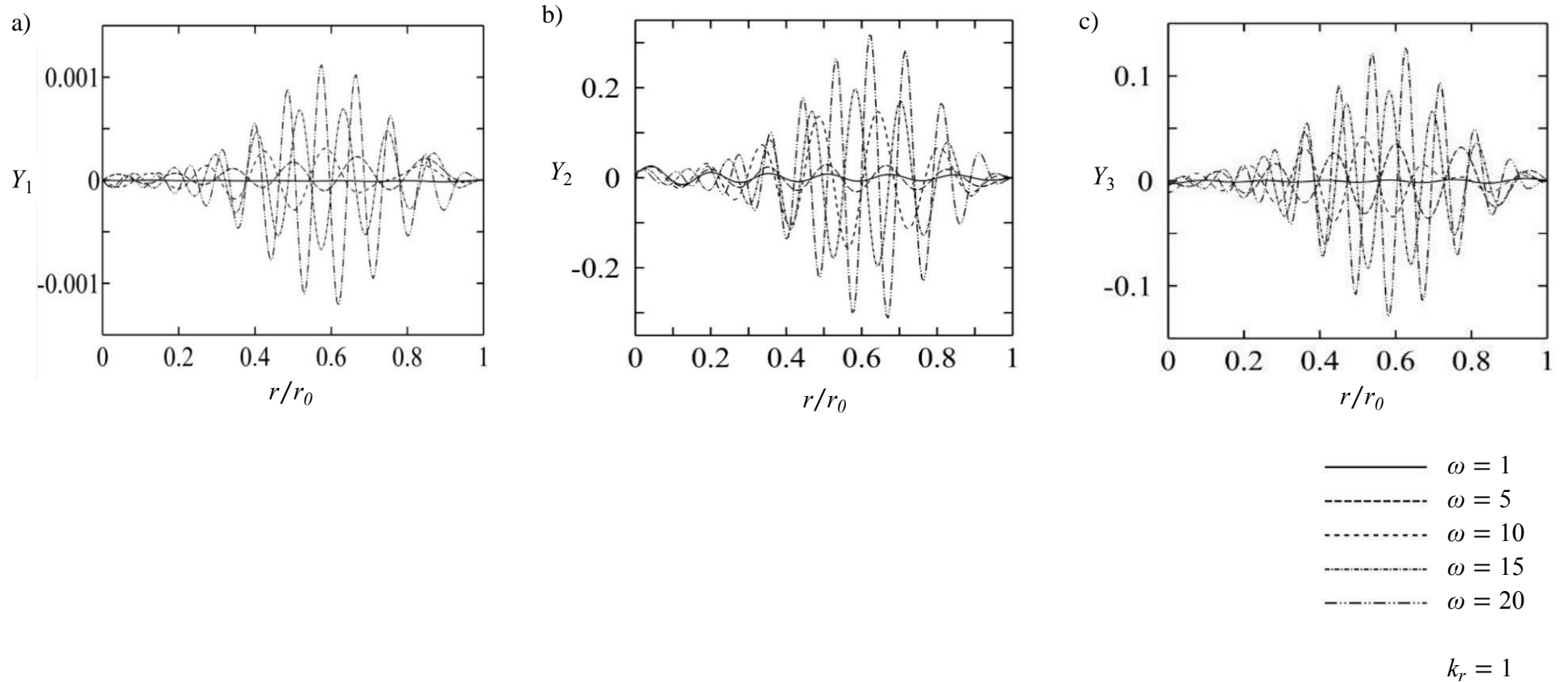


**Figure 3.6 :** Mode shapes for  $k_r = 1$  at different frequencies, Left, radial component,  $Y_1 = u'_r$ . Center, tangential component  $Y_2 = u'_\phi$ . Right, axial component  $Y_3 = u'_z$ .

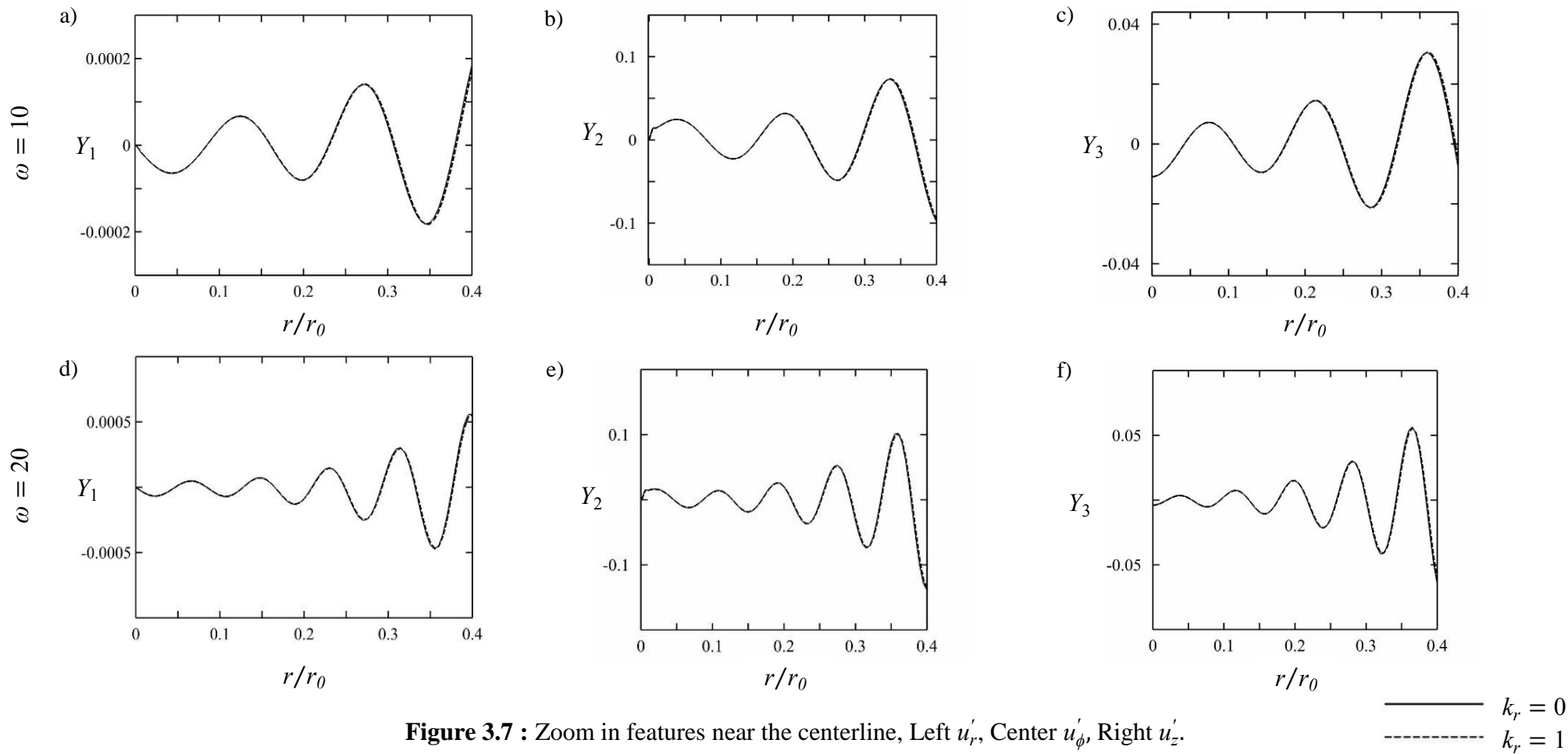
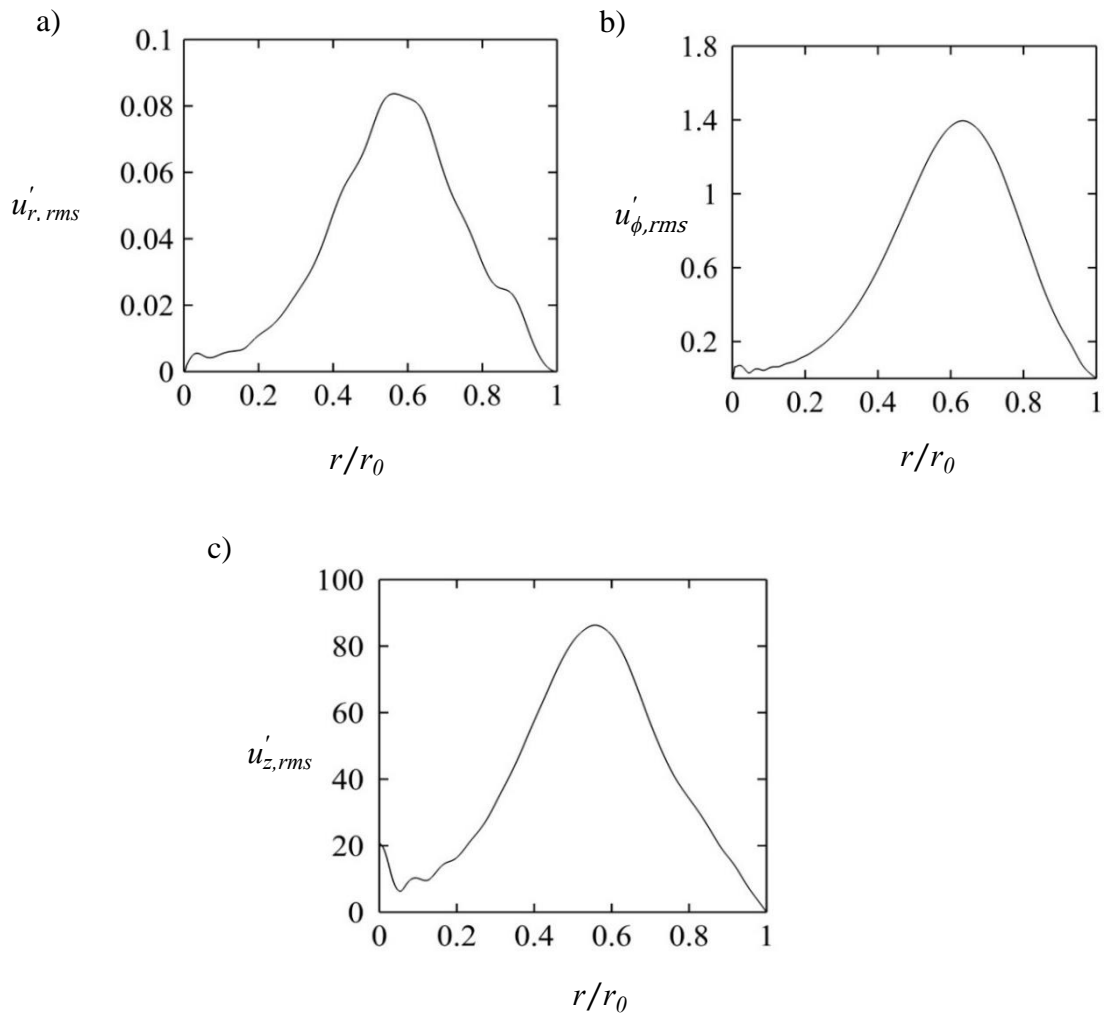


Figure 3.8 presents the rms fluctuation profiles of  $u'_r$ ,  $u'_\phi$  and  $u'_z$  which were calculated from the modal shapes. The rms profiles of the radial ( $u'_r$ ) and axial velocity fluctuations ( $u'_z$ ) exhibit a peak value at around  $r/r_0 = 0.58$ , whereas the helical velocity fluctuation rms ( $u'_\phi$ ) reaches its maximum roughly at  $r/r_0 = 0.65$ . Furthermore, it should be emphasized that as it is expected, the fluctuation velocities all drop to zero at the wall. At the centerline, however, the rms fluctuations diminish except for the axial fluctuation values. It seems that highest fluctuation intensity occurs for the axial fluctuation component, which decreases subsequently almost 2 orders of magnitude for the helical fluctuation component and finally 1 order of magnitude more reduction is observed for the radial component. These results indicate a strong anisotropy in the turbulent field. Hence, it is evident that the radial and helical fluctuations do not have any significant contribution to the turbulent energy. These findings confirm the outcomes of the previous studies on turbulent rotating pipe flows (Imao et al., 1996; Wu and Moin, 2008). The radial RMS distributions of the velocity components show that the axial fluctuations are dominant. Whereas, the azimuthal fluctuation is approximately two orders of magnitude less than  $u'_{z,rms}$  and the  $u'_{r,rms}$  does not have any significant contribution to the fluctuation energy of the flow.



**Figure 3.8 :** Radial distribution of RMS profiles, a)  $u'_{r,rms}$ , b)  $u'_{\phi,rms}$ , c)  $u'_{z,rms}$ .

## **4. LARGE EDDY SIMULATION OF AN INCOMPRESSIBLE, AXISYMMETRIC, TURBULENT SWIRLING JET**

In this chapter three commonly used numerical methods for turbulence modeling in CFD is briefly discussed. These different approaches, DNS, RANS and LES are compared so to justify the use of LES.

### **4.1 Turbulence Simulation: DNS**

As being the most accurate approach in simulating turbulent flow DNS resolves all length and time scales of the flow domain by solving Navier-Stokes equations and no modeling is involved (Jimenez, 2003). However, highly accurate discretization methods are required for DNS to accurately capture the evolution of turbulence over a wide range of length and time scales from Kolmogorov microscales up to the integral scales. Hence, the number of grid points required increases as  $Re^{9/4}$  (Pope, 2000). Hence, DNS is only limited to the simulation of the flows at relatively low Reynolds number and simple geometries (Xie, 2016).

### **4.2 Turbulence Simulation: RANS**

In contrast to DNS approach, the RANS models the whole cascade in a similar manner, assuming, for example, the isotropy is valid at all scales is important characteristics of this technic and, thus, it reduces computational cost and memory requirements, which makes it the most popular approach in industrial CFD applications. On the other hand, the RANS method is unable to capture the complex turbulent flow characteristics such as recirculation, coherent structures in turbulent swirling flows and in general does not provide any information about unsteady features of turbulent flows.

### **4.3 Turbulence Simulation: LES**

One of the most successful model which is a compromise between the first two methodologies for turbulence modeling is LES which was first introduced by

Smagorinsky for meteorology applications in 1963 (Smagorinsky, 1963). In LES large scales are anisotropic and, thus, resolved explicitly while small eddies can be considered to be much less dependent on the flow geometry and are close to isotropic, more universal and homogeneous in character than the large eddies and modelled by a sub-grid scale (SGS) model. Thus, LES reduces the computational cost related to mesh fineness significantly compared to DNS (Fröhlich and Rodi, 2001). It also remains more universal and produce more accurate results compared to the RANS since the large eddies contain most of the turbulent energy and responsible for momentum transfer is captured by the LES while they are modelled in the RANS approach (Fröhlich and Terzi, 2008). Hence, LES has proven to be one of the most feasible and promising methods to overcome the limitations of the DNS and RANS which is widely used in recent decades to predict complex turbulent flows as shown in figure 4.1 (Heinz, 2020).

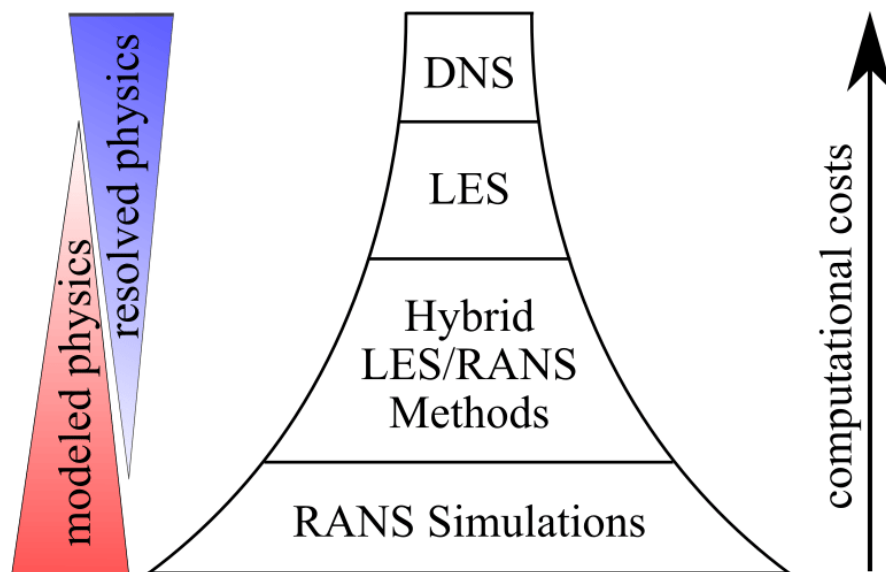


**Figure 4.1 :** A schematic differentiation between RANS, LES and DNS modeling. (Sagaut et al, 2013).

### 4.3.1 Filtering in LES

As mentioned in the previous section, LES formulation requires the modelling the effects of unresolved SGS and resolving the large eddies in a flow field. In order to filter out the smaller eddies, first, a separation of the spectra of flow variables in respect of the wave number is required. A flow variable  $\theta$  is decomposed into two parts as follows,

$$\theta(x) = \bar{\theta}(x) + \theta''(x) \quad (4.1)$$

where  $\bar{\theta}$  denotes the contribution due to the resolved scales with lower wave numbers and  $\theta''$  denotes the contribution due to the subgrid scales with higher wave numbers. Then, a filtered flow variable in a certain fluid domain  $D$  can be defined by,

$$\tilde{\theta}(x) = \int_D \theta(x'') G(x, x'') dx'' \quad (4.2)$$

so that the equation 4.2 represents the convolution of the flow variable  $\theta$  with the filtering kernel function  $G$ .

It is worth noting that the filtering operator differs from Reynolds operators by two crucial distinctions (Sagaut, 2002). The first distinction is that a time averaging of a filtered flow variable is not equal to the time-average of the variable itself.

$$\overline{\tilde{\theta}}(x) = \int_D \tilde{\theta}(x'') G(x, x'') dx'' \neq \bar{\theta}(x) \quad (4.3)$$

By rewriting the equation (4.1), the subgrid part of the flow variable can be defined as

$$\theta''(x) = \theta(x) - \bar{\theta}(x) \quad (4.4)$$

By time-averaging the equation 4.4, it yields

$$\overline{\theta''}(x) = \bar{\theta}(x) - \overline{\tilde{\theta}}(x) \quad (4.5)$$

Since  $\bar{\theta}(x)$  and  $\overline{\tilde{\theta}}(x)$  in equation 4.5 are not equal, as obtained in 4.3, time average of the subgrid part does not yield zero.

$$\overline{\theta''}(x) \neq 0 \quad (4.6)$$

Although there are various types of filter functions  $G$ , the most common are called the box (or top-hat) filter, the Gaussian filter and the sharp cutoff filter.

### 4.3.2 Formulation of equations

By employing a top-hat filter to the unsteady incompressible Navier-Stokes equations, the following continuity and momentum equations is obtained.

$$\frac{\partial \tilde{u}_i}{\partial x_i} = 0 \quad (4.7)$$

$$\frac{\partial \tilde{u}_i}{\partial t} + \frac{\partial(\tilde{u}_i \tilde{u}_j)}{\partial x_j} = -\frac{\partial \tilde{p}}{\partial x_i} + \frac{1}{\text{Re}} \frac{\partial^2 \tilde{u}_i}{\partial x_j \partial x_j} \quad (4.8)$$

Due to the non-linear term  $(\tilde{u}_i \tilde{u}_j)$  on the LHS of equation 4.8, a decomposition in terms of the resolved and sub-grid parts of  $u_i$  is required.

### 4.3.3 Leonard decomposition

$$u = \tilde{u}_i + u_i'' \quad (4.9)$$

$$\tilde{u}_i \tilde{u}_j = (\tilde{u}_i + \widetilde{u_i''})(\tilde{u}_j + u_j'') \quad (4.10)$$

$$\tilde{u}_i \tilde{u}_j = \tilde{u}_i \tilde{u}_j + \widetilde{u_i'' u_j''} + \widetilde{u_i'' u_j''} + u_i'' u_j'' \quad (4.11)$$

Subtracting a  $\tilde{u}_i \tilde{u}_j$  term from both sides of equation 4.11, yields

$$\widetilde{u_i'' u_j''} - \tilde{u}_i \tilde{u}_j = \widetilde{u_i'' u_j''} - \tilde{u}_i \tilde{u}_j + \widetilde{u_i'' u_j''} + u_i'' u_j'' \equiv \tau_{ij} \quad (4.12)$$

Then, by substituting 4.12 into the equation 4.8,

$$\frac{\partial \tilde{u}_i}{\partial t} + \frac{\partial(\tilde{u}_i \tilde{u}_j)}{\partial x_j} = -\frac{\partial \tilde{p}}{\partial x_i} - \frac{\partial \tau_{ij}}{\partial x_j} + \frac{1}{\text{Re}} \frac{\partial^2 \tilde{u}_i}{\partial x_j \partial x_j} \quad (4.13)$$

is obtained, where  $\tilde{p}$  and  $\tau_{ij}$  denote the filtered pressure and SGS stress tensor, respectively.

The SGS stress tensor  $\tau_{ij}$  can be further separated into three stress tensors by using Leonard decomposition.

$$\tau_{ij} = L_{ij} + C_{ij} + R_{ij} \quad (4.14)$$

$$L_{ij} = \widetilde{\widetilde{u}_i \widetilde{u}_j} - \widetilde{u}_i \widetilde{u}_j \quad (4.15)$$

$$C_{ij} = \widetilde{\widetilde{u}_i \widetilde{u}_j''} + \widetilde{u}_i \widetilde{u}_j'' \quad (4.16)$$

$$R_{ij} = \widetilde{u_i u_j''} \quad (4.17)$$

The term  $L_{ij}$  denotes Leonard stress tensor, which describe the interactions between all resolved scales of the flow.  $C_{ij}$  is called cross-stress tensor and it is related to interactions between large and small scales. Finally,  $R_{ij}$  denotes the Reynolds stress tensor and it determines the effect of small scales in the resolved flow field (Wagner et al, 2006).

#### 4.3.4 SGS models

Since the SGS stress tensor obtained by filtering process is unknown, it requires modeling. Most of the developed models were established upon Boussinesq's hypothesis, which defines a relation between SGS stress tensor and subgrid turbulent viscosity as follows,

$$\tau_{ij} - \frac{\delta_{ij} \tau_{kk}}{3} = -2\mu_t \widetilde{S}_{ij} \quad (4.18)$$

$$\widetilde{S}_{ij} = \frac{1}{2} \left( \frac{\partial \widetilde{u}_i}{\partial x_j} + \frac{\partial \widetilde{u}_j}{\partial x_i} \right) \quad (4.19)$$

where  $\widetilde{S}_{ij}$  is the resolved scale strain rate tensor,  $\mu_t$  is the subgrid turbulent viscosity,  $\tau_{kk}$  is the isotropic part of SGS and  $\delta_{ij}$  denotes the Kronecker delta (Mason, Galperin and Orszag, 1994).

The first basic SGS model was conjectured by Smagorinsky, in which a mixing length of  $L_s$  proportional to filter width  $\Delta$  is considered.

$$L_s = C_s \Delta \quad (4.20)$$

In equation 4.20,  $C_s$  denotes the Smogarinsky constant, which is not a universal constant and depends on the flow type, notably (Bernard and Wallace, 2002), so that it is required to adjust the constant for different applications.

Using the equation 4.20, the eddy viscosity,  $\mu_t$ , can be defined in terms of the mixing length.

$$\mu_t = L_s^2 |\tilde{S}| \quad (4.21)$$

$$|\tilde{S}| = \sqrt{2\tilde{S}_{ij}\tilde{S}_{ij}} \quad (4.22)$$

Germano et al (1991) had suggested an advanced SGS model to dynamically determine the Smogorinsky constant, which varies in time and space during the simulation, with a method of double filtering. Since the value of  $C_s$  does not remain constant in the whole domain in the dynamic model, the energy transfer from small to large scales can be captured as well.

In this study, LES with the dynamic Smogorinsky SGS model was used for the simulation of the flow field of an incompressible, axisymmetric, turbulent swirling jet.

#### 4.4 Mean Flow and Turbulent Parameters

As mentioned before, the swirling jet from the experimental study case of Örlü and Alfredsson (2008) is used as the validation of the LES simulations in this thesis.

As a reminder, the experimental flow field variables (Örlü and Alfredsson, 2008) that are used in this study are given in Table 4.1.

The experimental case flow field variables are given in Table 4.1.

**Table 4.1** : Experimental jet flow parameters.

Parameter	Symbol	Value	Unit
Bulk velocity at inflow boundary	$U_{bulk}$	6.00	m/s
Swirl Number	$S$	0.5	-
Density of air	$\rho$	1.177	kg/m <sup>3</sup>
Dynamic viscosity of air	$\mu$	1.846	10 <sup>-5</sup> kg/m s
Pipe nozzle diameter	$D_0$	0.06	m
Operating pressure	$P_0$	101,325	Pa

According to Kolmogorov's hypothesis, the relations between macro and micro scales in turbulent flows can be defined on the basis of Reynolds number of large scales,  $Re_l$ , as follows,

$$\eta/l_0 \cong Re_l^{-3/4} \quad (4.24)$$

where

$$Re_l = l_0 u_0 \rho / \mu \quad (4.25)$$

$$u_\eta / u_0 \cong Re_l^{-1/4} \quad (4.26)$$

$$\tau_\eta/\tau_0 \cong \text{Re}_l^{-1/2} \quad (4.27)$$

where  $l_0$ ,  $u_0$  and  $\tau_0$  are the length, velocity and time scales of large eddies, while  $\eta$ ,  $u_\eta$  and  $\tau_\eta$  denote the same parameters for small eddies, known as Kolmogorov scales, respectively (Pope, 2000).

To be able to find the magnitudes of the parameters of large scales, two additional relations are required. The first relation implies that the strain rates of large and mean flow scales are proportional and can be given as follows,

$$\frac{U_{\text{mean}}}{L} \sim \frac{u_0}{l_0} \quad (4.28)$$

where  $U_{\text{mean}}$  and  $L$  denote the length and velocity scales of the mean flow, which are already taken as  $U_b$  and  $D_0$  in this study, respectively. The second relation implies that the Reynolds number of the mean flow is one order of magnitude greater than the Reynolds number of macro scales, which can be given as follows,

$$\text{Re} = 10 \cdot \text{Re}_l \quad (4.29)$$

Additionally, it is known that

$$\tau_0 = l_0/u_0 \quad (4.30)$$

By using the equations 4.23, 4.24, 4.25, 4.26, 4.27, 4.28 and 4.29, the magnitudes of the parameters of large and small scales are calculated and given in Table 4.2.

**Table 4.2 :** Turbulent scales.

Parameter	Large Scales	Kolmogorov scales
Length [m]	0.0189	$5.53341 \cdot 10^{-05}$
Velocity [m/s]	1.897	0.271
Time [s]	0,01	0.000204



## 5. COMPUTATIONAL PROCEDURES OF SWIRLING JETS

### 5.1 Computational Domain

The computational domain of the jet in this study was designed according to the experimental setup of Örlü and Alfredsson (2008). The geometry of the domain was a truncated cone as shown in Figure 5.1. A pipe of diameter  $D_0 = 0.06$  m and wall thickness of 5 mm was aligned concentrically within the cone and extended from the bottom of the cone to the jet exit plane, where the origin of the coordinate system was set. The computational domain started from the bottom plane of the cone, which was located at a distance of  $D_0$  upstream of the jet exit. The length of the domain in the axial direction was extended up to a distance of  $40D_0$ , measured from the origin to the top plane of the cone. The diameter of cone at the bottom and top were  $10D_0$  and  $40D_0$ , respectively.

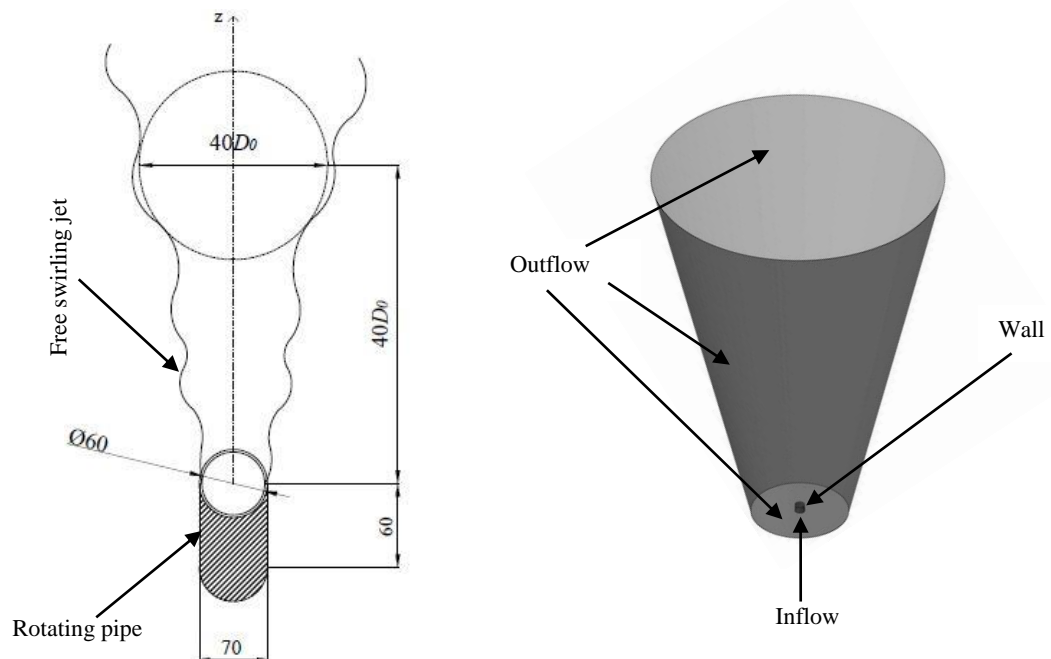


**Figure 5.1 :** Schematic and geometry of computational jet domain with boundaries shown.

The structured hexahedral mesh was built by employing a commercial software (ANSYS ICEM CFD 18.2). The mesh consists of 5,533,041 hexa elements defined in 48 blocks, which satisfies the criterion  $\Delta/\eta = 8.966 < 12$  (Pope, 2000) where  $\Delta$  is the smallest cell size of the mesh and  $\eta$  is the Kolmogorov length scale given in Table 4.2. Multiple interpolated o-grid blocks were created to improve the mesh quality. The outer o-grid blocks were designed by assuming that the total angle of spread of the free jet is  $24^\circ$  (Cushman-Roisin, 2014). The mesh, with a minimum cell size of  $\Delta z_{\min} = 0.0005$  m in the near field of jet, was generated according to turbulent length scales given in Table 4.2, which allows an entrainment surface to be able to represent the small eddies. This was expected to increase the accuracy of the simulation.

Different sections of the computational grid are shown in Figures 5.2.

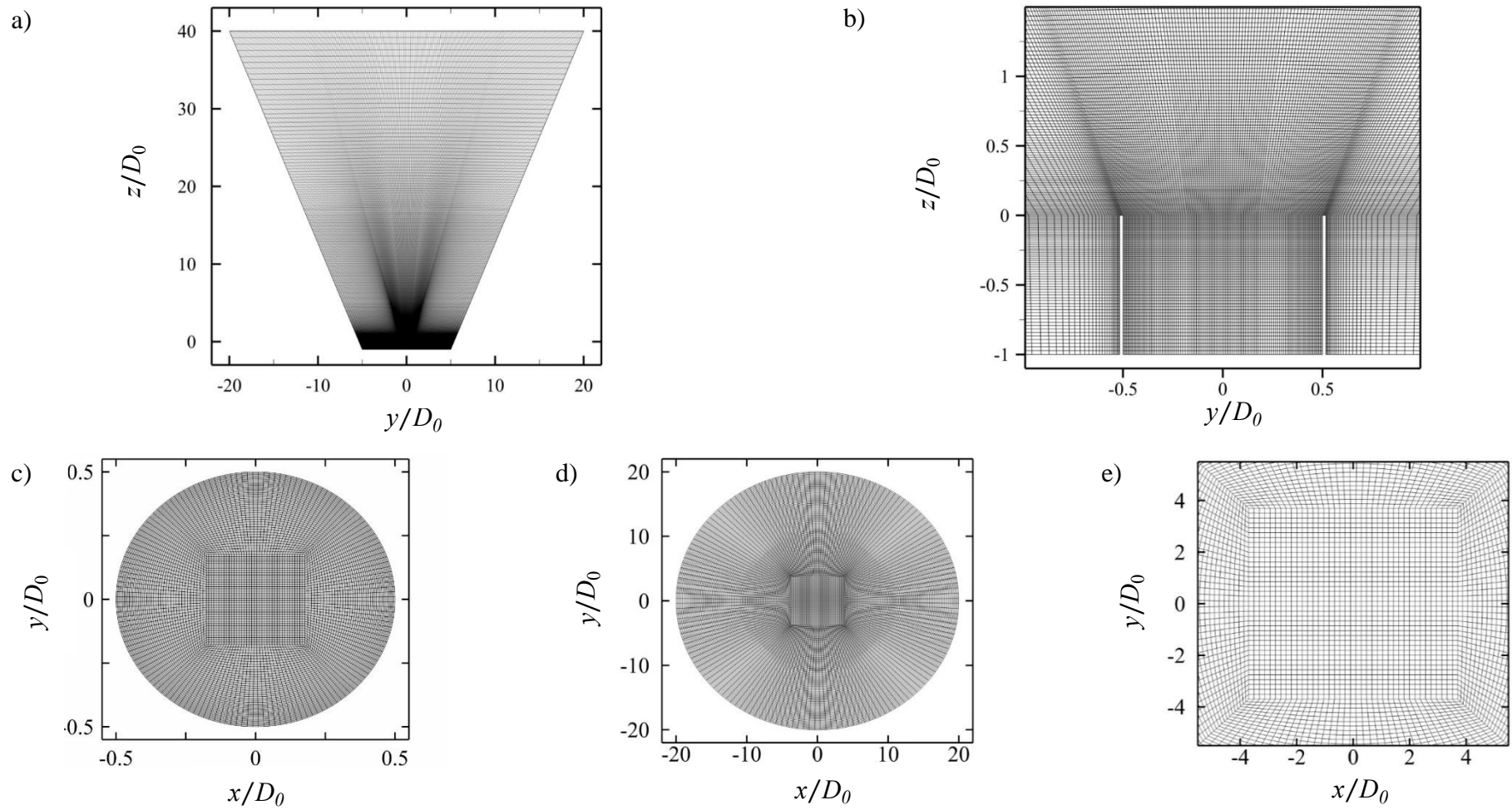


**Figure 5.2 :** Computational mesh a) slice of computational grid at  $x = 0$ . b) Close up section of computational grid near jet exit at  $x = 0$  c) Computational grid section in the  $y-z$  plane, close up of inlet plane grid. d) O-grid type used in azimuthal direction e) strong zoom of d).

## **5.2 Flow Solver and Numerical Methods**

As a computational platform to solve the governing equations, a three-dimensional, incompressible, transient solver with double precision (ANSYS FLUENT V18.0) was used with the finite-volume discretization method. Since the finite-volume discretization of the code uses an implicit filtering through the integration over volumes of computational cells (which is similar to convolution with a top hat filter) an explicit filtering of instantaneous flow field equations was not necessary (Zhiyin, 2014).

### **5.2.1 Spatial discretization**

In the solver, pressure and velocity values were stored in cell centers. However, the values of the pressure at the faces between cells were required to solve the discretized momentum equations. Usually, the momentum equation coefficients are used to obtain the pressure values at faces. This scheme is feasible for flow simulations, in which the pressure profile does not have a high gradient at cell faces (Chung, 2010; ANSYS, Inc., 2012). For the convection discretization of transport equations, bounded central differencing scheme was utilized which is considered as the optimal setting for LES due to its low numerical diffusion (Guseva et al., 2018; Adedoyin, Walters, & Bhushan, 2015). The bounded scheme is an improved version of central differencing, in which the central differencing, the first-order and second-order upwind schemes are all blended. This approach eliminates the unnatural numerical oscillations caused by the standard second order central differencing scheme and thus, it yields a more accurate solution and increases the numerical stability (Leonard, 1991). The Pressure-Implicit with Splitting of Operators (PISO) was employed as the pressure-velocity coupling method, which is specially recommended for transient flows and can maintain high stability even with large time steps (Chung, 2010; Versteeg & Malalasekera, 2007).

### **5.2.2 Temporal discretization**

For temporal discretization, bounded second order implicit formulation was selected as it provides high stability due to bounded variables. It is unconditionally stable for any time step size, unlike explicit methods, in which the time step size is dependent

on mesh size according to the Courant-Friedrich-Lewy (CFL) condition (Courant et al, 1928). The CFL number is a function of the local velocity  $U_L$  and cell size  $\Delta z$ , and can be given for one-dimensional case as

$$CFL = U_L \frac{\Delta t}{\Delta z} \quad (4.31)$$

where  $\Delta t$  denotes the time step size. Even though implicit temporal discretization method is not limited by CFL number as far as numerical stability is concerned, it should be remarked that sufficiently small temporal and spatial resolution are still required for high accuracy in LES simulations. In this study, the time step size was chosen as  $\Delta t = 0.001$  s, about 5 times greater than the Kolmogorov time scale given in Table 4.2. It captures the smallest scales of the inertial sub-range so that a maximum CFL number below 11 was maintained for the implicit temporal discretization.

### 5.2.3 Wall boundary condition

For the pipe walls shown in Figure 5.2b, the no-slip boundary condition was assigned, in which the magnitudes of all velocity components at the wall are set to zero.

### 5.2.4 Inflow boundary conditions

The inlet boundary was located at the pipe inlet, where a prescribed velocity was employed by specifying the time-varying velocity components in the axial and azimuthal directions. Two simulations with different turbulent properties were computed: The first simulation was run without any turbulent velocity fluctuations at the inlet boundary. In the second simulation, the Fourier modes obtained by the linear stability analysis were superimposed over all frequency and wavenumber spaces for the radial, azimuthal and axial velocity components as follows,

$$\sum_w \sum_{k_r} \sum_{k_\phi} \sum_{k_z} A_i(r) e^{i\{k_r r + k_\phi \phi + k_z z - wt\}} \quad (4.32)$$

However, the orthonormality condition imposed in equation 2.40 leads to the rms fluctuations (eigenfunctions in summation 4.31) to an arbitrary constant, which was

previously set to 1. In order to have the desired turbulent intensity (TI) at the inflow boundary, the unscaled rms fluctuations needed to be scaled by a factor  $c$  defined as,

$$C = \frac{TI \cdot U_{bulk}}{u_{z,rms}} \quad (4.33)$$

where  $U_{bulk} = 6.0$  m/s. The TI was chosen according to the experimental data (Örlü and Alfredsson, 2008) as 14.84%. Hence, one can make the unscaled rms fluctuations producing the same TI as the experimental value, if  $c$  is set to 0.011, which is based on the maximum value  $u_{z,rms}|_{max} = 86.28$  (see Figure 3.7b). The resulting scaled fluctuating velocity components were then superimposed on the mean velocity profiles to generate the time-dependent axial, radial and azimuthal velocity components.

The turbulent intensity characteristics at inflow boundary and the corresponding values of " $c$ " are given in Table 5.1 for all simulations.

**Table 5.1 :** Turbulent intensity characteristics at inflow boundary and the calculated values of  $c$  for all simulations.

Simulation	TI	$C$
SIM1	No fluctuation	-
SIM2	14.84%	0.010319

By using a UDF, the resulting scaled signal for the radial velocity component was directly applied at inflow boundary, while the signals for the axial and azimuthal velocity components were first superimposed over the mean profiles to generate the time-dependent turbulent axial and tangential velocity profiles respectively.

### 5.2.5 Outflow boundary conditions

At three outflow boundaries shown in Figure 5.1, the pressure outlet conditions were employed, which assigned a constant static pressure (zero gauge pressure) at the boundary, while all other quantities were extrapolated from the interior. In order to avoid the reflection of the outgoing waves from the outlet surfaces back into the interior of the domain, these boundaries also need to be non-reflecting. The formulation of the non-reflecting boundary condition, where the waves are numerically absorbed and do not corrupt the solution, is given as,

$$\frac{\partial \theta}{\partial t} + U_c \frac{\partial \theta}{\partial n} = 0 \quad (4.34)$$

where  $\theta$  represents any dependent variable of the flow field,  $n$  denotes the coordinate in the direction normal to the outflow plane and  $U_c$  is convection velocity, which is required to maintain the overall mass flux conservation (Ferziger and Peric, 2002).

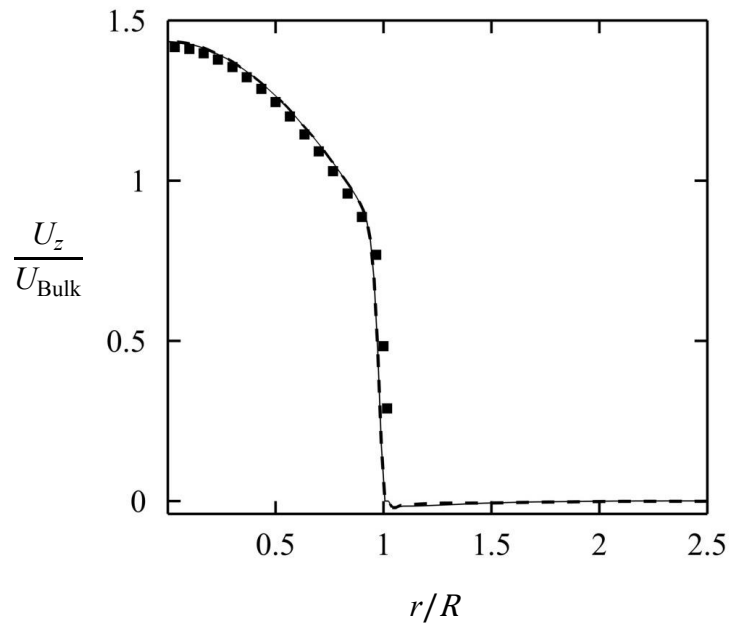


## 6. RESULTS OF LARGE EDDY SIMULATIONS OF SWIRLING JETS

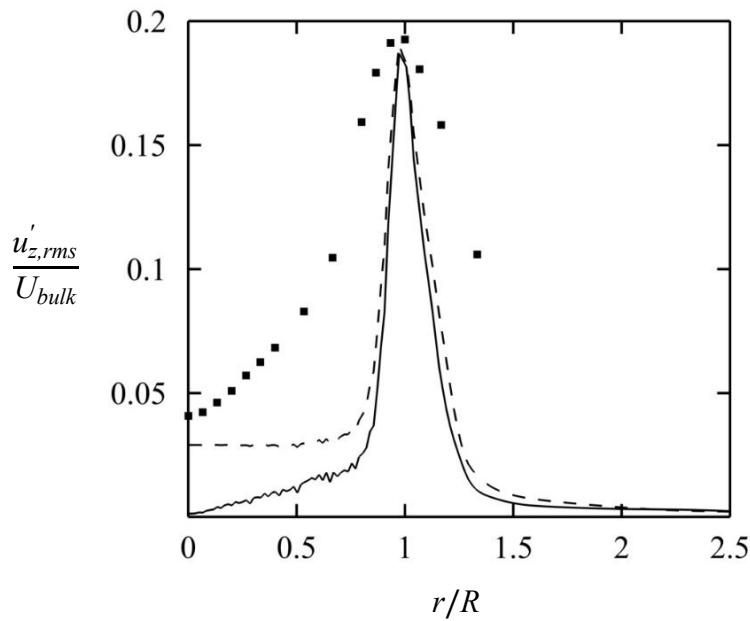
In this chapter, the time-averaged results of the large eddy simulations are given and compared to the experimental results of Örlü and Alfredsson (2008). The mesh described in 5.1 was used for SIM1 and SIM2. At the beginning of the simulations, the mean axial and azimuthal velocity profile applied at the inflow boundary was slightly modified according to the boundary layer development along the pipe, so that the exact experimental jet exit profiles at  $z/D_0 = 0.0$  were obtained. Both simulations were run initially for 4000 time steps until the flow reached a statistically temporally stationary state. After this time, the numerical data were sampled for over 5000 time steps for proper and robust time statistics.

### 6.1 Axial Velocity Results

Figure 6.1 shows that the computed mean profiles for both cases present an excellent agreement with the experimental profile. As Örlü and Alfredsson stated, this axial mean velocity profile emanating from the rotating pipe flow is matching well with power-law profile of  $U/U_{bulk} = (1 - r/R)^{1/7}$  where  $R = 0.5 \cdot D_0$  (Schlichting, 1979; Örlü and Alfredsson, 2008).



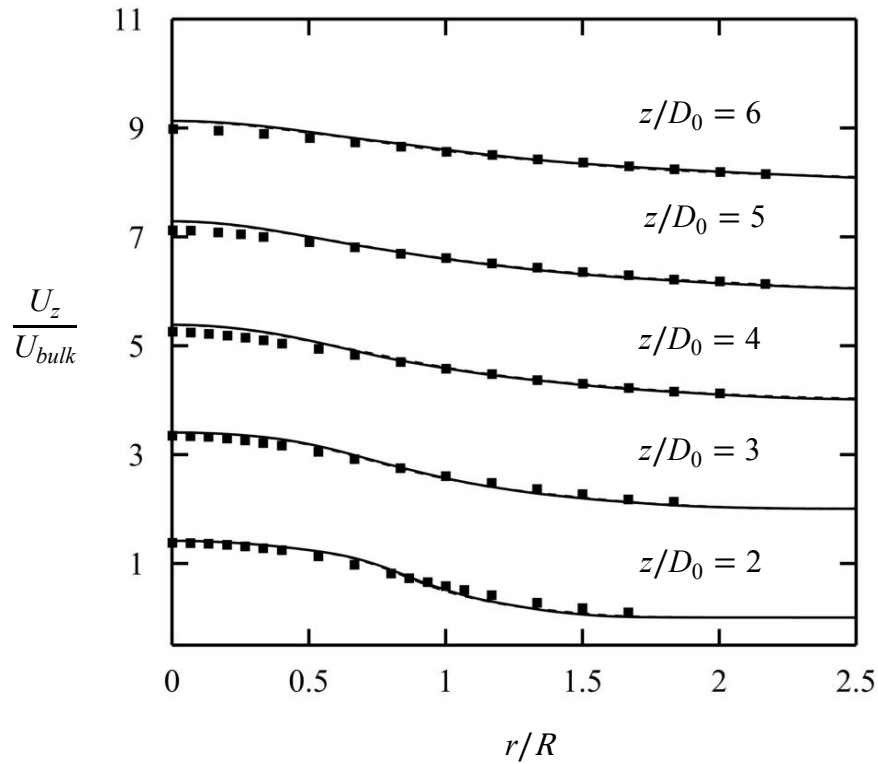
**Figure 6.1 :** Radial profiles of normalized mean axial velocity at  $z/D_0 = 0.0$   
 (■): Experimental data, (—): SIM1, (---): SIM2, (-·-): Power-law profile.



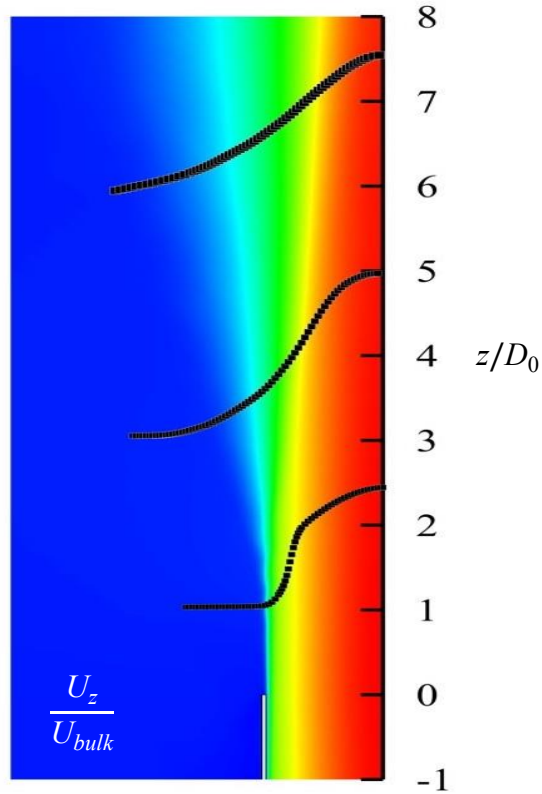
**Figure 6.2 :** Radial profiles of axial turbulent intensity at  $z/D_0 = 0.0$   
 (■): Experimental data, (—): SIM1, (---): SIM2.

The radial distribution of axial component of the turbulent intensity at  $z/D_0 = 0.0$  is shown in Figure 6.2. Compared to the experimental data, the computations of turbulent fluctuations in both simulations capture the location and the magnitude of the peak

value but, otherwise, retain much lower values; although the SIM2 shows some improvements it is still far from being satisfactory. The discrepancies between the simulations and the experimental data can be caused by two reasons; first, the lack of accuracy of measurements near the pipe exit, where the LDV probe volume would be very elongated in the  $r$ -direction, causing severe smearing of the velocity gradient (Jones, 2005). The second, the turbulent diffusional effects might be underestimated in the computations, which manifest itself as relatively longer length of the potential core and more gradual growth of the shear layer (Bogey et al., 2012).



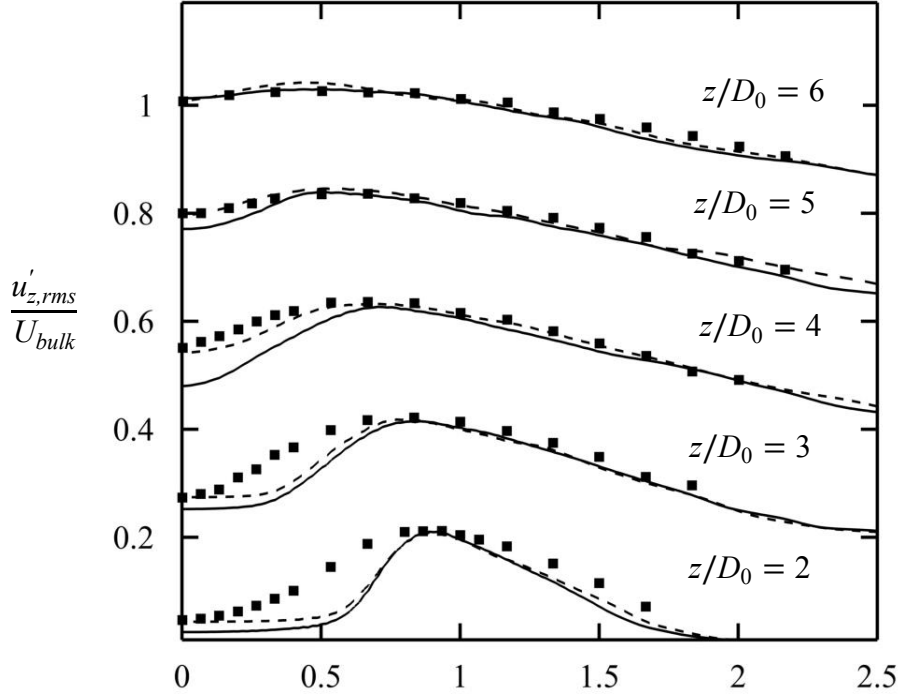
**Figure 6.3 :** Radial profiles for normalized mean axial velocity at different streamwise locations. (■): Experimental data, (—): SIM1, (---): SIM2, (Each curve is moved up by 2 with respect to previous one).



**Figure 6.4 :** Visualization of the time-averaged axial velocity  $U_z$ . The radial profiles of normalized mean axial velocity shown at selected axial positions.

Figure 6.3 compares the normalized mean axial velocity profiles with the measurements at the five different axial stations. In the near-field region, a good agreement with the experiment is observed. Both simulations show an excellent agreement for  $z/D_0 < 4$ . Farther away from the jet exit, very small discrepancies become apparent particularly in the inner shear layer, where the axial velocities near the centerline is slightly overpredicted. In the outer shear layer, nearly a perfect match is observed between the experimentally measured and computationally predicted results.

The radial profiles of the mean axial velocity were replotted ( $z/D_0 = 1, 3$  and  $6$ ) on the contours of the mean axial in Figure 6.4, which puts in evidence that the potential core of the jet was overextended beyond  $z/D_0 = 5$  as described by Vouros and Anidis (2010) and Facciolo et al. (2005).



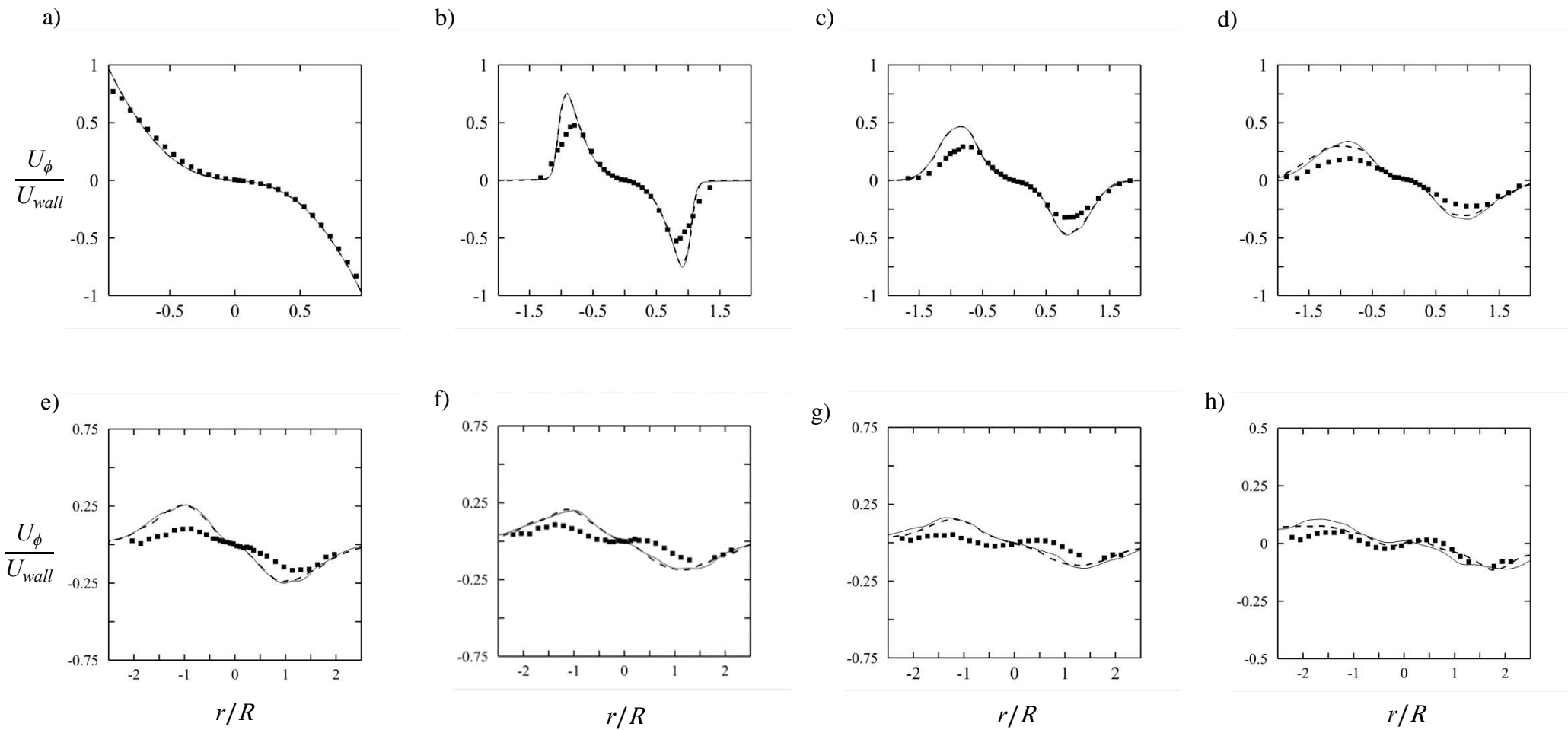
**Figure 6.5 :** Radial profiles of axial turbulent intensity at different streamwise locations: Near-field region. (■): Experimental data, (-): SIM1, (---): SIM2, (Each curve is moved up by 0.2 with respect to previous one).

Figure 6.5 presents the radial profiles of the axial component of the turbulent fluctuations at five axial locations. In near-field of the jet, where there exist a very steep radial gradient at the jet boundary, the axial component of the rms fluctuation,  $u'_{z,rms}/U_{bulk}$ , peaks in the shear region. The rms fluctuations close to the centerline (in the potential core) remain low compared to the shear region, which are referred to the dominance of small-scale fluctuations (Örlü and Alfredson, 2008). This might be the reason for the large departures from the experimental data in the potential core particularly immediately next to the jet exit. It should also be pointed out that the length of the pipe in the computational setup (from which the jet issued) was  $D_0$ , and this was too short to make the flow in the pipe fully developed compared to  $100D_0$  long pipe in the experimental setup. Apparently, this became particularly more severe for the flow turbulence (manifested by the second order moments) to reach the full-developed state. Nonetheless, the results of the SIM2 calculations rapidly recover up to  $z/D_0 = 4$  and attain a very good fit with the experimental data. The agreement is already

satisfactory in the outer shear layer, where the large-scale structures form and grow with the entrainment (Schefer, 1994).

## 6.2 Azimuthal Velocity Results

The radial distribution of the mean azimuthal velocity  $U_\phi$ , which is normalized with the azimuthal velocity at the pipe wall,  $U_{wall} = 3.0$  m/s at 8 different measurement station along the axial direction are plotted in figure 6.6. The present results show excellent agreement at the pipe exit, which validate the inflow boundary condition used in the prediction of the flow in simulations. As presented in the figure 6.6 the mean azimuthal velocity follows the parabola like profile  $(r/R)^2$  and, except for the peaks, this profile match with the measurement and simulations until three diameter downstream (Foiccolo, 2007; Örlü and Alfredson, 2008). As apparent from the Fig.6.6 and 6.7, the decay of the azimuthal velocity peaks in the simulations were slower compared to the experimental data. It implies that the swirling jets calculated is not expanding as fast as in the experiments. This proves the lack of turbulent diffusion in the LES model. It is observed that in contrast to the simulations, the peak values of the mean azimuthal velocity in the experimental data decreased to almost half of the value after just one diameter downstream. This is also attributed to the entrainment of air surrounding the jet, which I not well captured in the simulations. Consequently, the simulations overpredicted the tangential velocity. Nonetheless, both simulations were able to follow the trend of the experimental data until  $z/D_0 = 6$ , where a very interesting phenomenon is observed. In the experimental data, the azimuthal mean velocity profile exhibits a counter rotating core (Fig. 6.6c). This implies that the part of the jet around the centerline starts to rotate in the direction opposite to the one in the rotating pipe upstream (Foiccolo, 2007; Örlü and Alfredson, 2008). This phenomenon is, however, observed slightly downstream at around  $z/D_0 = 8$  in the simulations with the SIM2 having slightly better prediction. It is mostly due to fact that, the eddy-viscosity model in the LES formulation becomes inadequate in the region, where the entrainment turn into a periodic phenomenon and the jet expansion is mostly governed by the diffusivity (García-Villalba, 2006). It is also important to note that the azimuthal mean velocity at this location is relatively small, roughly about 2% of the  $U_\phi$  in the pipe.



**Figure 6.6** : Radial profiles of mean azimuthal velocity at first four streamwise location. (■): Experimental data, (—): SIM1, (---): SIM2

In figure 6.7 radial profile of azimuthal turbulent intensities of two simulations for 8 different axial locations are presented. Unfortunately, there is no experimental data available to compare the results concerning the azimuthal rms values of the fully developed rotating pipe flow. It is observed that for all axial stations, the normalized azimuthal fluctuations were substantially lower at the mixing region around the centreline (Be'er and Chigier 1972) compared to the peak in the jet shear layer at around  $r/R = 1$ . The difference between the centerline values and the values at the peak is reduced because the shear layer gradually penetrate into the jet core until  $z/D_0 = 8$ , where the jet becomes fully developed. It should also be noted that the SIM2 exhibits a wider distribution near the jet exit, and the difference between the SIM1 and SIM2 is reduced away from the jet exit.

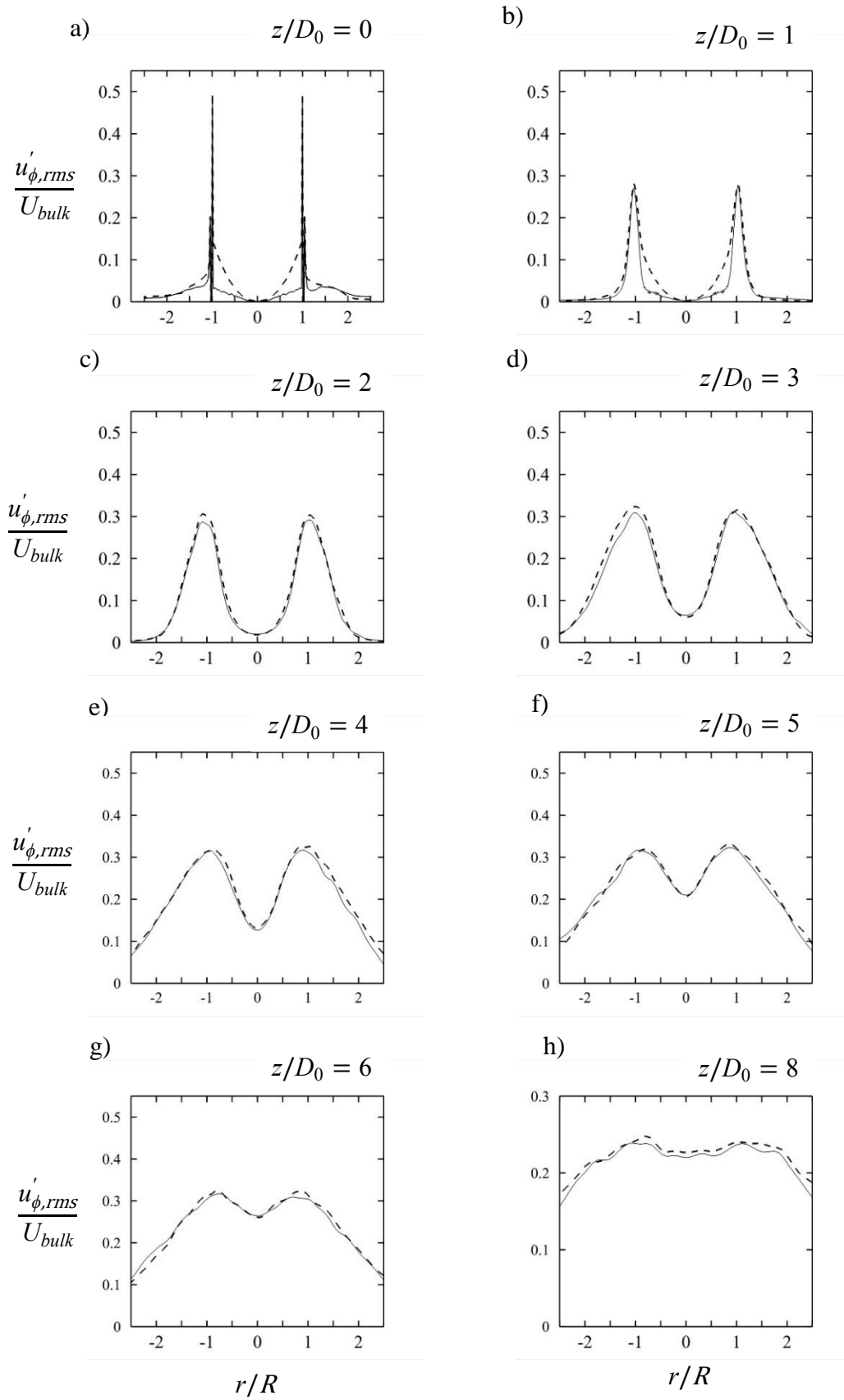


**Figure 6.7 :** Radial profile of azimuthal turbulent intensities at different streamwise locations. (—): SIM1, (---): SIM2.

### 6.3 Spectrum Analysis

In order to analyze the complex features of the swirling jet near the jet exit region, the power spectrum of the computed velocity fluctuations were presented at point  $z/D_0 = 1$  and  $r/R = 0.6$ , which is located in the inner shear layer near the jet exit where there exists coherent structures (García-Villalba, 2008). The case of SIM1, Fig. 6.9(a-c), where no perturbations superimposed on the mean flow shows a fairly low level of fluctuations but a distinct peak around  $f = 2$  Hz for axial velocity component and  $f = 3$  and 4 Hz for the azimuthal and radial disturbance, respectively. The higher harmonics are related to random turbulence eddies present in the flow field.

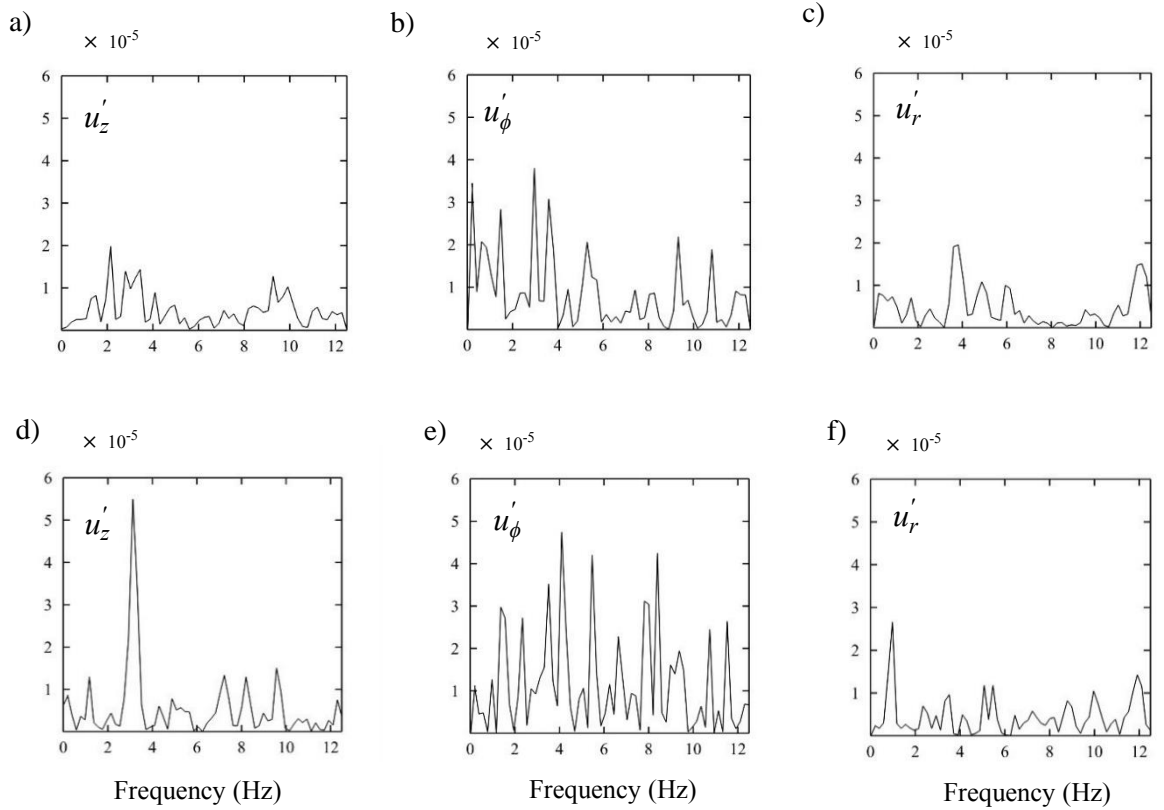


**Figure 6.8 :** Power spectrum of axial velocity at  $z/D_0 = 1$ ,  $r/R = 0.6$ . a) - c) SIM1. d) - f) SIM2.

For the SIM2 case, Fig. 6.9(d-f), where the perturbations are introduced, a dominant frequency of  $f = 3$  Hz can clearly be identified in the axial velocity, which is larger than that for the SIM1. These peaks at the low frequency range is attributed mainly to the well-known swirling flow structure, called the precessing vortex core (PVC) (Syred et al., 1994; Wessman, 1995). The PVC motions are characterized by large structures, which rotate around the axis of symmetry at a very low frequency (Wang

et al., 2004). In the literature, the formation of PVC motion is related to shear layer instability of Kelvin-Helmholtz type (Schlüter, 2000; Oberleithner et al., 2011). It is also evident from the azimuthal and radial rms fluctuations that higher amplitudes are observed in the SIM2 compared to the SIM1, which is a result of the addition of turbulent perturbations. The radial fluctuations have the lowest values of amplitudes between other velocity components as it is expected from the results of the previous section where the radial velocity has the lowest value among other velocity components (Wang et al., 2004).



## 7. CONCLUSION

In this study, hydrodynamic stability approach was used to generate proper and accurate inflow boundary conditions for large eddy simulation of an axisymmetric turbulent swirling jet. For this purpose, the hydrodynamic stability analysis was performed for a circular pipe flow. By solving the linearized equations of motion for fluctuation components with the parallel shooting method, Fourier modes for axial, azimuthal and radial velocity components and pressure were obtained. By superimposing the sets of these modes over frequency and wavenumber spaces, time- and space-dependent velocity signals were produced to use as inflow boundary condition in LES of a turbulent jet. The Reynolds and swirl number of the flow are kept fixed at 24000 and 0.5, respectively. The jet geometry and the axial mean velocity profile were taken from experimental study of Örlü and Alfredsson (2008). Two simulations were run with different turbulence characteristics at inflow boundary and results were compared to the measurements of Örlü and Alfredsson (2008).

The stability analyses are performed for axisymmetric and non-axisymmetric disturbances in cylindrical coordinates. The numerical results showed that the fully developed pipe flow responses was stable to both axisymmetric and helical perturbations, which is consistent with previous stability analyses in both temporal and spatial frameworks. The effect of mode shapes for different frequencies as well as different radial wavenumbers, is illustrated. It appears that the amplitude of the mode shapes increases substantially with frequency. The amplitude modulations' peak value resides between the centerline and the wall, where the outer shear layer is located. Radial RMS distributions of the velocity components show that the axial fluctuations are dominant. Whereas, the azimuthal fluctuation is approximately two orders of magnitudes less than  $u'_{z,rms}$  and the  $u'_{r,rms}$  does not have any significant contribution to the fluctuation energy of the flow.

All simulations provided very similar results at all axial locations regarding the radial distribution of mean axial velocity, and this revealed that the radial velocity signal applied at the inflow boundary did not have a remarkable effect on the jet spread. This

suggested that either the radial velocity fluctuations were suppressed in the very start of the potential core, or their magnitudes were not high enough to make a contribution. Additionally, the potential core length and centerline decay rate were well captured in all two simulations. However, considering the results in terms of axial turbulent intensity, it was observed that the simulations with 14.84% turbulent intensity at the inflow boundary provided better results overall compared to the other case. Same results also revealed that.

Further investigation is done by analyzing the power spectral density of velocity fluctuations. The spectra obtained from LES data revealed the existence of the coherent structures (PVC) in the near flow field of the swirling jet, particularly for the SIM2. Thereby, it can be concluded that flow with perturbed inflow captured the large scale structures in the simulations much better than the non-perturbed one. This study can be extended for non-linear hydrodynamic analysis, which can be performed to calculate more realistic modes without neglecting terms like Reynolds stresses.

This study can further be extended for non-linear hydrodynamic analysis, which can be performed for the calculation of more realistic modes without neglecting terms like Reynolds stresses.

## REFERENCES

- Abid, M., Brachet, M. E., & Huerre, P.** (1993). Linear hydrodynamic instability of circular jets with thin shear layers. *European journal of mechanics. B, Fluids*, 12(5), 683–693.
- Adedoyin, A. A., Walters, D. K., & Bhushan, S.** (2015). Investigation of turbulence model and numerical scheme combinations for practical finite-volume large eddy simulations. *Engineering Applications of Computational Fluid Mechanics*, 9(1), 324–342.  
<https://doi.org/10.1080/19942060.2015.1028151>
- ANSYS Inc.** (2013). Ansys Fluent Theory Guide. *ANSYS Inc., USA*.
- Argyropoulos, C. D., & Markatos, N. C.** (2015). Recent advances on the numerical modelling of turbulent flows. *Applied Mathematical Modelling*, 39(2), 693–732.  
<https://doi.org/10.1016/j.apm.2014.07.001>
- Balestra, G., Gloor, M., & Kleiser, L.** (2015). Absolute and convective instabilities of heated coaxial jet flow. *Physics of Fluids*, 27(5), 1–18.  
<https://doi.org/10.1063/1.4919594>
- Baolin, X.** (2016). *Improved vortex method for LES inflow generation and applications to channel and flat-plate flows* (Doctoral dissertation). Retrieved from <https://www.theses.fr/2016LYSEC058>
- Batchelor, G. K., & Gill, A. E.** (1962). Analysis of the stability of axisymmetric jets. *Journal of Fluid Mechanics*, 14(4), 529–551.  
<https://doi.org/10.1017/S0022112062001421>
- Beér, J. M., & Chiger, N. A.** (1972). *Combustion Aerodynamics*. Applied Science Publishers Ltd. <https://doi.org/10.1017/S0022112072210990>
- Bernard, P., Wallace, J., & Yavuzkurt, S.** (2003). Turbulent Flow: Analysis, Measurement, and Prediction. *Applied Mechanics Reviews*.  
<https://doi.org/10.1115/1.1623759>
- Bogey, C., Marsden, O., & Bailly, C.** (2011). Large-eddy simulation of the flow and acoustic fields of a Reynolds number 105 subsonic jet with tripped exit boundary layers. *Physics of Fluids*, 23(3), 26–28.  
<https://doi.org/10.1063/1.3555634>
- Boiko, A. ., Grek, G. R., Dovgal, A. V, & Kozlov, V. V.** (2002). *The Origin of Turbulence in Near-Wall Flows*. Springer.

- Chung, T. J.** (2010). Computational Fluid Dynamics. In *Computational Fluid Dynamics, Second Edition*. Cambridge University Press.  
<https://doi.org/10.1017/CBO9780511780066>
- Courant, R., Friedrichs, K., & Lewy, H.** (1928). Über die partiellen Differenzgleichungen der mathematischen Physik. *Mathematische Annalen*, 100(1), 32–74. <https://doi.org/10.1007/BF01448839>
- Crow, S. C., & Champagne, F. H.** (1971). Orderly structure in jet turbulence. *Journal of Fluid Mechanics*, 48(3), 547–591.  
<https://doi.org/10.1017/S0022112071001745>
- Cushman-roisin, B.** (2019). *Environmental Fluid Mechanics* (Issue January). John Wiley & Sons, Inc. Retrieved from  
<http://www.dartmouth.edu/~cushman/books/EFM.html>
- Den Toonder, J. M. J., & Nieuwstadt, F. T. M.** (1997). Reynolds number effects in a turbulent pipe flow for low to moderate Re. *Physics of Fluids*, 9(11), 3398–3409. <https://doi.org/10.1063/1.869451>
- Dhamankar, N. S., Blaisdell, G. A., & Lyrintzis, A. S.** (2015). An overview of turbulent inflow boundary conditions for large eddy simulations (Invited). *22nd AIAA Computational Fluid Dynamics Conference, June*.  
<https://doi.org/10.2514/6.2015-3213>
- Dhamankar, N. S., Blaisdell, G. A., & Lyrintzis, A. S.** (2018). Overview of turbulent inflow boundary conditions for large-eddy simulations. *AIAA Journal*, 56(4), 1317–1334. <https://doi.org/10.2514/1.J055528>
- Drazin, P. G., & Reid, W. H.** (2004). *Hydrodynamic Stability* (2nd ed.). Cambridge University Press. <https://doi.org/https://doi.org/10.1017/CBO9780511616938>
- Facciolo, L.** (2006). *A study on axially rotating pipe and swirling jet flows* (Doctoral dissertation). Retrieved from  
<http://kth.diva-portal.org/smash/record.jsf?pid=diva2%3A9755&dswid=3670>
- Facciolo, L., Tillmark, N., Talamelli, A., & Alfredsson, P. H.** (2007). A study of swirling turbulent pipe and jet flows. *Physics of Fluids*, 19(3), 035105.  
<https://doi.org/10.1063/1.2710287>
- Faisst, H.** (2003). *Turbulence transition in pipe flow*, (Doctoral dissertation). Retrieved from <http://archiv.ub.uni-marburg.de/diss/z2003/0156/pdf/diss.pdf>
- Fernandez-Feria, R., & Del Pino, C.** (2002). The onset of absolute instability of rotating Hagen-Poiseuille flow: A spatial stability analysis. *Physics of Fluids*, 14(9), 3087–3097. <https://doi.org/10.1063/1.1497374>

- Ferziger, J. H., & Perić, M.** (2002). Computational Methods for Fluid Dynamics. In *Computational Methods for Fluid Dynamics*. Springer.  
<https://doi.org/10.1007/978-3-642-56026-2>
- Fröhlich, J., & Rodi, W.** (2001). Introduction to Large Eddy Simulation of Turbulent Flows. In *Closure Strategies for Turbulent and Transitional Flows* (pp. 267–298). Cambridge University Press.  
<https://doi.org/10.1017/CBO9780511755385.010>
- Fröhlich, Jochen, & Von Terzi, D.** (2008). Hybrid LES/RANS methods for the simulation of turbulent flows. *Progress in Aerospace Sciences*, 44(5), 349–377.  
<https://doi.org/10.1016/j.paerosci.2008.05.001>
- García-Villalba, M., Fröhlich, J., & Rodi, W.** (2006). Identification and analysis of coherent structures in the near field of a turbulent unconfined annular swirling jet using large eddy simulation. *Physics of Fluids*, 18(5), 1–18.  
<https://doi.org/10.1063/1.2202648>
- García-Villalba, Manuel, & Fröhlich, J.** (2006). LES of a free annular swirling jet - Dependence of coherent structures on a pilot jet and the level of swirl. *International Journal of Heat and Fluid Flow*, 27(5), 911–923.  
<https://doi.org/10.1016/j.ijheatfluidflow.2006.03.015>
- Garg, V. K., & Rouleau, W. T.** (1972). Linear spatial stability of pipe Poiseuille flow. *Journal of Fluid Mechanics*, 54(1), 113–127.  
<https://doi.org/10.1017/S0022112072000564>
- Germano, M., Piomelli, U., Moin, P., & Cabot, W. H.** (1991). A dynamic subgrid-scale eddy viscosity model. *Physics of Fluids A: Fluid Dynamics*, 3(7), 1760–1765. <https://doi.org/10.1063/1.857955>
- Gupta, A. K., Lilley, D. G., & Syred, N.** (1984). *Swirl Flows*. Abacus Press.  
[https://doi.org/10.1016/0010-2180\(86\)90133-1](https://doi.org/10.1016/0010-2180(86)90133-1)
- Heinz, S.** (2020). A review of hybrid RANS-LES methods for turbulent flows: Concepts and applications. *Progress in Aerospace Sciences*, 114, 100597.  
<https://doi.org/10.1016/j.paerosci.2019.100597>
- Howard, L. N., & Gupta, A. S.** (1962). On the hydrodynamic and hydromagnetic stability of swirling flows. *Journal of Fluid Mechanics*, 14(3), 463–476.  
<https://doi.org/10.1017/S0022112062001366>
- Hu, B., Musculus, M. P. B., & Oefelein, J. C.** (2012). The influence of large-scale structures on entrainment in a decelerating transient turbulent jet revealed by large eddy simulation. *Physics of Fluids*, 24(4), 045106.  
<https://doi.org/10.1063/1.3702901>
- Huerre, P.** (1985). Absolute and convective instabilities in free shear layers. *Journal of Fluid Mechanics*, 159, 151–168.  
<https://doi.org/10.1017/S0022112085003147>

- Huerre, P., & Monkewitz, P. A.** (1990). Local and Global Instabilities in Spatially Developing Flows. *Annual Review of Fluid Mechanics*.  
<https://doi.org/10.1146/annurev.fl.22.010190.002353>
- Hussain, A. K. M. F., & Reynolds, W. C.** (1970). The mechanics of an organized wave in turbulent shear flow. *Journal of Fluid Mechanics*.  
<https://doi.org/10.1017/S0022112070000605>
- Imao, S., Itoh, M., & Harada, T.** (1996). Turbulent characteristics of the flow in an axially rotating pipe. *International Journal of Heat and Fluid Flow*.  
[https://doi.org/10.1016/0142-727X\(96\)00057-4](https://doi.org/10.1016/0142-727X(96)00057-4)
- Jiménez, J.** (2003). Computing high-Reynolds-number turbulence: Will simulations ever replace experiments? *Journal of Turbulence*, 4(December 2014), 37–41.  
<https://doi.org/10.1088/1468-5248/4/1/022>
- Kambe, T.** (1969). The stability of an axisymmetric jet with parabolic profile. *Journal of the Physical Society of Japan*. <https://doi.org/10.1143/JPSJ.26.566>
- Keating, A., Piomelli, U., Balaras, E., & Kaltenbach, H.-J.** (2004). A priori and a posteriori tests of inflow conditions for large-eddy simulation. *Physics of Fluids*, 16(12), 4696–4712. <https://doi.org/10.1063/1.1811672>
- Keller., H. B.** (2018). *Numerical methods for two-point boundary-value problems*. Dover Publications, Inc.
- Klein, M., Sadiki, A., & Janicka, J.** (2003). A digital filter based generation of inflow data for spatially developing direct numerical or large eddy simulations. *Journal of Computational Physics*, 186(2), 652–665.  
[https://doi.org/10.1016/S0021-9991\(03\)00090-1](https://doi.org/10.1016/S0021-9991(03)00090-1)
- Knowles, K., & Saddington, A. J.** (2006). A review of jet mixing enhancement for aircraft propulsion applications. In *Proceedings of the Institution of Mechanical Engineers, Part G: Journal of Aerospace Engineering*.  
<https://doi.org/10.1243/09544100G01605>
- Lambourne, N. C., & Bryer, D. W.** (1961). The bursting of leading-edge vortices - some observations and discussion of the phenomenon. In *Aeronautical Research Council Reports & Memoranda* (Vol. 3282).
- Leibovich, S.** (1984). Vortex stability and breakdown - survey and extension. *AIAA Journal*, 22(9), 1192–1206. <https://doi.org/10.2514/3.8761>
- Leonard, B. P.** (1991). The ULTIMATE conservative difference scheme applied to unsteady one-dimensional advection. *Computer Methods in Applied Mechanics and Engineering*, 88(1), 17–74. [https://doi.org/10.1016/0045-7825\(91\)90232-U](https://doi.org/10.1016/0045-7825(91)90232-U)

- Lessen, M., Deshpande, N. V., & Hadji-Ohanes, B.** (1973). Stability of a potential vortex with a non-rotating and rigid-body rotating top-hat jet core. *Journal of Fluid Mechanics*, *60*(3), 459–466. <https://doi.org/10.1017/S0022112073000297>
- Lessen, M., Fox, J. A., & Zien, H. M.** (1965). The instability of inviscid jets and wakes in compressible fluid. *Journal of Fluid Mechanics*, *21*(1), 129–143. <https://doi.org/10.1017/S0022112065000095>
- Lessen, M., Sadler, S. G., & Liu, T. Y.** (1968). Stability of pipe Poiseuille flow. *Physics of Fluids*, *11*(7), 1404–1409. <https://doi.org/10.1063/1.1692122>
- Lessen, M., & Singh, P. J.** (1973). The stability of axisymmetric free shear layers. *Journal of Fluid Mechanics*, *60*(3), 433–457. <https://doi.org/10.1017/S0022112073000285>
- Lessen, M., Singh, P. J., & Paillet, F.** (1974). The stability of a trailing line vortex. Part 1. Inviscid theory. *Journal of Fluid Mechanics*. <https://doi.org/10.1017/S0022112074002175>
- Liang, H., & Maxworthy, T.** (2005). An experimental investigation of swirling jets. *Journal of Fluid Mechanics*, *525*, 115–159. <https://doi.org/10.1017/S0022112004002629>
- Loiseau, J.** (2014). *Dynamics and global stability analysis of three-dimensional flows (Doctoral Thesis)*. Ecole nationale supérieure d'arts et métiers - ENSAM.
- Lund, T. S., Wu, X., & Squires, K. D.** (1998). Generation of Turbulent Inflow Data for Spatially-Developing Boundary Layer Simulations. *Journal of Computational Physics*, *140*(2), 233–258. <https://doi.org/10.1006/jcph.1998.5882>
- Martinelli, F., Olivani, A., & Coghe, A.** (2007). Experimental analysis of the precessing vortex core in a free swirling jet. *Experiments in Fluids*, *42*(6), 827–839. <https://doi.org/10.1007/s00348-006-0230-x>
- Mason, P. J., Galperin, B., & Orszag, S. A.** (1993). *Large-eddy simulation of complex engineering and geophysical flows* (Vol. 120, Issue 520). Cambridge University Press. <https://doi.org/10.1002/qj.49712052017>
- McIlwain, S., & Pollard, A.** (2002). Large eddy simulation of the effects of mild swirl on the near field of a round free jet. *Physics of Fluids*, *14*(2), 653–661. <https://doi.org/10.1063/1.1430734>
- Meseguer, A., & Trefethen, L. N.** (2000). *A spectral Petrov–Galerkin formulation for pipe flow I: Linear stability and transient growth* (Issue 00/18). <http://eprints.maths.ox.ac.uk/1255/1/NA-00-18.pdf>

- Michalke, A.** (1965). On spatially growing disturbances in an inviscid shear layer. *Journal of Fluid Mechanics*, 23(3), 521–544. <https://doi.org/10.1017/S0022112065001520>
- Michalke, A.** (1984). Survey on jet instability theory. *Progress in Aerospace Sciences*, 21(C), 159–199. [https://doi.org/10.1016/0376-0421\(84\)90005-8](https://doi.org/10.1016/0376-0421(84)90005-8)
- Mishra, A.** (2018). Energy transfer mechanisms in nonuniform density viscous swirling flows: A linear stability analysis. *2018 Fluid Dynamics Conference*. <https://doi.org/10.2514/6.2018-3093>
- Mohseni, K., & Colonius, T.** (2000). Numerical Treatment of Polar Coordinate Singularities. *Journal of Computational Physics*, 157(2), 787–795. <https://doi.org/10.1006/jcph.1999.6382>
- Moin, P., & Mahesh, K.** (1998). DIRECT NUMERICAL SIMULATION: A Tool in Turbulence Research. *Annual Review of Fluid Mechanics*, 30(1), 539–578. <https://doi.org/10.1146/annurev.fluid.30.1.539>
- Monkewitz, P. A., & Sohn, K. D.** (1988). Absolute instability in hot jets. *AIAA Journal*, 26(8), 911-916. <https://doi.org/10.2514/3.9990>
- Morse, A. P.** (1980). *Axisymmetric Free Shear Flows With and Without Swirl* (Doctoral dissertation). Imperial College London, Retrieved from. <http://hdl.handle.net/10044/1/7641>
- Müller, J. S., Lückoff, F., Paredes, P., Theofilis, V., & Oberleithner, K.** (2020). Receptivity of the turbulent precessing vortex core: Synchronization experiments and global adjoint linear stability analysis. *Journal of Fluid Mechanics*, 888. <https://doi.org/10.1017/jfm.2019.1063>
- Oberleithner, K., Paschereit, C. O., & Wagnanski, I.** (2014). On the impact of swirl on the growth of coherent structures. *Journal of Fluid Mechanics*, 741, 156–199. <https://doi.org/10.1017/jfm.2013.669>
- Oberleithner, K., Sieber, M., Nayeri, C. N., Paschereit, C. O., Petz, C., Hege, H. C., Noack, B. R., & Wagnanski, I.** (2011). Three-dimensional coherent structures in a swirling jet undergoing vortex breakdown: Stability analysis and empirical mode construction. *Journal of Fluid Mechanics*. <https://doi.org/10.1017/jfm.2011.141>
- Olendraru, C., Sellier, A., Rossi, M., & Huerre, P.** (1999). Inviscid instability of the Batchelor vortex: Absolute-convective transition and spatial branches. *Physics of Fluids*, 11(7), 1805–1820. <https://doi.org/10.1063/1.870045>
- Örlü, R., & Alfredsson, P. H.** (2008). An experimental study of the near-field mixing characteristics of a swirling jet. *Flow, Turbulence and Combustion*, 80(3), 323–350. <https://doi.org/10.1007/s10494-007-9126-y>

- Ortega-Casanova, J.** (2011). Numerical simulation of the heat transfer from a heated plate with surface variations to an impinging jet. *Two Phase Flow, Phase Change and Numerical Modeling, Amimul Ahsan*, 76(1998), 128–143. <https://doi.org/10.5772/19666>
- Otero, E.** (2009). Synthetic Inflow Condition for Large Eddy Simulation (Synthetic Eddy Method) (Doctoral dissertation). Retrieved from <https://pdfs.semanticscholar.org/8a60/f37b5761b2680625f174d3e9b38974d2b56f.pdf>
- Özdemir, I. B., & Whitelaw, J. H.** (1993). Impingement of an Unsteady Two-Phase Jet on Unheated and Heated Flat Plates. *Journal of Fluid Mechanics*. <https://doi.org/10.1017/S0022112093003854>
- Özdemir, I. B., & Whitelaw, J. H.** (1992). Impingement of an axisymmetric jet on unheated and heated flat plates. *Journal of Fluid Mechanics*. <https://doi.org/10.1017/S002211209200017X>
- Panda, J., & McLaughlin, D. K.** (1994). Experiments on the instabilities of a swirling jet. *Physics of Fluids*, 6(1), 263–276. <https://doi.org/10.1063/1.868074>
- Paschereit, C. O., Terhaar, S., Čosić, B., & Oberleithner, K.** (2014). Application of linear hydrodynamic stability analysis to reacting swirling combustor flows. *Journal of Fluid Science and Technology*, 9(3), JFST0024–JFST0024. <https://doi.org/10.1299/jfst.2014jfst0024>
- Pedley, T. J.** (1969). On the instability of viscous flow in a rapidly rotating pipe. *Journal of Fluid Mechanics*, 35(1), 97–115. <https://doi.org/10.1017/S002211206900098X>
- Pope, S. B.** (2000). Turbulent Flows. In *Turbulent Flows*. Cambridge University Press. <https://doi.org/10.1017/CBO9780511840531>
- Press, W. H., Teukolsky, S. A., Vetterling, W. T., & Flannery, B. P.** (1992). Numerical Recipes Example Book (FORTRAN) 2nd Edition. In *Book* (2nd ed.). Cambridge University Press.
- Qadri, U. A.** (2013). *Global stability and control of swirling jets and flames* (Doctoral thesis). University of Cambridge, <https://doi.org/10.17863/CAM.14066>
- Rayleigh, L.** (1878). On the instability of jets. *Proceedings of the London Mathematical Society*. <https://doi.org/10.1112/plms/s1-10.1.4>
- Ribeiro, M. M., & Whitelaw, J. H.** (1980). Coaxial jets with and without swirl. *Journal of Fluid Mechanics*, 96(04), 769. <https://doi.org/10.1017/S0022112080002352>

- Sagaut, P.** (2006). *Large Eddy Simulation for Incompressible Flows: An Introduction* (3<sup>rd</sup> ed., Vol. 12, Issue 10). Springer.  
<https://doi.org/10.1007/b137536>
- Schefer, R. W., Kerstein, A. R., Namazian, M., & Kelly, J.** (1994). Role of large-scale structure in a nonreacting turbulent CH 4 jet. *Physics of Fluids*, 6(2), 652–661. <https://doi.org/10.1063/1.868305>
- Schlichting, H., & Gersten, K.** (2017). Boundary-Layer Theory. In *Boundary-Layer Theory* (9th ed.). Springer Berlin Heidelberg. <https://doi.org/10.1007/978-3-662-52919-5>
- Schlüter, J., Pitsch, H., & Moin, P.** (2002). Consistent boundary conditions for integrated LES/RANS simulations: LES outflow conditions. *32nd AIAA Fluid Dynamics Conference and Exhibit* (p. 3121).
- Semaan, R., & Naughton, J. W.** (2013). Three-component laser-doppler-anemometry measurements in turbulent swirling jets. *AIAA Journal*, 51(9), 2098–2113. <https://doi.org/10.2514/1.J051783>
- Skene, C. S., & Schmid, P. J.** (2019). Adjoint-based parametric sensitivity analysis for swirling M-flames. *Journal of Fluid Mechanics*, 859(January), 516–542. <https://doi.org/10.1017/jfm.2018.793>
- Smagorinsky, J.** (1963). General Circulation Experiments with the Primitive Equations. I. The Basic Experiment. *Monthly Weather Review*, 91(3), 99–164.
- Spalart, P. R.** (1988). Direct simulation of a turbulent boundary layer up to  $R\theta=1410$ . *Journal of Fluid Mechanics*, 187, 61–98. <https://doi.org/10.1017/S0022112088000345>
- Syred, N.** (2006). A review of oscillation mechanisms and the role of the precessing vortex core (PVC) in swirl combustion systems. In *Progress in Energy and Combustion Science*. <https://doi.org/10.1016/j.pecs.2005.10.002>
- Tabor, G. R., & Baba-Ahmadi, M. H.** (2010). Inlet conditions for large eddy simulation: A review. *Computers and Fluids*, 39(4), 553–567. <https://doi.org/10.1016/j.compfluid.2009.10.007>
- Tennekes, H., & Lumley, J. L.** (1972). *A First Course in Turbulence*. MIT Press.
- Vaidya, H. A., Ertunç, Ö., Genç, B., Beyer, F., Köksoy, Ç., & Delgado, A.** (2011). Numerical simulations of swirling pipe flows- decay of swirl and occurrence of vortex structures. *Journal of Physics: Conference Series*. <https://doi.org/10.1088/1742-6596/318/6/062022>
- Vanderborck, G., & Platten, J. K.** (1978). Stability of the Pipe Poiseuille Flow, with Respect to Axi and Nonaxisymmetric Disturbances. *Journal of Non-Equilibrium Thermodynamics*, 3(3), 169–190. <https://doi.org/10.1515/jnet.1978.3.3.169>

- Versteeg, H. K., Malalasekera, W., Orsi, G., Ferziger, J. H., Date, A. W., & Anderson, J. D.** (2007). *An Introduction to Computational Fluid Dynamics - The Finite Volume Method*. In Fluid flow handbook. McGraw-Hill, Pearson education.
- Vouros, A. P., & Panidis, T.** (2013). Turbulent properties of a low Reynolds number, axisymmetric, pipe jet. *Experimental Thermal and Fluid Science*, 44, 42–50. <https://doi.org/10.1016/j.expthermflusci.2012.05.012>
- Wagner, C., Hüttl, T., & Sagaut, P.** (2007). *Large-Eddy Simulation for Acoustics* (Cambridge Aerospace Series). Cambridge: Cambridge University Press.
- Wang, P., Bai, X. S., Wessman, M., & Klingmann, J.** (2004). Large eddy simulation and experimental studies of a confined turbulent swirling flow. *Physics of Fluids*, 16(9), 3306–3324. <https://doi.org/10.1063/1.1769420>
- Wang, S., & Rusak, Z.** (1996). On the stability of an axisymmetric rotating flow in a pipe. *Physics of Fluids*, 8(4), 1007–1016. <https://doi.org/10.1063/1.868882>
- Wang, S., Rusak, Z., Gong, R., & Liu, F.** (2016). On the three-dimensional stability of a solid-body rotation flow in a finite-length rotating pipe. *Journal of Fluid Mechanics*, 797(2016), 284–321. <https://doi.org/10.1017/jfm.2016.223>
- Weigand, B.** (2015). *Analytical Methods for Heat Transfer and Fluid Flow Problems*. In *Analytical Methods for Heat Transfer and Fluid Flow Problems* (2nd ed.). Springer. <https://doi.org/10.1007/978-3-540-68466-4>
- Wu, C., Farokhi, S., & Taghavi, R.** (1992). Spatial instability of a swirling jet — Theory and experiment. *AIAA Journal*, 30(6), 1545–1552. <https://doi.org/10.2514/3.11099>
- Wu, J. Z., Ma, H. Y., & Zhou, M. D.** (2015). Vortical flows. In *Vortical Flows*. <https://doi.org/10.1007/978-3-662-47061-9>
- Wu, X., & Moin, P.** (2008). A direct numerical simulation study on the mean velocity characteristics in turbulent pipe flow. In *Journal of Fluid Mechanics* (Vol. 608). <https://doi.org/10.1017/S0022112008002085>
- Xiao, H., & Cinnella, P.** (2019). Quantification of model uncertainty in RANS simulations: A review. *Progress in Aerospace Sciences*, 108, 1–31. <https://doi.org/10.1016/j.paerosci.2018.10.001>
- Zemtsop, C. P., Stöllinger, M. K., Heinz, S., & Stanescu, D.** (2009). Large-Eddy Simulation of Swirling Turbulent Jet Flows in Absence of Vortex Breakdown. *AIAA Journal*, 47(12), 3011–3021. <https://doi.org/10.2514/1.43813>
- Zhiyin, Y.** (2015). Large-eddy simulation: Past, present and the future. *Chinese Journal of Aeronautics*, 28(1), 11–24. <https://doi.org/10.1016/j.cja.2014.12.007>



## **CURRICULUM VITAE**

**Name Surname** : Amir Mehrabi  
**Place and Date of Birth** : İnan, 1993  
**E-Mail** : amirmehrabi72@gmail.com



### **EDUCATION** :

- **High school** : 2012, İstanbul İnan Lisesi.
- **B.Sc.** : 2016, Istanbul Technical University, Faculty of Mechanical Engineering, Mechanical Engineering Program